Spectroscopic Study of Charge-Transfer States in Organic Semiconductors

Yun Liu

A dissertation
submitted in partial fulfillment of
requirements for the degree of

Doctor of Philosophy

University of Washington

2021

Reading Committee:
David S. Ginger, Chair
Xiaosong Li
Cody W. Schlenker

Program Authorized to Offer Degree:
Chemistry

University of Washington

Abstract

Spectroscopic Study of Charge-Transfer States in Organic Semiconductors

Yun Liu

Chair of the Supervisory Committee:
Professor David S. Ginger
Department of Chemistry

To achieve net zero carbon emission required for a sustainable economy, global energy production requires a clean and reliable solution. Photovoltaic technology that directly converts sunlight into electricity has demonstrated its potential in contributing to a carbon free energy future. Among myriad solar technologies, photovoltaic cells based on organic semiconductors offer unique advantages of being light weight, flexible and low cost and have shown promising photovoltaic performance with efficiency climbing over 18%.

In state-of-the-art organic solar cells, a mixture of polymer electron donor and electron acceptor molecules converts light energy to electrical energy. The rapid performance advancement from 11% to over 18% in recent years is largely achieved by the replacement of fullerene molecules with small molecules as electron acceptors, known as non-fullerene acceptors. These new materials not only unlock promising photovoltaic performance but more importantly pose new photophysical questions that challenge the research community's original understanding of organic solar cells and suggest new design rules. Central to the photophysics of organic solar cells, as reviewed in Chapter 1, is the charge-transfer state formed between the electron donor molecular and the acceptor molecule. The work presented in this thesis focuses on understanding the properties of the charge-transfer state and its role in mediating energy loss in solar cells.

Contrary to the traditional model in which significant driving energy is required to separate tightly bound electron-hole pair in the charge-transfer state, one surprising finding to the organic solar cell community is that the most efficient polymer/non-fullerene organic photovoltaics have negligible driving force for charge separation. Furthermore, compared to fullerene acceptors, non-fullerene acceptors have appreciable absorption, implying that charge generation via hole transfer from acceptor to donor could play an important role. In Chapter 2, via detailed time-resolved and steady state spectroscopic studies, we discover a slow yet efficient generation of the charge-transfer state and charge carriers via hole transfer using a model blend of polymer and non-fullerene acceptors. Our findings also allude to a new photophysical scheme in charge generation that was not observed in polymer/fullerene blends but important to efficient polymer/non-fullerene acceptor blends.

Another remarkable property of many efficient polymer/non-fullerene blends is their high photoluminescence efficiency and consequently small non-radiative recombination loss, suggesting that "a great solar cell is also a great light emitting diode" also applies to organic solar cells and prompting research efforts on improving the luminescence efficiency of charge-transfer states. Based on Shockley-Queisser's theoretical framework, an ideal solar cell should only suffer energy loss from radiative recombination as it is unavoidable, and that any non-radiative recombination is excess. In organic solar cells, however, due to molecular vibrations, non-radiative recombination loss contributes a significant amount to total energy loss. Current research efforts have shown that the non-radiative recombination loss follows an energy-gap law where higher gap materials have intrinsically lower loss. Moreover, photoluminescence yield of the charge-transfer state can be limited by that of the local exciton of the lower bandgap material when these states quantum mechanically mix. In Chapter 3, I combine spectroscopic methods

and molecular dynamic calculations to examine in detail what molecular properties determine photoluminescence yield of the charge-transfer state and non-radiative recombination loss of the solar cell. After demonstrating an intrinsically emissive yet charge-generating small molecule blend, I show that due to wavefunction mixing between the charge-transfer state and the local exciton, both photoluminescence quantum yield *and* lifetime of the local exciton influences emission of the charge-transfer state. The latter is a new consideration for selecting materials for efficient organic photovoltaics and light emitting diodes. In Chapter 4, I propose and show current progress on a previously overlooked spectroscopy method directly detecting wavefunction mixing between the charge-transfer state and the local exciton of non-fullerene acceptor molecules. Our findings and proposal provide direction for molecular design and material selection to limit energy loss in organic solar cells.

TABLE OF CONTENTS

List of Figures

Acknowledgement

This thesis reflects my scientific and personal growth that would not have been possible without many people.

Professors at Carleton College shared their contagious curiosity for knowledge. Thanks to Profs. Chris Calderone, Steve Drew, Dave Alberg, Joe Chihade, Will Hollingsworth, Marion Cass, and Deborah Gross for making me think about chemistry in ways I never did. Special thanks to Chris for showing me how to do research rigorously and thoughtfully.

I am grateful to Prof. Shu-ou Shan at Caltech and Prof. Joan Steitz at Yale for letting me join their groups for summer which fueled my interest in research and for encouraging me to pursue my curiosity outside biochemistry research. It also meant a lot to me to see two trailblazing female scientists in action first-hand.

I want to extend my gratitude to Prof. David Ginger for sharing scientific skills, supporting me during challenging times, and trusting me with responsibilities that have allowed me to grow scientifically and personally. It is easy to get lost in the thick of graduate school and research. David always reminded me of the meaningful questions and shared an optimistic view to get to those answers. I hope to carry this mindset wherever I go.

Thanks to my research collaborators – Slava Coropceanu, Jean-Luc Bredas, Lijian Zuo, Sae Byeok Jo, Chen Zou, and Yunping Huang, whose questions and perspectives have led to exciting research directions and improved the quality of my work. Also, thanks to my thesis committee for support.

Thanks to the staff at shared research facilities and electronics shop for training me on instruments and gladly helping me with issues – Kristine Parra, Liam Bradshaw, William Beaty and Lon buck.

Thanks to many Ginger lab members for your support, especially, to Mark for patiently answering my never-ending stream of questions on OPV and spectroscopy, to Jian for valuable discussions on OPV, to Franzi for sharing spectroscopy knowledge and agreeing to backpacking trips, to Joe for patiently teaching me to make solar cells, to Erin for gladly helping me in lab, to Katie for listening and understanding, and to Jess and Sarthak for countless lively exchanges.

It has been a great pleasure to be part of UW and the Clean Energy Institute, where I met many highly energetic people including fellow graduate students and post-docs, CEI staff, invited speakers, clean technology angel investors, science communication professionals and many others – thank you for all the interesting conversations.

Finally, of course, I want to thank my family and friends for your tremendous love and support as always.

Chapter 1. Introduction

With inevitable demand for renewable and sustainable energy resources as the global economy expands, photovoltaic technology that directly converts solar energy to electricity provides a significant solution. Despite successful commercialization of solar panels, in order to transform global energy production to significantly reduce carbon emission, low-cost and mass deployable photovoltaic technologies are required. Organic semiconductors owning unique advantages of low cost, light weight and easy processability have gained significant research momentum and led to exciting technological breakthroughs in organic solar cells (OSCs). However, compared to silicon and inorganic photovoltaics, OSCs suffer from inferior photovoltaic efficiency. Understanding the fundamental physical and optoelectronic properties of semiconductors have historically been crucial to advance their photovoltaic performance.

Central to the physics of organic semiconductors is a unique photoexcited species known as the charge-transfer state. The succeeding chapters is dedicated to understanding the role of the charge-transfer state in the working mechanism and thus performance of OSCs. In the following sections of this chapter, I first review the working mechanisms of organic photovoltaics, followed by material development that aims to improve efficiencies of photophysical events. I then discuss the origins of energy loss in OSCs.

Understanding of these topics prompts the research questions that are studied in detail in Chapters 2 through 4:

1. What are the kinetics of charge generation upon photoexcitation of non-fullerene acceptors in OPVs?

2. What is the lower limit for non-radiative recombination loss in charge transfer-based organic donor/acceptor blends?

3. What is the origin for low non-radiative recombination loss in OPV blends incorporating emissive non-fullerene acceptors?

These topics are crucial to improving charge generation efficiency and suppressing charge recombination loss to realize more efficient OSCs.

1.1 Mechanism of organic solar cells

The working principles of an OSC, or organic photovoltaic (OPV) device, involve a series of electronic processes. Broadly, it can be described in four steps: photon absorption, charge generation, charge recombination and charge collection, as shown in **Figure 1.1**. Efficiency of these photophysical processes and thus the overall photovoltaic performance of the solar cell is determined by the fate of the photogenerated species.

Due to low dielectric constants of organic molecules (ϵ~2-4), photoexcitation of organic molecules results in strongly bound electron-hole pairs, known as Frenkel-type excitons.[1] This is unlike photoexcitation of inorganic materials, where electrons and holes can readily dissociate into free carriers. For photovoltaic applications, the nature of excitons in organic molecules requires efficient pathways to overcome the coulombic interaction between the electron and hole to generate charges.

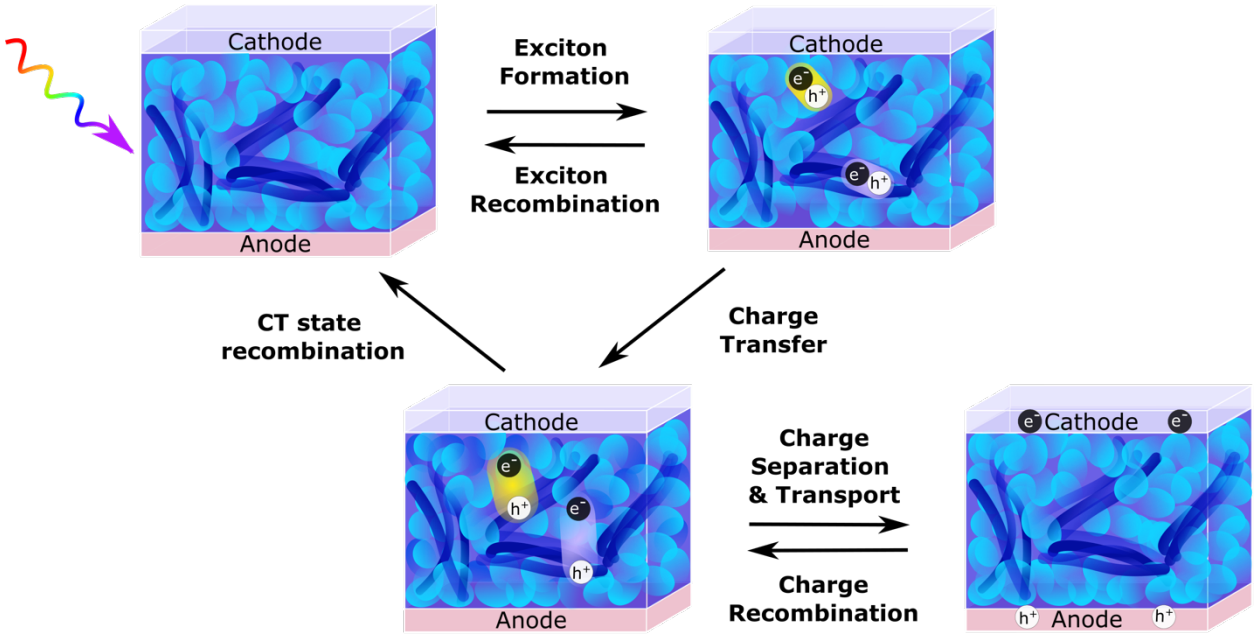

Figure 1.1 Operating principle of organic solar cells in an anode/BHJ/cathode model structure. The blue ellipse represents the NFA molecule, and the purple rod represents the polymer donor. Excitons form upon absorption of light, then migrates to the D/A interface and forms charge-transfer states. CT states can separate into free electrons and holes, which can transport to and be extracted by the electrodes. For each step towards charge extraction, a reverse process, i.e., recombination, can happen that leads to energy loss.

In 1986, C.W. Tang demonstrated a bilayer photovoltaic device using copper phthalocyanine and a perylene polymer derivative.[2] However, a bilayer structure is doomed to give inferior photovoltaic performance.[3] The photogenerated excitons have relatively short diffusion lengths on the order of 10 nm. In order for excitons to reach the donor/acceptor interface, the thickness of the absorbing material is limited, and consequently photon absorption suffers. A breakthrough in the 1990s solved this conundrum when Alan Heeger reported an absorbing layer spin-cast from a mixture of polymer as the electron donor and fullerene molecules as the electron acceptor, known as a bulk heterojunction (BHJ).[4] The nanoscale mixture in the BHJ architecture results in higher interface density between donor and acceptor materials.[5] As a result, a greater number of excitons are generated near the donor/acceptor interface, leading to increased charge generation.

In a BHJ OPV device, following photon absorption, an exciton in either donor or acceptor material diffuses to the donor/acceptor interface. At this point, the electron on the excited donor or hole in the excited acceptor can transfer the charge to the ground state of the acceptor or donor respectively, thereby forming a coulombically-bound electron-hole pair localized in the donor and acceptor materials, known as the charge-transfer (CT) state. Fundamentally, the CT state results from the interaction between the wavefunctions of the donor and acceptor material in their excited and ground states.[6]

As an intermediate between the exciton and fully dissociated charges, the fate of CT states governs charge generation and recombination.[7] Ideally, CT states dissociate into free electrons and holes, which can be extracted at the electrode to generate current. However, CT states can also recombine before forming free carriers and free carrier can also recombine with CT state (back arrows in **Figure 1.1**). These undesirable processes lead to a significant amount of energy losses in organic solar cells,[8,9] as discussed in detail in Section 1.4 and 1.5. The final step in OPV operation is charge extraction of the photogenerated carriers at the electrode. In an efficient solar cell, charge extraction must out-compete charge recombination. Many research efforts have focused on optimization of the energetics between the absorbing material and electrode via building energy cascades or improving morphology.[3]

1.2 Material development of OPV

In BHJ OSCs, fullerenes have been commonly used as the electron acceptor material mixed with polymer donors.[10–13] Due to highly symmetrical structure, fullerenes possess a number of advantageous properties.[14] Because the lowest unoccupied molecular orbitals (LUMOs) are delocalized across the entire 3D surface, isotropic and efficient charge transport can be achieved. This results in nanoscale pure fullerene domains in the polymer/fullerene BHJ blend within the diffusion length of the exciton, which is beneficial for efficient exciton splitting.[15]

Fullerenes also have significant drawbacks.[14] Due to its highly symmetrical structure, optical transitions are largely forbidden, limiting absorption in the UV-visible range of the solar spectrum. Less symmetrical fullerene acceptors such as $PC_{70}BM$ and its derivative have been designed, but the synthetic yield of such molecules is considerably low. Second, fullerene molecules have low optical tunability. The 3D cage structure makes it difficult to modify the frontier orbital energies. Consequently, when blended with a polymer, optical absorption and photocurrent generation are limited. Lastly, the morphology of polymer/fullerene is unstable and requires fine control to achieve efficient photovoltaic performance. Although pure fullerene domains are beneficial for exciton splitting, larger aggregates beyond the exciton diffusion length can form over time, thereby leading to exciton and carrier decay before reaching the donor/acceptor interface or the electrode.

Research efforts have focused on synthetic strategies on the polymer donor and morphological control to mitigate the aforementioned challenges.[5,12,16] Large-gap polymer donors have been developed to compensate for fullerene's low optical absorption. Via hybridization of the electron-donating and electron-accepting units in the polymer chain, namely push-pull hybridization, small-gap polymer donors such as PTB7-Th have been demonstrated. Other strategies include using high boiling-point solvent additive to control morphology[17] and adding a second polymer molecule to enhance photon absorption.[18] These efforts lead to over 10% power-conversion efficiency.

Until recently, strategically designed electron accepting materials replaced the fullerene acceptors.[5,19,20] The development of new non-fullerene acceptors (NFAs) has advanced the performance of organic photovoltaics, with power conversion efficiencies (PCEs) now approaching over 18%.[21] Compared to fullerene acceptors, NFAs have a number of attractive properties that not only benefit the solar cell efficiency but also prompt new photophysical questions.

1. Most NFAs contain electron-donating and electron-accepting units, thus rendering strong absorption in the visible-near IR region. This not only appreciably enhances photon absorption in

the solar cell, but also complements the absorption profile of wide-gap polymer donors. When NFA molecule is photoexcited, a significant number of excitons can charge-transfer to the polymer donor, forming charge-transfer states which can dissociate into photocarriers. Charge generation via hole-transfer from the acceptor molecule has been a previously overlooked topic polymer/fullerene OPVs because of fullerene's inferior photon absorption. We examine in detail the kinetics of hole transfer from NFA to polymer donor in Chapter 2.

2. Polymer/NFA blends can achieve small energetics offset between low gap exciton and charge-transfer state due to NFA's readily tunable bandgap. Energetics of the CT state including its adiabatic energy and the energetic offset with the low gap exciton largely determine the energy loss in organic solar cell. This topic will be discussed in detail in the next section.

3. Small non-symmetrical acceptors could lead to a highly intermixed morphology, which requires novel morphological control to ensure efficient exciton splitting and charge transport.

Overall, the development of NFAs push the field into higher photovoltaic performance. Understanding of the kinetics and thermodynamics of photophysical processes and the governing molecular properties is crucial to further improvement of organic solar cells.

1.3 Energy loss in organic solar cells

To achieve high efficiency, a solar cell must minimize the energy loss in photon-to-electron conversion. In this section, we review origins for energy loss processes in an organic solar cell and analytical methods for determining the loss terms, as this understanding is crucial for material and device design.

Overall, the total energy loss of an OPV device is defined as the energy difference between the energies of the low gap exciton (E_{S1}) and the free carriers ($E_{carrier}$), shown in Eqn. 1.1. In the solar cell research community, $E_{carrier}$ is commonly described via the concept of open-circuit voltage (V_{OC}), which is the maximum voltage a solar cell can output. Energy loss in an ideal solar cell is described by the Shockley-Queisser theory. Shockley and Queisser assume that an ideal solar cell where (1) absorptance is step-like, i.e. total absorption above step-like bandgap, and zero below), (2) only radiative recombination is present, and (3) all generated electrons are collected.[22] In this regime, the maximum voltage output can be predicted based on the bandgap of the solar cell and is thus known as Shockley-Queisser voltage limit ($V_{OC,\,SQ}$). Nevertheless, a real solar cell suffers from excess loss processes due to: (1) less-than-1 charge generation efficiency, (2) broad bandgap leading to additional radiative recombination, (3) molecular vibration and structural defects giving rise to significant non-radiative recombination loss. Thus, the energy loss, or the open-circuit voltage loss (ΔV_{OC}) in a solar cell can be separated into energy lost from charge generation from excitons of the donor and acceptor to form charge-transfer states ($\Delta V_{charge-gen}$), and energy lost from radiative and non-radiative recombination of charge-transfer states[1] (ΔV_{rad}, ΔV_{nrad}), as shown in Eqn. 1.2 and Eqn. 1.3.[8]

[1] This includes recombination of free carrier, as charge-transfer state is the intermediate between exciton and free carriers. The recombination of free carriers is non-geminate and bi-molecular, whereas charge-transfer recombination is geminate or mono-molecular.

In the next few paragraphs, we describe the sources of each loss term and ways to reduce loss.

$$\Delta E = E_{S1} - E_{carrier} \qquad \text{Eqn. 1.1}$$

$$\Delta E = \Delta E_{charge-gen} + \Delta E_{rad} + \Delta E_{nrad} \qquad \text{Eqn. 1.2}$$

$$\Delta V_{OC} = \Delta V_{charge-gen} + \Delta V_{rad} + \Delta V_{nrad} \qquad \text{Eqn. 1.3}$$

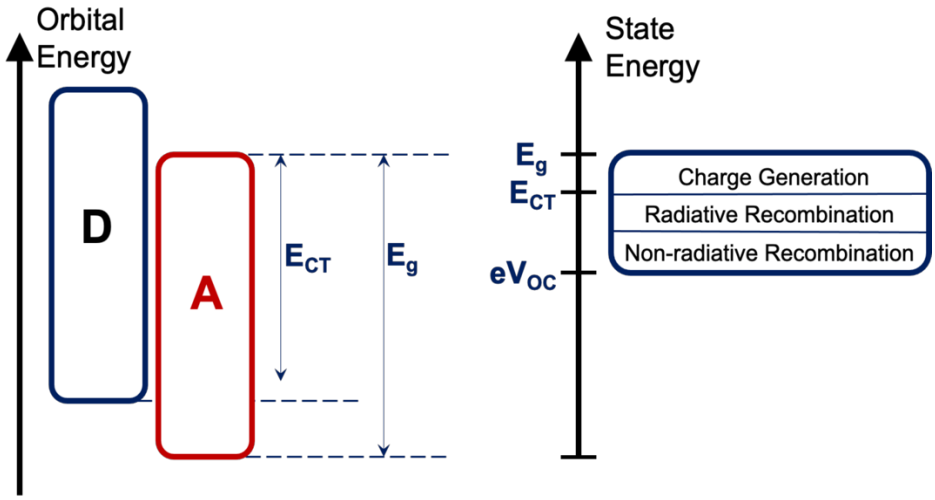

Figure 1.2 Energetics of organic solar cell. The left panel shows the orbital energies of the donor (D) and acceptor (A) molecule and the energies of the bandgap and the CT-state in the corresponding D/A blend. The right panel shows the state energy and sources of energy loss in an OPV device.

Charge generation loss

The energetic offset between the donor and acceptor molecule directly relates to the charge generation loss. As **Figure 1.2** shows, HOMO and LUMO energy differences between the donor and acceptor molecules govern the E_{S1}-E_{CT} offset, which can be tuned by modulating the chemical structures of the donor and acceptor molecules. As S1 and CT energies come closer, "driving force" for exciton dissociation is reduced. Traditionally, this is considered detrimental to the charge transfer efficiency because significant energy is thought to be required to overcome the coulombic interaction between the electron and the hole in the exciton. However, many reports have demonstrated efficient power-conversion efficiency in donor/acceptor blends with minimal S1-CT offset.[23–26] Furthermore, modulating the offset energy also influences the vibronic coupling between the S1 and CT and hot exciton dissociation.[27,28]

The optical bandgap E_{S1} can be determined by three methods.[29] The most common method uses the onset of the absorption or the photoaction spectrum. A more well-defined estimation is to use the intersection between the normalized absorption and emission spectra. Lastly, the optical bandgap can be determined via the photoaction spectrum. This method accounts for the interference effect of transport layers and electrode on the bandgap in a device. Analytically, the absorptance is interpreted as a superposition of a distribution of sharp step-functions, as described

by Shockley-Queisser, with different bandgap energies. Thus, the photovoltaic bandgap energy is the average bandgap energies in the distribution.

To determine the energy of the CT state, highly sensitive experimental methods are usually required. For polymer/fullerene blends, CT state lies lower in energy than the optical bandgap E_{S1}. This means that the CT state is visible in the absorption and emission spectra, but it only shows extremely weak features due to their low density of state and low oscillator strength.[6] Thus, photothermal deflection spectroscopy and Fourier-transform photocurrent spectroscopy are used to detect CT state.[22,30]

Radiative recombination loss

Detailed balance analysis shows that radiative recombination in solar cells is unavoidable. The solar cell has non-negligible absorption below the bandgap, which extends into the blackbody emission spectrum. Based on Kirchoff's radiation laws, a grey body when in thermal equilibrium with the ambient environment must emit an equivalent amount of radiation it absorbs.[31] In a real solar cell, sub-bandgap states such as the CT state result in excess thermal absorption, leading to unwanted radiative recombination. Radiative recombination loss can be reduced by sharpening the absorption band-edge. Polymer/fullerene blends has prominent radiative recombination loss, as CT states are low-lying relative to the low gap S1 state. Polymer/NFA blends has lower radiative recombination loss, as low as <0.1eV in the most efficient organic solar cells.[32] However, this is still significant compared to inorganic and perovskite solar cells. Details on radiative recombination loss calculation are included in Appendix B.

Non-radiative recombination loss

All non-radiative recombination processes lead to excess energy loss. These processes include a variety of events such as geminate and non-geminate transition of CT state to the ground-state, recombination via the triplet state, Auger recombination and morphological defects.[3] The luminescence efficiency of the solar cell under charge injection determines the non-radiative recombination loss as shown by Eqn. 1.4. A full derivation can be found in Appendix B.

$$q\Delta V_{nrad} = -kTln(EQE_{EL}) \quad \text{Eqn. 1.4}$$

Non-radiative recombination loss contributes significantly to the total energy loss in organic solar cells. This is 0.3-0.4 eV in polymer/fullerene blends and as low as 0.2 eV in polymer/NFA blends, compared to ~0.18 eV for commercial silicon,[33] 0.025 eV for GaAs cells[34] and 0.034 eV for emerging perovskite solar cells.[35]

Since CT state mediates charge generation and charge recombination (**Figure 1.1**), recent research efforts to reduce non-radiative recombination loss have focused on understanding the less-than-ideal radiative efficiency or luminescence efficiency (PLQY) of the CT state. As shown by Eqn. 1.5, PLQY of the CT state is determined by the fraction of radiative transition rate in the total rate.

Given the promising luminescence quantum efficiency achieved in organic light emitting diodes (OLEDs), it is perplexing what molecular properties limit the photoluminescence of charge-transfer states in OSCs, currently below 0.1%. Furthermore, we ask: what is the lower limit for non-radiative recombination loss in organic solar cells? This motivated the work presented in Chapter 3, where I study the photovoltaic performance and the photoluminescence properties of a

model OSC using an intrinsically emissive donor/acceptor blend. To approach this topic, I examine the theoretical frameworks that uncover the molecular properties governing PL properties of charge-transfer state. This understanding will provide insight for molecular design of OSCs with low energy loss.

1.4 Molecular origin for non-radiative recombination loss

Modeling CT recombination rates in the two-state electron transfer regime

As mentioned in the last section, when only non-radiative recombination loss from CT states is considered, the EQE_{EL} is related to the photoluminescence quantum efficiency of the CT state (Eqn 1.5). radiative and non-radiative recombination of CT states can be described as a two-state electron-transfer event between CT and ground-state via the Marcus-Levich-Jortner framework.[36] This scheme assumes that the electron that the electronic coupling between CT and ground-state is much larger than that between CT and local exciton, as shown in **Error! Reference source not found.**.**3**.

$$PLQY = \frac{k_r}{k_r + k_{nr}} \qquad \text{Eqn. 1.5}$$

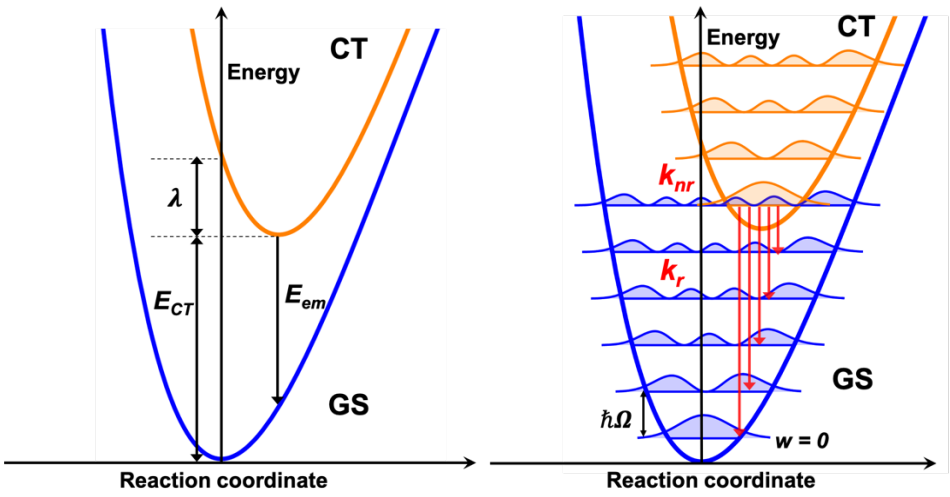

Figure 1.3 Potential energy surfaces of CT (orange) and ground-state (blue). Left diagram shows a semi-classical description and the right shows a quantum mechanical model, where vibrational levels and wavefunctions are shown. Radiative transitions are indicated by red arrows and non-radiative transitions are shown as vibrational wavefunction overlap. Total reorganization energy is denoted as λ, emission energy of highest intensity as E_{em} and vibrational spacing as $\hbar\Omega$.

In the framework of semi-classical two-state model (**Figure 1.3** on the right), the non-radiative recombination rate is written as the electron transfer rate constant given by the Marcus equation: $k_{nr} = \frac{2\pi}{\hbar} V^2 \frac{1}{\sqrt{4\pi\lambda_{CT} k_B T}} \exp\left(-\frac{(E_{CT}-\lambda_{CT})^2}{4k_B T \lambda_{CT}}\right)$, where V^2 is the electronic coupling between ground-state and CT state, and λ_{CT} is the reorganization energy being the sum of *inter*molecular

reorganization (reflecting structural rearrangements upon de-excitation of CT) and *intra*molecular reorganization due to vibrations of the molecule. In addition, intramolecular phonon modes must be treated quantum-mechanically, given that intramolecular phonon modes are "frozen" ($\hbar\omega_{intra}$ ~300-3000cm^{-1}) at room temperature and only intermolecular phonon modes ($\hbar\omega_{inter}$~10-100cm^{-1}) are activated.[36] Since $\hbar\omega_{inter} \ll k_B T \ll \hbar\omega_{intra}$, intramolecular phonon modes must be treated quantum-mechanically,[37,38] and thus, within the Born-Oppenheimer approximation and Fermi Golden Rule limits, the non-radiative transition rate can be written as

$$k_{nr} = \frac{2\pi}{\hbar} V^2 FCWD \quad \text{Eqn. 1.6}$$

where FCWD (Franck-Condon weighted density of states) factor accounts for transitions between all vibrational levels of CT and ground-states (**Figure 1.3** on the left).

Here, Assuming CT and ground-state have equal intramolecular phonon modes ($\hbar\Omega$), it has been shown that the overlap integral squared between two vibronic states $\psi_{a\alpha}$ and $\psi_{b\beta} < \psi_{a\alpha}|\psi_{b\beta} >^2$, describing the transition probability, reduces to $\frac{e^{-S} S^{w-t} t!}{w!} [L_t^{w-t}(S)]^2$,[39] S is the Huang-Rhys factor , $S = \frac{\lambda_{qm}}{\hbar\omega}$, where $\hbar$ is the intramolecular phonon mode energy, t and w are the vibrational quantum numbers for the ground-state and CT state, respectively, and $L_t^{w-t}(S)$ is the generalized Laguerre polynomial. The initial density of states at a particular vibrational level, t, of the CT state follows the Boltzmann distribution, and the density of population with energy required for the transition from the initial vibrational level of the CT state to the ground-state vibrational level, while satisfying energy conservation, is described as a delta function. At room temperature, we can safely only consider transitions from the relaxed CT states to all w vibrational levels. Taken together, we write FCWD for non-radiative transition rate as

$$FCWD(0) = \frac{1}{\sqrt{4\pi\lambda_c k_B T}} \sum_{w=0}^{\infty} \frac{e^{-S} S^w}{w!} [L_0^w(S)]^2 e^{\frac{-(E_{CT} - \lambda_c - w\hbar\Omega)^2}{4\lambda_c k_B T}} \quad \text{Eqn. 1.7}$$

where the factor before the sum represents the classical density of states.

Radiative transition can be modeled as spontaneous emission with probability density of $< \psi_{a\alpha}|\vec{\mu}|\psi_{\beta\beta} >^2$. Using the MLJ approach, we then write the radiative rate constant at a particular photon energy $k_r(\hbar\omega)$ and integrate over photon energies to obtain the total radiative rate K_r (Eqn. 1.9). Based on generalized Mulliken-Hush approach, the transition dipole moment (M) is related to the electronic coupling (V) and change in dipole moment $\Delta\mu$.[40,41]

$$k_r(\hbar\omega) = \frac{1}{3\pi\epsilon_0\hbar^4} \left(\frac{\hbar\omega}{c}\right)^3 M^2 FCWD(\hbar\omega) \left[6.94 \times 10^{-41} \frac{C^2 s^2 kg^{-1} eV}{D^2}\right] \text{Eqn. 1.8}$$

$$K_r = \int k_r(\hbar\omega)\, d\hbar\omega \quad \text{Eqn. 1.9}$$

Using this model, it has been shown that both the radiative and non-radiative transition rates of the CT state follow an "energy-gap law," where higher CT energy has faster decay rates. More importantly, the non-radiative recombination loss also follows this trend, where higher CT energy renders lower loss. Besides the CT energy, non-radiative recombination is sensitive to the vibronic overlap between the CT and ground state.[28,42] This means that non-radiative recombination loss can be mitigated by tuning the CT energetics relative to the ground-state, including the reorganization energy, CT adiabatic energy, electronic overlap between the CT and the ground-state, and the transition dipole moment.

These trends provide important insights for molecular design of high PLQY organic systems for low voltage loss OPVs. Interestingly, when CT presumes a high adiabatic energy, the non-radiative recombination rate is extremely sensitive to modifications in the molecular properties.[43] The consequence of this is two-fold: (1) It is extremely important to cross-check molecular properties obtained from experiments and theoretical calculation. Failure to do so leads to either molecular properties with no physical meaning or misinterpretation of the physical nature of charge recombination in an organic system. (2) CT-LE mixing may impede high PLQY of CT because mixing can also increase the non-radiative transition rate. These topics are studied in Chapter 3.

Beyond Marcus-Levich-Jortner two-state model

As discussed in Section 1.2, frontier orbital energies of NFAs can be tuned to raise the energy of CT state. This is a common strategy to mitigate the S1-CT energy offset, suppressing energy loss from charge generation. Recently, several polymer/NFA blends with small ΔE_{S1-CT} exhibits lower non-radiative recombination loss than what MLJ model would predict.[44,45] Theoretical work attributes this finding to wavefunction mixing between the S1 and CT state that becomes significant when CT and ground-state are close in energy.[27,45] In the context of OPV, CT-LE mixing is beneficial because CT state can borrow the emission intensity from an emissive NFA, thereby enhancing electroluminescence and reduce non-radiative recombination loss. In Chapter 4, I propose an experimental method for directly probing wavefunction mixing in OPV blends with small S1-CT energy offset. However, CT-LE mixing can hurt PLQY of large gap CT states, as I will discuss in Chapter 3.

References

(1) Pope, M.; Swenberg, H. E. *Electronic Processes in Organic Crystals and Polymers*, Second Ed.; 1999.

(2) Tang, C. W. Two-Layer Organic Photovoltaic Cell. *Appl. Phys. Lett.* **1986**, *48* (2), 183–185. https://doi.org/10.1063/1.96937.

(3) Karki, A.; Gillett, A. J.; Friend, R. H.; Nguyen, T. Q. The Path to 20% Power Conversion Efficiencies in Nonfullerene Acceptor Organic Solar Cells. *Adv. Energy Mater.* **2020**, *2003441*, 1–30. https://doi.org/10.1002/aenm.202003441.

(4) Yu, G.; Gao, J.; Hummelen, J. C.; Wudl, F.; Heeger, A. J. Polymer Photovoltaic Cells: Enhanced Efficiencies via a Network of Internal Donor-Acceptor Heterojunctions. *Science (80-.).* **1995**, *270* (5243), 1789. https://doi.org/10.1126/science.270.5243.1789.

(5) Wadsworth, A.; Moser, M.; Marks, A.; Little, M. S.; Gasparini, N.; Brabec, C. J.; Baran, D.; McCulloch, I. Critical Review of the Molecular Design Progress in Non-Fullerene Electron Acceptors towards Commercially Viable Organic Solar Cells. *Chem. Soc. Rev.* **2019**, *48* (6), 1596–1625. https://doi.org/10.1039/c7cs00892a.

(6) Coropceanu, Veaceslav; Chen, Xian-Kai; Wang, Tonghui; Zheng, Zilong; Bredas, J.-L. Charge-Transfer Electronic States in Organic Solar Cells. *Nat. Rev. Mater.* **2019**. https://doi.org/10.1038/s41578-019-0137-9.

(7) Liu, X.; Rand, B. P.; Forrest, S. R. Engineering Charge-Transfer States for Efficient , Low-Energy-Loss Organic Photovoltaics. *Trends Chem.* **2019**, *1* (9), 815–829. https://doi.org/10.1016/j.trechm.2019.08.001.

(8) Menke, S. M.; Ran, N. A.; Bazan, G. C.; Friend, R. H. Understanding Energy Loss in Organic Solar Cells: Toward a New Efficiency Regime. *Joule* **2018**, *2* (1), 25–35. https://doi.org/10.1016/j.joule.2017.09.020.

(9) Benduhn, J.; Tvingstedt, K.; Piersimoni, F.; Ullbrich, S.; Fan, Y. L.; Tropiano, M.; McGarry, K. A.; Zeika, O.; Riede, M. K.; Douglas, C. J.; Barlow, S.; Marder, S. R.; Neher, D.; Spoltore, D.; Vandewal, K. Intrinsic Non-Radiative Voltage Losses in Fullerene-Based Organic Solar Cells. *Nat. Energy* **2017**, *2*. https://doi.org/Artn 17053 10.1038/Nenergy.2017.53.

(10) He, Y.; Li, Y. Fullerene Derivative Acceptors for High Performance Polymer Solar Cells. *Phys. Chem. Chem. Phys.* **2011**, *13* (6), 1970–1983. https://doi.org/10.1039/c0cp01178a.

(11) Li, Y. Molecular Design of Photovoltaic Materials for Polymer Solar Cells: Toward Suitable Electronic Energy Levels and Broad Absorption. *Acc. Chem. Res.* **2012**, *45* (5), 723–733. https://doi.org/10.1021/ar2002446.

(12) Liang, Y.; Yu, L. A New Class of Semiconducting Polymers for Bulk Heterojunction Solar Cells with Exceptionally High Performance. *Acc. Chem. Res.* **2010**, *43* (9), 1227–1236. https://doi.org/10.1021/ar1000296.

(13) Liao, S. H.; Jhuo, H. J.; Cheng, Y. S.; Chen, S. A. Fullerene Derivative-Doped Zinc Oxide Nanofilm as the Cathode of Inverted Polymer Solar Cells with Low-Bandgap Polymer (PTB7-Th) for High Performance. *Adv. Mater.* **2013**, *25* (34), 4766–4771.

https://doi.org/10.1002/adma.201301476.

(14) Yan, C. Q.; Barlow, S.; Wang, Z. H.; Yan, H.; Jen, A. K. Y.; Marder, S. R.; Zhan, X. W. Non-Fullerene Acceptors for Organic Solar Cells. *Nat. Rev. Mater.* **2018**, *3*. https://doi.org/Artn 18003 10.1038/Natrevmats.2018.3.

(15) Yang, X.; Loos, J.; Veenstra, S. C.; Verhees, W. J. H.; Wienk, M. M.; Kroon, J. M.; Michels, M. A. J.; Janssen, R. A. J. Nanoscale Morphology of High-Performance Polymer Solar Cells. *Nano Lett.* **2005**, *5* (4), 579–583. https://doi.org/10.1021/nl048120i.

(16) Liang, Y.; Wu, Y.; Feng, D.; Tsai, S. T.; Son, H. J.; Li, G.; Yu, L. Development of New Semiconducting Polymers for High Performance Solar Cells. *J. Am. Chem. Soc.* **2009**, *131* (1), 56–57. https://doi.org/10.1021/ja808373p.

(17) Zhao, J.; Li, Y.; Yang, G.; Jiang, K.; Lin, H.; Ade, H.; Ma, W.; Yan, H. Efficient Organic Solar Cells Processed from Hydrocarbon Solvents. *Nat. Energy* **2016**, *1* (2). https://doi.org/10.1038/NENERGY.2015.27.

(18) Khlyabich, P. P.; Burkhart, B.; Thompson, B. C. Efficient Ternary Blend Bulk Heterojunction Solar Cells with Tunable Open-Circuit Voltage. *J. Am. Chem. Soc.* **2011**, *133* (37), 14534–14537. https://doi.org/10.1021/ja205977z.

(19) Lin, Y.; Wang, J.; Zhang, Z.-G.; Bai, H.; Li, Y.; Zhu, D.; Zhan, X. An Electron Acceptor Challenging Fullerenes for Efficient Polymer Solar Cells. *Adv. Mater.* **2015**, *27* (7), 1170–1174. https://doi.org/10.1002/adma.201404317.

(20) Yan, C.; Barlow, S.; Wang, Z.; Yan, H.; Jen, A. K. Y.; Marder, S. R.; Zhan, X. Non-Fullerene Acceptors for Organic Solar Cells. *Nat. Rev. Mater.* **2018**, *3*, 18003–18021. https://doi.org/10.1038/natrevmats.2018.3.

(21) NREL. National Renewable Energy Laboratory Research Cell Efficiency Chart https://www.nrel.gov/pv/cell-efficiency.html (accessed May 14, 2020).

(22) Yao, J.; Kirchartz, T.; Vezie, M. S.; Faist, M. A.; Gong, W.; He, Z.; Wu, H.; Troughton, J.; Watson, T.; Bryant, D.; Nelson, J. Quantifying Losses in Open-Circuit Voltage in Solution-Processable Solar Cells. *Phys. Rev. Appl.* **2015**, *014020*, 1–10. https://doi.org/10.1103/PhysRevApplied.4.014020.

(23) Liu, Y.; Zuo, L.; Shi, X.; Jen, A. K. Y.; Ginger, D. S. Unexpectedly Slow Yet Efficient Picosecond to Nanosecond Photoinduced Hole-Transfer Occurs in a Polymer/Nonfullerene Acceptor Organic Photovoltaic Blend. *ACS Energy Lett.* **2018**. https://doi.org/10.1021/acsenergylett.8b01416.

(24) Unger, T.; Wedler, S.; Kahle, F. J.; Scherf, U.; Bässler, H.; Köhler, A. The Impact of Driving Force and Temperature on the Electron Transfer in Donor-Acceptor Blend Systems. *J. Phys. Chem. C* **2017**, *121* (41), 22739–22752. https://doi.org/10.1021/acs.jpcc.7b09213.

(25) Liu, J.; Chen, S.; Qian, D.; Gautam, B.; Yang, G.; Zhao, J.; Bergqvist, J.; Zhang, F.; Ma, W.; Ade, H.; Inganäs, O.; Gundogdu, K.; Gao, F.; Yan, H. Fast Charge Separation in a Non-Fullerene Organic Solar Cell with a Small Driving Force. *Nat. Energy* **2016**, *1* (7), 16089–16095. https://doi.org/10.1038/nenergy.2016.89.

(26) Nakano, K.; Chen, Y.; Xiao, B.; Han, W.; Huang, J.; Yoshida, H.; Zhou, E.; Tajima, K. Anatomy of the Energetic Driving Force for Charge Generation in Organic Solar Cells. *Nat.*

Commun. **2019**, *10* (1), 1–10. https://doi.org/10.1038/s41467-019-10434-3.

(27) Chen, X. K.; Coropceanu, V.; Bredas, J. L. Assessing the Nature of the Charge-Transfer Electronic States in Organic Solar Cells. *Nat. Commun.* **2018**, *9*. https://doi.org/Artn 5295 10.1038/S41467-018-07707-8.

(28) Panhans, M.; Hutsch, S.; Benduhn, J.; Schellhammer, K. S.; Nikolis, V. C.; Vangerven, T.; Vandewal, K.; Ortmann, F. Molecular Vibrations Reduce the Maximum Achievable Photovoltage in Organic Solar Cells. *Nat. Commun.* **2020**, *11* (1), 1–10. https://doi.org/10.1038/s41467-020-15215-x.

(29) Wang, Y.; Qian, D.; Cui, Y.; Zhang, H.; Hou, J.; Vandewal, K.; Kirchartz, T.; Gao, F. Optical Gaps of Organic Solar Cells as a Reference for Comparing Voltage Losses. *Adv. Energy Mater.* **2018**, 1801352. https://doi.org/10.1002/aenm.201801352.

(30) Buchaca-Domingo, E.; Vandewal, K.; Fei, Z.; Watkins, S. E.; Scholes, F. H.; Bannock, J. H.; De Mello, J. C.; Richter, L. J.; DeLongchamp, D. M.; Amassian, A.; Heeney, M.; Salleo, A.; Stingelin, N. Direct Correlation of Charge Transfer Absorption with Molecular Donor:Acceptor Interfacial Area via Photothermal Deflection Spectroscopy. *J. Am. Chem. Soc.* **2015**, *137* (16), 5256–5259. https://doi.org/10.1021/ja512410f.

(31) Rau, U. Reciprocity Relation between Photovoltaic Quantum Efficiency and Electroluminescent Emission of Solar Cells. *Phys. Rev. B* **2007**, *76* (8), 1–8. https://doi.org/10.1103/PhysRevB.76.085303.

(32) Liu, S.; Yuan, J.; Deng, W.; Luo, M.; Xie, Y.; Liang, Q.; Zou, Y.; He, Z.; Wu, H.; Cao, Y. High-Efficiency Organic Solar Cells with Low Non-Radiative Recombination Loss and Low Energetic Disorder. *Nat. Photonics* **2020**. https://doi.org/10.1038/s41566-019-0573-5.

(33) Kirchartz, T.; Rau, U.; Kurth, M.; Mattheis, J.; Werner, J. H. Comparative Study of Electroluminescence from Cu(In,Ga)Se2 and Si Solar Cells. *Thin Solid Films* **2007**, *515* (15 SPEC. ISS.), 6238–6242. https://doi.org/10.1016/j.tsf.2006.12.105.

(34) Green, M. A.; Dunlop, E. D.; Hohl-Ebinger, J.; Yoshita, M.; Kopidakis, N.; Ho-Baillie, A. W. Y. Solar Cell Efficiency Tables (Version 55). *Prog. Photovoltaics Res. Appl.* **2020**, *28* (1), 3–15. https://doi.org/10.1002/pip.3228.

(35) Yoo, J. J.; Wieghold, S.; Sponseller, M. C.; Chua, M. R.; Bertram, S. N.; Hartono, N. T. P.; Tresback, J. S.; Hansen, E. C.; Correa-Baena, J. P.; Bulović, V.; Buonassisi, T.; Shin, S. S.; Bawendi, M. G. An Interface Stabilized Perovskite Solar Cell with High Stabilized Efficiency and Low Voltage Loss. *Energy Environ. Sci.* **2019**, *12* (7), 2192–2199. https://doi.org/10.1039/c9ee00751b.

(36) Engleman, R.; Jortner, J. The Energy Gap Law for Radiationless Transitions in Large Molecules. *Mol. Phys.* **1970**, *18* (2), 145–164.

(37) Barbara, P. F.; Meyer, T. J.; Ratner, M. A. Contemporary Issues in Electron Transfer Research. *J. Phys. Chem.* **1996**, *100* (31), 13148–13168. https://doi.org/10.1021/jp9605663.

(38) Jortner, J. Temperature Dependent Activation Energy for Electron Transfer between Biological Molecules. *J. Chem. Phys.* **1976**, *64* (12), 4860–4867. https://doi.org/10.1063/1.432142.

(39) Keil, T. H. Shapes of Impurity Absorption Bands in Solids. *Phys. Rev.* **1965**, *140* (2A), 601–

617. https://doi.org/10.1017/CBO9781107415324.004.

(40) Subotnik, J. E.; Yeganeh, S.; Cave, R. J.; Ratner, M. A. Constructing Diabatic States from Adiabatic States: Extending Generalized Mulliken-Hush to Multiple Charge Centers with Boys Localization. *J. Chem. Phys.* **2008**, *129* (24). https://doi.org/10.1063/1.3042233.

(41) Azzouzi, M.; Yan, J.; Kirchartz, T.; Liu, K. K.; Wang, J. L.; Wu, H. B.; Nelson, J. Nonradiative Energy Losses in Bulk-Heterojunction Organic Photovoltaics. *Phys. Rev. X* **2018**, *8*. https://doi.org/Artn 031055 10.1103/Physrevx.8.031055.

(42) Azzouzi, M.; Yan, J.; Kirchartz, T.; Liu, K.; Wang, J.; Wu, H.; Nelson, J. Nonradiative Energy Losses in Bulk-Heterojunction Organic Photovoltaics. *Phys. Rev. X* **2018**, *8* (3), 1–14. https://doi.org/10.1103/PhysRevX.8.031055.

(43) Cho, E.; Coropceanu, V.; Brédas, J. L. Organic Neutral Radical Emitters: Impact of Chemical Substitution and Electronic-State Hybridization on the Luminescence Properties. *J. Am. Chem. Soc.* **2020**, *142* (41), 17782–17786. https://doi.org/10.1021/jacs.0c08997.

(44) Qian, D.; Zheng, Z.; Yao, H.; Tress, W.; Hopper, T. R.; Chen, S.; Li, S.; Liu, J.; Chen, S.; Zhang, J.; Liu, X.; Gao, B.; Ouyang, L.; Jin, Y.; Pozina, G.; Buyanova, I. A.; Chen, W. M.; Inganäs, O.; Coropceanu, V.; Bredas, J.; Yan, H.; Hou, J.; Zhang, F.; Bakulin, A. A.; Gao, F. Design Rules for Minimizing Voltage Losses in High-Efficiency Organic Solar Cells. *Nat. Mater.* **2018**, *17*. https://doi.org/10.1038/s41563-018-0128-z.

(45) Eisner, F. D.; Azzouzi, M.; Fei, Z.; Hou, X.; Anthopoulos, T. D.; Dennis, T. J. S.; Heeney, M.; Nelson, J. Hybridization of Local Exciton and Charge-Transfer States Reduces Nonradiative Voltage Losses in Organic Solar Cells. *J Am Chem Soc* **2019**, *141*, 6362–6374. https://doi.org/10.1021/jacs.9b01465.

Chapter 2. Hole-transfer in a polymer/non-fullerene acceptor organic photovoltaic blend

Adapted with permission from Liu, Y.; Zuo, L.; Shi, X.; Jen, A. K.-Y.; Ginger, D. S. Unexpectedly Slow Yet Efficient Picosecond to Nanosecond Photoinduced Hole-Transfer Occurs in a Polymer/Nonfullerene Acceptor Organic Photovoltaic Blend. *ACS Energy Lett.* **2018**, 3, 2396– 2403, DOI: 10.1021/acsenergylett.8b01416.

2.1 Overview

We study photoinduced charge generation in a model polymer/non-fullerene acceptor organic photovoltaic (OPV) blend. Specifically, we focus on hole-transfer kinetics from the photoexcited non-fullerene acceptor (NFA) thiophene-thieno[3,2-*b*]thiophene-thiophene-3-(dicyanomethylidene)indan-1-one (4TIC) to the conjugated polymer donor poly[(4,4'-bis(2-butyloctoxycarbonyl-[2,2'-bithiophene]-5,5-diyl)-alt-(2,2'-bithiophene-5,5'-diyl)] (PDCBT) using ultrafast transient absorption and time-resolved photoluminescence spectroscopy. We measure the hole-transfer dynamics by selectively exciting the 4TIC electron acceptor and monitoring the bleach of the PDCBT ground-state population. In the blend, we find that the 4TIC excitons decay with an average lifetime of 7 ps, accompanied by a concomitant rise in the ground-state bleach of the polymer with a comparable average lifetime that is 60% complete by 8 ps and 95% complete by 100 ps, occurring roughly an order of magnitude slower than in previously reported polymer/NFA blends. Notably, the ground-state bleach of the polymer continues to grow, not reaching its maximum until ~1 ns. To explain this long tail in the ground-state bleach rise, we propose that some 4TIC charge-transfer-like excitons are generated, which undergo hole-transfer to the polymer on the 100 ps-1 ns time-scale. Our findings provide new insight into the kinetics of hole-transfer in non-fullerene OPV blends in the regime of small driving force and also support the proposal that non-fullerene acceptors may generate long-lived charge species upon direct photoexcitation.

2.2 Introduction

The development of new non-fullerene acceptors (NFAs) has advanced the performance of organic photovoltaics (OPVs)[1–3] and reinvigorated the field, with efficiencies now climbing over 14%.[2] Compared to fullerene acceptors, NFAs have several notable properties.[4–6] First, NFAs have larger absorption cross-sections than fullerenes that facilitate more efficient light harvesting.[3,4] Second, unlike fullerenes, NFAs can have extended absorption into the near-infrared (nIR) wavelengths, thereby complementing the absorption of the polymers.[1] With such absorption profiles, electron transfer from the photoexcited polymer donor to the NFA, and hole-transfer from the photoexcited NFA to the polymer donor, can both contribute to charge generation. Third, the energy levels of NFAs can be readily tuned to match with those of the polymer donor to minimize open-circuit voltage loss (V_{OC}).[1,4] Finally, and perhaps most importantly, while fullerenes exhibit intrinsically low photoluminescence quantum efficiencies which consign polymer/fullerene cells to large non-radiative recombination losses, NFAs can in principle avoid this loss, possibly allowing them to achieve higher V_{OC} and thus close the performance gap with inorganic photovoltaics.[7–10]

However, these unique properties can also give rise to different charge generation and recombination dynamics in polymer/NFA OPVs compared to fullerene systems. Because of an organic NFA's significant contribution to light absorption, it is of particular interest to investigate the mechanism and dynamics of hole-transfer from the NFA to the polymer electron donor. Most recent reports have shown efficient hole-transfer in multiple polymer/NFA systems occurring on ultrafast timescales,[11–13] with excitons formed at the donor/acceptor interface dissociating within 1 ps. Slower hole-transfer (~1-2 ps) then occurs following exciton diffusion from the pure acceptor region to the interface. These observations appear broadly consistent with the ultrafast charge generation reported in many fullerene-based OPVs.[14–20] In contrast, delayed charge generation has also been suggested in a limited number of polymer/NFA blends.[10,21–23] Furthermore, in terms of energetics, the necessity of a large enthalpic driving force, as often required by the majority of efficient polymer/fullerene systems, has been challenged in newer studies of polymer/NFA systems.[7–10,21,22]

Herein, we investigate charge generation via hole-transfer from the NFA to a conjugated polymer donor in a model OPV system. This system, a blend of PDCBT and 4TIC, has minimal driving force for hole-transfer yet good photon-to-charge conversion efficiency. Importantly, this system also has clearly separated absorption bands, allowing for selective excitation of the 4TIC NFA, and selective monitoring of polymer donor's ground-state signatures, providing clean kinetics for analysis. We study the dynamics and efficiency of hole-transfer in the PDCBT:4TIC blend by selectively exciting 4TIC and monitoring the ground-state bleach (GSB) of PDCBT and the decay of the 4TIC exciton. We find that only 60% of hole-transfer is completed by 8 ps, with 95% completed by 100 ps, and the last 5% of hole transfer occurring very slowly between 100 ps and 1 ns. Hole transfer here is thus more than an order of magnitude slower than charge generation in other efficient polymer/NFA OPV systems, yet still highly efficient (~90% quantum yield). To explain these complex kinetics, we propose that some of the initial photoexcitations immediately dissociate into polymer/acceptor charge-transfer (CT) states while other photoexcitations result in CT excitons in the pure NFA region which ultimately transfers the hole polaron to the polymer over different timescales.

2.3 Photovoltaic properties of PDCBT:4TIC blend

Figure 2.1a shows the structures and the ionization potential (IP) and electron affinity (EA) energy levels of PDCBT and 4TIC estimated via cyclic voltammetry measurements on films, combined with the measured optical bandgaps. Jen and co-workers designed the 4TIC molecule based on ITIC, a widely used NFA that has shown good device performance when blended with various polymers.[24] Compared to ITIC, the core donor unit is replaced by a rigid and more electron-rich, fused-ring thiophene-thieno[3,2-*b*]thiophene-thiophene (4T), which we expect to give rise to stronger intramolecular charge transfer with the acceptor unit 3-(dicyanomethylidene)indan-1-one (IC).[24] Consequently, 4TIC has an extended absorption into the near-infrared (nIR) wavelengths compared to ITIC (**Figure 2.1b**, red). The donor PDCBT is a derivative of polythiophene (PT) and absorbs at shorter wavelengths (**Figure 2.1b**, black).[25,26] We determine the driving enthalpy for hole-transfer from the photoexcited NFA to the polymer donor to be ~-110meV (endergonic) – suggesting that hole-transfer should be slightly energetically unfavorable based solely on commonly used CV energetics and assuming only enthalpic terms (see Section 1 in the SI for details).[27]

Figure 2.1b shows the wavelength-resolved external quantum efficiency (EQE) spectrum for a ITO/PEDOT:PSS/PDCBT:4TIC (1:2 wt/wt)/bis-C_{60}/Ag device. The blend generates photocurrent efficiently across the absorption bands of both the 4TIC (~550-900 nm) and PDCBT (~450-650 nm), with an external quantum efficiency (EQE) as high as 53% in the 4TIC absorption wavelengths. The optical density of the blend film is 0.4-0.5 in the 4TIC absorption wavelengths suggesting that the internal quantum efficiency is over 50 % at these wavelengths, assuming a simple double pass approximation. This indicates a large fraction of 4TIC excitons dissociate to generate free charge efficiently. **Figure 2.1c** shows the full current-voltage curve for a typical device prepared from a PDCBT/4TIC blend. These devices show efficient photocurrent generation and collection, with a short-circuit current density (J_{SC}) of 16.6 mA/cm^2, a V_{OC} of 0.70 V, a fill factor of 60%, and an overall power conversion efficiency of 6.4±0.4% (averaged over 8 devices). Since 4TIC has a smaller bandgap than PDCBT, hole-transfer from 4TIC to PDCBT is the only possible pathway to create hole polarons on PDCBT following photon absorption by 4TIC. Our observation of efficient charge generation despite a slightly unfavorable driving force is broadly consistent with other reports of charge generation regardless of low (or even zero) energy offsets in polymer/NFA blends and serves to underscore the fact that the OPV field has reached the limits of using electrochemical- or photoemission-based measurements to determine driving forces. Since hole-transfer is obviously favorable, as seen by the device data in **Figure 2.1b-c** we propose that the CV-derived values of the driving force are uncertain either because (i) the EA and IP energy calculations from cyclic voltammetry measurements in solution differ from the values in the device due to effects such as the role of the counterion on the redox potentials of the organic materials,[28] (ii) IP and EA energies of the donor and acceptor molecules are modified in a bulk heterojunction structure,[29] or (iii) entropic terms play a role and we need to rely on free energies should be computed using a different formalism,[29–31] rather than simple enthalpic terms. While a discussion of these points is not our focus here, we highlight the small apparent driving force to highlight the similarity of this system with many recently reported materials.[8–10,22,32,33]

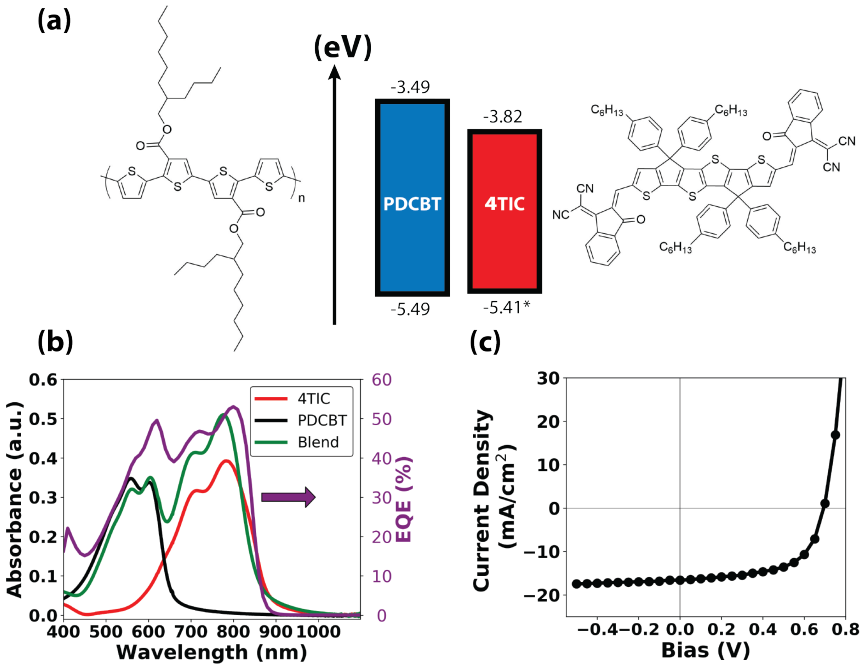

Figure 2.1(a) Molecular structures and IP and EA levels of the polymer donor PDCBT and the non-fullerene acceptor 4TIC. The IP and EA of PDCBT and IP of 4TIC were measured via cyclic

voltammetry on films. The EA of 4TIC was estimated based on the optical bandgap and the IP of the 4TIC film. **(b)** Absorption spectra of PDCBT, 4TIC, and PDCBT/4TIC (1:2 wt/wt) blend, and EQE of the optimized blend device. **(c)** Current density-voltage characterization of the optimized PDCBT/4TIC device under AM 1.5G illumination. Device structure: ITO/PEDOT:PSS/PDCBT:4TIC (1:2 wt/wt)/bis-C60/Ag.

2.4 Hole-transfer kinetics

Having established that efficient charge separation still takes place in PDCBT/4TIC blends, we next turn to explore the kinetics governing charge generation in this system. In all the following spectroscopic studies, we selectively excite 4TIC at 810 nm, where PDCBT does not absorb, to isolate hole-transfer from electron-transfer from donor to acceptor. In these experiments, energy-transfer is not possible because PDCBT has a larger bandgap than 4TIC, and we excite on the red edge of the 4TIC absorption band. We then monitor the kinetics of hole-transfer via the ground-state bleach of the PDCBT polymer.

We analyze the carrier dynamics following 4TIC excitation in PDCBT:4TIC blends and propose a mechanism to describe the kinetics. We use 810 nm pump laser with 2.5 $\mu J/cm^2$/pulse to selectively excite 4TIC in the blend film. We use low excitation fluences to avoid non-linear photophysics such as two-photon absorption, exciton-exciton, and exciton-charge annihilation, (See Appendix A **Figure S1**), as well as to keep the excitation density relevant to the working condition of a solar cell, on the order of 10^{17} excitations/cm^3 (see Appendix A Section 2 for excitation density calculations). **Figure 2.2** shows $-\Delta T/T$ transient absorption (TA) spectra at selected pump-probe delay times after photoexcitation, and kinetic traces of key photoexcited species (ps-ns). **Figure 2.2a** shows evidence for hole-transfer from 4TIC to PDCBT at 1 ps: a negative signal spans the entire visible spectrum, consistent with a bleach of the absorption of both PDCBT and 4TIC (**Figure 2.1a,** black). Importantly, the bleach from 450-600 nm matches the PDCBT absorption spectrum, complete with vibronic structure, and can only be attributed to the PDCBT polymer, since 4TIC does not absorb in this region. Since we do not excite the polymer (see Appendix A **Figure S2** for control experiments on pristine polymer films) and since the PDCBT bandgap is larger than the 4TIC bandgap, the presence of the PDCBT ground-state bleach presents a clear, unambiguous fingerprint of hole-transfer from 4TIC to PDCBT.

In the NIR wavelengths, we observe two prominent photoinduced absorption (PIA) features at 960 nm and 1100 nm following photoexcitation (**Figure 2.2a)**. At 1 ps, the 960 nm peak dominates the NIR wavelengths, whereas at later times the feature at 1100 nm is the only remaining signature. We assign the 960 nm peak as the absorption of 4TIC exciton generated due to the 810 nm excitation, based on its similarity with the TA spectra of pristine 4TIC solutions (Appendix A **Figure S7**). The 1100 nm peak is likely to be a mixture of various photoexcited species, such as PDCBT/4TIC charge-transfer (CT) states and PDCBT and 4TIC polarons (Appendix A **Figure S3**). Because the exciton and polaron features overlap spectrally, we decomposed the NIR spectrum (900 – 1400 nm) into two Gaussian functions representing each PIA feature (See Appendix A **Section 4** and **Figure S4-5** for details on spectral decomposition). However, the kinetics of these exciton and polaron features did not change appreciably after spectral decomposition (Appendix A **Figure S5**), and we thus use the kinetics data before decomposition in all discussions below for simplicity. The orange trace in **Figure 2.2b** shows a rise with a mono-exponential time constant of ~2 ps. Roughly 80% of the 1100 nm signature population still remains

by 5 ns, indicating the presence of long-lived free carriers. Thus, based on the spectral signature and persistent signal, we assign the 1100 nm peak to absorption of donor and acceptor polarons and/or long-lived charge transfer pairs.

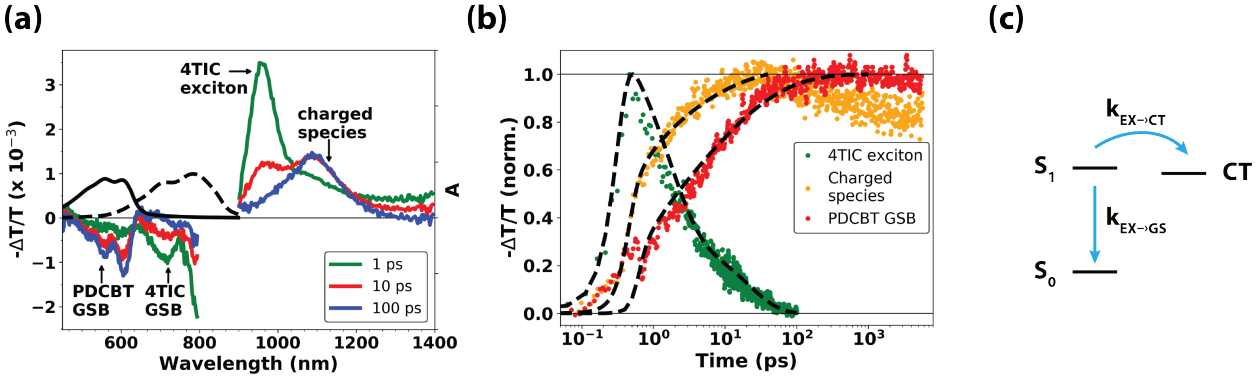

Figure 2.2 (a) Transient absorption spectra of PDCBT/4TIC (1:2 wt/wt) film at selected pump-probe delays of 1, 10 and 100 ps using 810 nm pump at 2.5 μJ/cm2/pulse (green, red and blue) and steady-state absorption spectra of PDCBT (black, solid) and 4TIC (black, dotted). **(b)** Kinetics of 4TIC exciton (at 960 nm), PDCBT GSB (at 600 nm), and the charged species of PDCBT and 4TIC (at 1100 nm). Black traces represent stretched exponential best-fits to the kinetic traces obtained by re-convolving a stretched exponential with the Gaussian-shaped IRF of the laser system (~250 fs). The charge population is only fit up to 100 ps to characterize its rise. **(c)** Scheme for hole-transfer directly from 4TIC excitons. $k_{EX\rightarrow CT}$ and $k_{EX\rightarrow GS}$ are the first-order rate constants of the 4TIC exciton dissociation to form PDCBT/4TIC CT states and the exciton recombination to the ground-state, respectively. S0: ground-state 4TIC, S1: 4TIC singlet exciton.

Figure 2.2b shows that the hole-transfer is remarkably slow yet relatively efficient. We note that only 60% of the polymer GSB (red trace) completes by 10 ps. Yet, the majority of the hole-transfer (~95%), i.e. PDCBT ground-state bleach rise, tracks almost perfectly with the 4TIC exciton decay, with average 1/e lifetimes of 8 ps and 7 ps, respectively. We take the correspondence between the kinetics of the 4TIC exciton decay and the majority of the PDCBT GSB rise to indicate that hole-transfer from the 4TIC excitons occurs efficiently over the first 100 ps, by which time the 4TIC exciton fully decays. Notably, this timescale is much slower compared to many polymer/fullerene and polymer/NFA blends, where charge generation occurs on sub-100-fs timescales.[8,11–13,21] In our blend system, the donor GSB has a slow rise and low signal magnitude within the instrument response, suggesting that ultrafast charge transfer is negligible. Rather, hole-transfer most likely occurs via the 4TIC exciton diffusion and subsequent dissociation into PDCBT/4TIC CT states, a commonly reported charge generation scheme (**Figure 2.2**).[30] Nevertheless, these PDCBT/4TIC blends ultimately exhibit efficient charge transfer and good photovoltaic quantum efficiencies (**Figure 2.1c**) even though the timescale for charge transfer in the PDCBT/4TIC blend is ten-to-hundred times slower than that reported for many typical organic donor/acceptor blends. Based on the charge generation scheme depicted in **Figure 2.2c**, we can quantify the hole-transfer efficiency *within 100 ps* as determined by the competition between first-order rate constants of the 4TIC exciton recombination to ground-state ($k_{EX\rightarrow GS}$) and hole-transfer from the exciton to

donor/acceptor CT state ($k_{EX \rightarrow CT}$, **Eqn. 2.1**). We thus estimate the hole-transfer yield to be around 90%, *within 100 ps*.

$$Hole - transfer\ yield\ =\ k_{EX \rightarrow CT}\ /\ (k_{EX \rightarrow CT}\ +\ k_{EX \rightarrow GS}) \qquad \textbf{Eqn. 2.1}$$

This ~10-100 ps scale charge transfer is already remarkably slow compared to conventional OPV blends. We next focus on the remaining ~5% of the bleach population, which slowly completes from 100 ps to 1 ns. It is unrealistic that this slow phase is due to dissociation of long-lived initial photoexcited excitons because this would imply a hole-transfer yield of ~45% and would be inconsistent with the measured device EQE and the estimated IQE at 810 nm, as explained in detail below. The polymer GSB rise *from 0 ps up to 1 ns* can be fit to a stretched exponential function with average lifetime of 18.3±0.2 ps. Note that the longer average lifetime found here characterizes the long tail observed in the PDCBT GSB rise. Since the 4TIC exciton decays with an average lifetime of 8 ps, based on the hole-transfer scheme in **Figure 2.2c**, the total hole-transfer yield would be only ~45%. This is unreasonable given an estimated IQE of 70% based on the high EQE we observe at 810 nm (**Figure 2.1b,** orange trace). The conundrum here is to reconcile the fast decay of the 4TIC exciton with the slow yet efficient hole-transfer indicated by PDCBT GSB rise. Therefore, we hypothesize that the slow phase of hole-transfer does not originate directly from the spectrally resolved 4TIC excitons to the PDCBT/4TIC CT state; *rather, a separate 4TIC photoexcited species transfers its hole to the PDCBT on the timescale of tens to hundreds of picoseconds*. Specifically, we consider two possibilities for the generation of the second 4TIC photoexcited species. First, *within the instrument response*, some charge-transfer-like species are formed in the pure acceptor region due to intermolecular interactions between aggregated 4TIC molecules. These states could then transfer the hole to the polymer molecules on a delayed timescale, either directly or indirectly. Second, on slower timescales, the 4TIC excitons delocalize among the 4TIC molecules and generate 4TIC charge-transfer-like excitons with a different spectral fingerprint. This slower process would thus appear as an additional non-radiative decay pathway for 4TIC excitons, thereby seemingly competing with CT generation and reducing the hole-transfer yield according to **Eqn. 2.1**, but in actuality leading to charges, just at longer times.

Both of these hypotheses invoke the presence of a spectroscopically buried 4TIC intermediate state (possibly a secondary exciton species of charge-transfer characteristics) and both explain that despite the existence of highly efficient hole-transfer (~90% *within 100 ps*), the polymer GSB rise is two orders of magnitude slower than the exciton decay. Nevertheless, they differ on the time-scale and mechanism of the 4TIC intermediate generation. To examine the above two hypotheses, we performed TA experiments on pristine 4TIC films (Appendix A **Figure S6**). A PIA peak centered at ~1100 nm is immediately generated within the instrument response, even without the presence of the polymer donor, which we propose could be charged species of 4TIC molecules such as polarons or polaron-pairs (see Section 5 in Appendix A for TA studies on pristine 4TIC films, Appendix A **Figure S6-9**).[24] Thus, we hypothesize that 4TIC intermediates in the pure acceptor region of the PDCBT/4TIC blend could be created *within the instrument response*, i.e. in parallel with 4TIC exciton generation, as described by the first hypothesis. However, we cannot completely rule out the possibility that the intermediates are generated sequentially from 4TIC excitons and we therefore include this pathway in our hole-transfer scheme described below in detail.

2.5 Charge-transfer intermediates in pure 4TIC

Generation of secondary photoexcitation species has been reported in various neat homopolymers such as polythiophenes and poly(*p*-phenylene vinylene),[34–39] "push-pull" copolymers such as PBDTTPD, PCDTBT and PTB-based copolymers,[39–43] and various molecular crystals such as sexithiophene and polyacene molecules.[44–48] In these reports, the intermolecular photogenerated species, which exhibit a variety of charge separation and electronic delocalization, are generated (1) via second-order processes such as exciton-exciton and exciton-charge annihilation, at high fluences, (2) directly upon photoexcitation, or (3) via ultrafast branching of the exciton on femtosecond-timescale. In spite of the debate on the origin and electronic nature of the photoexcited species, the molecular packing and aggregation within solid-state polymer and molecular crystals are integral to fast charge photogeneration yield.[39] In the same vein, the enhanced crystallinity of indacenodithiophene-based NFAs,[3,6] including the 4TIC molecule in this study,[24] is very likely to play a role in inducing electronic delocalization of the primary 4TIC excitons to form charge-transfer-like species.

$$\frac{dEX}{dt} = -(k_{EX\rightarrow GS} + k_{EX\rightarrow CT} + k_{EX\rightarrow CTX})[EX] \qquad \textbf{Eqn. 2.2}$$

$$\frac{dCTX}{dt} = -(k_{CTX\rightarrow CT} + k_{CTX\rightarrow GS})[CTX] \qquad \textbf{Eqn. 2.3}$$

$$\frac{dCT}{dt} = k_{EX\rightarrow CT}[EX] + k_{CTX\rightarrow CT}[CTX] - (k_{CT\rightarrow GS} + k_{CT\rightarrow FC})[CT] \qquad \textbf{Eqn. 2.4}$$

$$\frac{dFC}{dt} = k_{CT\rightarrow FC}[CT] \qquad \textbf{Eqn. 2.5}$$

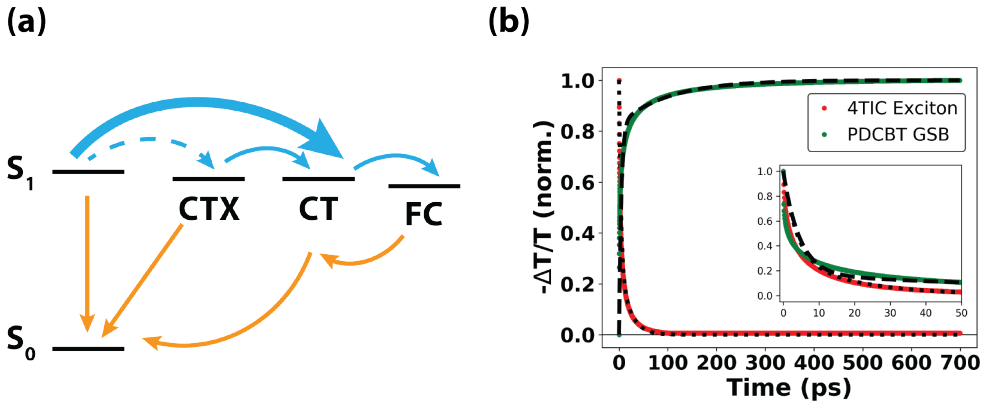

Figure 2.3 (a) Proposed model for charge generation in the PDCBT/4TIC blend upon 4TIC excitation. **(b)** Overlay of the normalized exciton and PDCBT GSB kinetics. Best-fits (black) are obtained by fitting the NFA exciton (··) and polymer GSB (--) kinetics simultaneously to numerical solutions to the rate equations based on the model in (a). Summary of the rate constants are shown in Table 1. Inset shows the normalized early-time (up to 20 ps) kinetics of the exciton and 1 – PDCBT GSB and their best-fits.

To understand the entire hole-transfer process (0-1 ns) in detail, we propose the charge generation scheme shown in **Figure 2.3a**. The key aspect of this model is that two populations of 4TIC photoexcitation, namely the 4TIC excitons and the 4TIC charge-transfer-like excitons (CTXs), can transfer the hole to the polymer PDCBT. Since we are not able to spectrally resolve the 4TIC CTXs

and characterize their dynamics, we consider both ultrafast generation parallel with the 4TIC exciton generation and sequential generation from 4TIC excitons. Our model is described below. Within the instrument response time, two populations of 4TIC photoexcitation are generated. Specifically, spectrally resolved 4TIC excitons (S_1), a fraction (f) of the total initial photoexcitations (N_0), are generated within the instrument response and have three fates: geminate recombination ($\mathbf{k_{EX\rightarrow GS}}$), direct hole-transfer and generation of CT states at donor-acceptor interface ($\mathbf{k_{EX\rightarrow CT}}$), and conversion to the 4TIC CTXs in the pure acceptor region ($\mathbf{k_{EX\rightarrow CTX}}$). The 4TIC CTXs can also be generated within the instrument response, with a yield of $(1-f)\times N_0$. Whether they are generated directly from 4TIC ground-state or from 4TIC excitons is ambiguous. They then hole-transfer to the polymer and form the PDCBT/4TIC CT state, which ultimately either dissociate into hole polarons of donor and electron polarons of acceptor molecules ($\mathbf{k_{CT\rightarrow FC}}$) or recombine geminately ($\mathbf{k_{CT\rightarrow GS}}$). Free carriers in 4TIC and PDCBT eventually recombine non-geminately ($\mathbf{k_{bi}}$) via interfacial CT states. The rate equations for this model are shown in **Eqns.2.2-5**. We omitted the free carrier recombination step in constructing **Eqn. 2.5**. This is reasonable because we focus on the charge generation process up to 1 ns, by which time PDCBT GSB has just saturated, and because the free carrier signal persists out to 5 ns. **Figure 2.3b** shows that the 4TIC exciton and PDCBT GSB kinetics fit well to the numerical solutions to these equations (rate constants shown in **Table 2.1**).

Table 2.1. Summary of rate constants of each step in the proposed hole-transfer model for PDCBT/4TIC blend and the ultrafast splitting ratio of initial photoexcitation into exciton and CT-like excitons.

	Rate constant (1/ps)	**1/e lifetime (ps)**
EX → CT	0.138±0.002	7.2±0.1
EX → GS_A	0.026±0.002	40±6
EX → CTX	0.035±0.001	28±1
CTX → CT	0.0090±0.0001	111±1
CTX → GS_A	0.0011±0.0002	1000±100
CT → FC_A +FC_D	0.076±0.008	13±1
CT → GS_A +GS_B	0.0009±0.0001	1050±30
	Fraction	
f	0.89±0.05	

Average and standard deviation values were obtained by fitting the NFA exciton and polymer GSB kinetic traces to the numerical solution to Equations 2-5 ten times. EX: acceptor exciton, CT: donor/acceptor charge-transfer state, CTX: acceptor charge-transfer-like exciton, $GS_{A(/D)}$: acceptor(/donor) ground-state, $FC_{A(/D)}$: free carrier of acceptor(/donor), f: fraction of the initial photoexcitation that generates 4TIC exciton

We draw attention to three observations. First, the rate constant of donor/acceptor CT formation ($\mathbf{k_{EX\rightarrow CT}}$) is significantly faster than 4TIC exciton geminate recombination to the ground-state ($\mathbf{k_{EX\rightarrow GS}}$). This indicates that hole-transfer from the 4TIC exciton to the PDCBT/4TIC CT state is kinetically favorable and thus efficient, as evidenced by the matching normalized kinetics of (1 - PDCBT GSB) and the 4TIC exciton at early times (**Figure 2.3(b)**, inset). Second, although 4TIC CT excitons convert to PDCBT/4TIC CTs ($\mathbf{k_{CTX\rightarrow CT}}$) faster than their relaxation to the ground-state ($\mathbf{k_{CTX\rightarrow gs}}$), hole-transfer from the 4TIC CT-like excitons (average 1/e time = 111±1 ps, **Table 2.1**) is more than 10 times slower than direct hole-transfer from 4TIC exciton (average 1/e time = 7.2±0.1 ps, **Table 2.1**). Therefore, the presence of the 4TIC CT-like excitons residing on 4TIC allows for slow charge generation on the PDCBT donor polymer. Lastly, based on **Eqn. 2.6**, the total yield of hole-transfer from 4TIC exciton and 4TIC charge-transfer-like exciton is ~94%, consistent with our estimate based on the exciton and polymer GSB kinetics in the first 100 ps (~90%). Overall, this scheme matches well with the observed data, demonstrating that a single hidden or spectroscopically buried state could account for the observed dynamics.

$$Hole-transfer\ yield = f \times \frac{k_{EX\rightarrow CT}+k_{EX\rightarrow CTX}}{k_{EX\rightarrow GS}+k_{EX\rightarrow CT}+k_{EX\rightarrow CTX}} + (1-f) \times \frac{k_{CTX\rightarrow CT}}{k_{CTX\rightarrow CT}+k_{CTX\rightarrow GS}} \qquad \textbf{Eqn. 2.6}$$

2.6 Conclusion

In conclusion, we have studied photoinduced charge generation in a model polymer/NFA system using ultrafast transient absorption spectroscopy. This system is a useful model system in that it permits selective excitation of only the NFA acceptor and has an unambiguous fingerprint of charge transfer in the polymer ground-state bleach. Despite a low driving force for charge transfer, we find the NFA transfers holes to the polymer efficiently, with a yield ~90%, with ~95% of the charges generated during the first 100 ps. This timescale is already much slower than most organic photovoltaic blends reported to date, although there are a limited number of studies reporting delayed charge generation in efficient polymer/NFA blends, where exciton diffusion to the donor/acceptor interface is slow[23] or lowered charge-transfer driving force likely increases exciton dissociation barrier.[10] Surprisingly, the polymer bleach continues to grow slowly over the next nanosecond, even though the excitons on the NFA have all decayed after 100 ps. To interpret this data, we propose that a small fraction of the NFA excitons dissociate into 4TIC CT-like excitons in the acceptor phase. These states can then transfer hole polarons to the polymer at longer times. These results are significant because they provide a detailed look at the kinetics of hole-transfer from a non-fullerene acceptor to a conjugated polymer. They confirm that ~fs scale charge-transfer is not a prerequisite for efficient photocurrent generation, consistent with a small number of prior studies on polymer/fullerene[49,50] and polymer/non-fullerene blends,[12,21] and also appear consistent, if indirectly, with proposal that some non-fullerene acceptors may generate CT states or polaron pairs upon direct photoexcitation.[24]

Appendix A

Experimental method and supplementary information for Chapter 2.

Acknowledgment

This paper is based on work supported primarily by the Office of Naval Research through grant number N00014-17-1-2201. Y.L. also acknowledges support in part by the Clean Energy Institute Graduate Fellowship. We thank Dr. Mark Ziffer for advice on data analysis and members of the Ginger lab for helpful discussion. Part of this work was conducted at the Molecular Analysis Facility, a National Nanotechnology Coordinated Infrastructure site at the University of Washington, which is supported in part by the National Science Foundation (grant ECC-1542101), the University of Washington, the Molecular Engineering & Sciences Institute, the Clean Energy Institute, and the National Institutes of Health.

References

(1) Hou, J.; Inganäs, O.; Friend, R. H.; Gao, F. Organic Solar Cells Based on Non-Fullerene Acceptors. *Nat. Mater.* **2018**, *17* (2), 119–128. https://doi.org/10.1038/nmat5063.

(2) Li, S.; Ye, L.; Zhao, W.; Yan, H.; Yang, B.; Liu, D.; Li, W.; Ade, H.; Hou, J. A Wide Band-Gap Polymer with a Deep HOMO Level Enables 14.2% Efficiency in Polymer Solar Cells. *J. Am. Chem. Soc.* **2018**, jacs.8b02695. https://doi.org/10.1021/jacs.8b02695.

(3) Zhao, W.; Li, S.; Yao, H.; Zhang, S.; Zhang, Y.; Yang, B.; Hou, J. Molecular Optimization Enables over 13% Efficiency in Organic Solar Cells. *J. Am. Chem. Soc.* **2017**, *139* (21), 7148–7151. https://doi.org/10.1021/jacs.7b02677.

(4) Nielsen, C. B.; Holliday, S.; Chen, H.-Y.; Cryer, S. J.; McCulloch, I. Non-Fullerene Electron Acceptors for Use in Organic Solar Cells. *Acc. Chem. Res.* **2015**, *48* (11), 2803–2812. https://doi.org/10.1021/acs.accounts.5b00199.

(5) Yan, C.; Barlow, S.; Wang, Z.; Yan, H.; Jen, A. K. Y.; Marder, S. R.; Zhan, X. Non-Fullerene Acceptors for Organic Solar Cells. *Nat. Rev. Mater.* **2018**, *3*, 18003–18021. https://doi.org/10.1038/natrevmats.2018.3.

(6) Zhang, J.; Tan, H. S.; Guo, X.; Facchetti, A.; Yan, H. Material Insights and Challenges for Non-Fullerene Organic Solar Cells Based on Small Molecular Acceptors. *Nat. Energy* **2018**, *3* (9), 720–731. https://doi.org/10.1038/s41560-018-0181-5.

(7) Ziffer, M. E.; Jo, S. B.; Zhong, H.; Ye, L.; Liu, H.; Lin, F.; Zhang, J.; Li, X.; Ade, H. W.; Jen, A. K.-Y.; Ginger, D. S. Long-Lived, Non-Geminate, Radiative Recombination of Photogenerated Charges in a Polymer:Small-Molecule Acceptor Photovoltaic Blend. *J. Am. Chem. Soc.* **2018**, *140* (31), 9996–10008. https://doi.org/10.1021/jacs.8b05834.

(8) Liu, J.; Chen, S.; Qian, D.; Gautam, B.; Yang, G.; Zhao, J.; Bergqvist, J.; Zhang, F.; Ma, W.; Ade, H.; Inganäs, O.; Gundogdu, K.; Gao, F.; Yan, H. Fast Charge Separation in a Non-Fullerene Organic Solar Cell with a Small Driving Force. *Nat. Energy* **2016**, *1* (7), 16089–16095. https://doi.org/10.1038/nenergy.2016.89.

(9) Baran, D.; Kirchartz, T.; Wheeler, S.; Dimitrov, S.; Abdelsamie, M.; Gorman, J.; Ashraf, R. S.; Holliday, S.; Wadsworth, A.; Gasparini, N.; Kaienburg, P.; Yan, H.; Amassian, A.; Brabec, C. J.; Durrant, J. R.; McCulloch, I. Reduced Voltage Losses Yield 10% Efficient Fullerene Free Organic Solar Cells with >1 V Open Circuit Voltages. *Energy Environ. Sci.* **2016**, *9* (12), 3783–3793. https://doi.org/10.1039/c6ee02598f.

(10) Qian, D.; Zheng, Z.; Yao, H.; Tress, W.; Hopper, T. R.; Chen, S.; Li, S.; Liu, J.; Chen, S.; Zhang, J.; Liu, X. K.; Gao, B.; Ouyang, L.; Jin, Y.; Pozina, G.; Buyanova, I. A.; Chen, W. M.; Inganäs, O.; Coropceanu, V.; Bredas, J. L.; Yan, H.; Hou, J.; Zhang, F.; Bakulin, A. A.; Gao, F. Design Rules for Minimizing Voltage Losses in High-Efficiency Organic Solar Cells. *Nat. Mater.* **2018**, *17* (8), 703–709. https://doi.org/10.1038/s41563-018-0128-z.

(11) Zhong, Y.; Trinh, M. T.; Chen, R.; Purdum, G. E.; Khlyabich, P. P.; Sezen, M.; Oh, S.; Zhu, H.; Fowler, B.; Zhang, B.; Wang, W.; Nam, C. Y.; Sfeir, M. Y.; Black, C. T.; Steigerwald, M. L.; Loo, Y. L.; Ng, F.; Zhu, X. Y.; Nuckolls, C. Molecular Helices as Electron Acceptors in High-Performance Bulk Heterojunction Solar Cells. *Nat. Commun.* **2015**, *6*, 8242–8249. https://doi.org/10.1038/ncomms9242.

(12) Eastham, N. D.; Logsdon, J. L.; Manley, E. F.; Aldrich, T. J.; Leonardi, M. J.; Wang, G.; Powers-Riggs, N. E.; Young, R. M.; Chen, L. X.; Wasielewski, M. R.; Melkonyan, F. S.; Chang, R. P. H.; Marks, T. J. Hole-Transfer Dependence on Blend Morphology and Energy Level Alignment in Polymer: ITIC Photovoltaic Materials. *Adv. Mater.* **2018**, *30* (3), 1704263–1704270. https://doi.org/10.1002/adma.201704263.

(13) Tamai, Y.; Fan, Y.; Kim, V. O.; Ziabrev, K.; Rao, A.; Barlow, S.; Marder, S. R.; Friend, R. H.; Menke, S. M. Ultrafast Long-Range Charge Separation in Nonfullerene Organic Solar Cells. *ACS Nano* **2017**, *11* (12), 12473–12481. https://doi.org/10.1021/acsnano.7b06575.

(14) Bässler, H.; Kohler, A. "hot or Cold": How Do Charge Transfer States at the Donor-Acceptor Interface of an Organic Solar Cell Dissociate? *Phys. Chem. Chem. Phys.* **2015**, *17* (43), 28451–28462. https://doi.org/10.1039/c5cp04110d.

(15) Jailaubekov, A. E.; Willard, A. P.; Tritsch, J. R.; Chan, W. L.; Sai, N.; Gearba, R.; Kaake, L. G.; Williams, K. J.; Leung, K.; Rossky, P. J.; Zhu, X. Y. Hot Charge-Transfer Excitons Set the Time Limit for Charge Separation at Donor/Acceptor Interfaces in Organic Photovoltaics. *Nat. Mater.* **2013**, *12* (1), 66–73. https://doi.org/10.1038/nmat3500.

(16) Grancini, G.; Maiuri, M.; Fazzi, D.; Petrozza, A.; Egelhaaf, H. J.; Brida, D.; Cerullo, G.; Lanzani, G. Hot Exciton Dissociation in Polymer Solar Cells. *Nat. Mater.* **2013**, *12* (1), 29–33. https://doi.org/10.1038/nmat3502.

(17) Bakulin, A. A.; Martyanov, D. S.; Paraschuk, D. Y.; Psehnichnikov, M. S.; van Loosdrecht, P. H. M. Ultrafast Charge Photogeneration Dynamics in Ground-State Charge-Transfer Complexes Based on Conjugated Polymers. *J. Phys. Chem. B* **2008**, *112*, 13730–13737.

(18) Bakulin, A. A.; Hummelen, J. C.; Pshenichnikov, M. S.; Van Loosdrecht, P. H. M. Ultrafast Hole-Transfer Dynamics in Polymer/PCBM Bulk Heterojunctions. *Adv. Funct. Mater.* **2010**, *20* (10), 1653–1660. https://doi.org/10.1002/adfm.200902099.

(19) Etzold, F.; Howard, I. A.; Mauer, R.; Meister, M.; Kim, T. D.; Lee, K. S.; Baek, N. S.; Laquai, F. Ultrafast Exciton Dissociation Followed by Nongeminate Charge Recombination in PCDTBT:PCBM Photovoltaic Blends. *J. Am. Chem. Soc.* **2011**, *133* (24), 9469–9479.

https://doi.org/10.1021/ja201837e.

(20) Jakowetz, A. C.; Böhm, M. L.; Zhang, J.; Sadhanala, A.; Huettner, S.; Bakulin, A. A.; Rao, A.; Friend, R. H. What Controls the Rate of Ultrafast Charge Transfer and Charge Separation Efficiency in Organic Photovoltaic Blends. *J. Am. Chem. Soc.* **2016**, *138* (36), 11672–11679. https://doi.org/10.1021/jacs.6b05131.

(21) Li, Y.; Zhong, L.; Gautam, B.; Bin, H.-J.; Lin, J.-D.; Wu, F.-P.; Zhang, Z.; Jiang, Z.-Q.; Zhang, Z.-G.; Gundogdu, K.; Li, Y.; Liao, L.-S. A Near-Infrared Non-Fullerene Electron Acceptor for High Performance Polymer Solar Cells. *Energy Environ. Sci.* **2017**, *10* (7), 1610–1620. https://doi.org/10.1039/C7EE00844A.

(22) Zheng, Z.; Awartani, O. M.; Gautam, B.; Liu, D.; Qin, Y.; Li, W.; Bataller, A.; Gundogdu, K.; Ade, H.; Hou, J. Efficient Charge Transfer and Fine-Tuned Energy Level Alignment in a THF-Processed Fullerene-Free Organic Solar Cell with 11.3% Efficiency. *Adv. Mater.* **2017**, *29* (5), 3–8. https://doi.org/10.1002/adma.201604241.

(23) Holliday, S.; Ashraf, R. S.; Wadsworth, A.; Baran, D.; Yousaf, S. A.; Nielsen, C. B.; Tan, C. H.; Dimitrov, S. D.; Shang, Z.; Gasparini, N.; Alamoudi, M.; Laquai, F.; Brabec, C. J.; Salleo, A.; Durrant, J. R.; McCulloch, I. High-Efficiency and Air-Stable P3HT-Based Polymer Solar Cells with a New Non-Fullerene Acceptor. *Nat. Commun.* **2016**, *7*, 11585–11595. https://doi.org/10.1038/ncomms11585.

(24) Shi, X.; Zuo, L.; Jo, S. B.; Gao, K.; Lin, F.; Liu, F.; Jen, A. K. Y. Design of a Highly Crystalline Low-Band Gap Fused-Ring Electron Acceptor for High-Efficiency Solar Cells with Low Energy Loss. *Chem. Mater.* **2017**, *29* (19), 8369–8376. https://doi.org/10.1021/acs.chemmater.7b02853.

(25) Zhang, M.; Guo, X.; Ma, W.; Ade, H.; Hou, J. A Polythiophene Derivative with Superior Properties for Practical Application in Polymer Solar Cells. *Adv. Mater.* **2014**, *26* (33), 5880–5885. https://doi.org/10.1002/adma.201401494.

(26) Qin, Y.; Uddin, M. A.; Chen, Y.; Jang, B.; Zhao, K.; Zheng, Z.; Yu, R.; Shin, T. J.; Woo, H. Y.; Hou, J. Highly Efficient Fullerene-Free Polymer Solar Cells Fabricated with Polythiophene Derivative. *Adv. Mater.* **2016**, *28* (42), 9416–9422. https://doi.org/10.1002/adma.201601803.

(27) Ren, G.; Schlenker, C. W.; Ahmed, E.; Subramaniyan, S.; Olthof, S.; Kahn, A.; Ginger, D. S.; Jenekhe, S. A. Photoinduced Hole Transfer Becomes Suppressed with Diminished Driving Force in Polymer-Fullerene Solar Cells While Electron Transfer Remains Active. *Adv. Funct. Mater.* **2013**, *23* (10), 1238–1249. https://doi.org/10.1002/adfm.201201470.

(28) Flagg, L. Q.; Giridharagopal, R.; Guo, J.; Ginger, D. S. Anion-Dependent Doping and Charge Transport in Organic Electrochemical Transistors. **2018**, Article ASAP. https://doi.org/10.1021/acs.chemmater.8b02220.

(29) Zhu, X. Y. How to Draw Energy Level Diagrams in Excitonic Solar Cells. *J. Phys. Chem. Lett.* **2014**, *5* (13), 2283–2288. https://doi.org/10.1021/jz5008438.

(30) Clarke, T. M.; Durrant, J. R. Charge Photogeneration in Organic Solar Cells. *Chem. Rev.* **2010**, *110* (1), 6736–6767. https://doi.org/10.1117/1.JPE.2.021001.

(31) Gregg, B. A. Entropy of Charge Separation in Organic Photovoltaic Cells: The Benefit of

Higher Dimensionality. *J. Phys. Chem. Lett.* **2011**, *2* (24), 3013–3015. https://doi.org/10.1021/jz2012403.

(32) Bin, H.; Gao, L.; Zhang, Z. G.; Yang, Y.; Zhang, Y.; Zhang, C.; Chen, S.; Xue, L.; Yang, C.; Xiao, M.; Li, Y. 11.4% Efficiency Non-Fullerene Polymer Solar Cells with Trialkylsilyl Substituted 2D-Conjugated Polymer as Donor. *Nat. Commun.* **2016**, *7*, 13651–13661. https://doi.org/10.1038/ncomms13651.

(33) Chen, S.; Liu, Y.; Zhang, L.; Chow, P. C. Y.; Wang, Z.; Zhang, G.; Ma, W.; Yan, H. A Wide-Bandgap Donor Polymer for Highly Efficient Non-Fullerene Organic Solar Cells with a Small Voltage Loss. *J. Am. Chem. Soc.* **2017**, *139* (18), 6298–6301. https://doi.org/10.1021/jacs.7b01606.

(34) King, S. M.; Hintschich, S. I.; Dai, D.; Rothe, C.; Monkman, A. P. Spiroconjugation-Enhanced Intramolecular Charge-Transfer State Formation in a Polyspirobifluorene Homopolymer. *J. Phys. Chem. C* **2007**, *111* (50), 18759–18764. https://doi.org/10.1021/jp0755138.

(35) Westerling, M.; Aarnio, H.; Österbacka, R.; Stubb, H.; King, S. M.; Monkman, A. P.; Andersson, M. R.; Jespersen, K.; Kesti, T.; Yartsev, A.; Sundström, V. Photoexcitation Dynamics in an Alternating Polyfluorene Copolymer. *Phys. Rev. B - Condens. Matter Mater. Phys.* **2007**, *75* (22), 224306–224314. https://doi.org/10.1103/PhysRevB.75.224306.

(36) Yan, M.; Rothberg, L. J.; Papadimitrakopoulos, F.; Galvin, M. E.; Miller, T. M. Spatially Indirect Excitons as Primary Photoexcitations in Conjugated Polymers. *Phys. Rev. Lett.* **1994**, *72* (7), 1104–1107. https://doi.org/10.1103/PhysRevLett.72.1104.

(37) Paquin, F.; Latini, G.; Sakowicz, M.; Karsenti, P. L.; Wang, L.; Beljonne, D.; Stingelin, N.; Silva, C. Charge Separation in Semicrystalline Polymeric Semiconductors by Photoexcitation: Is the Mechanism Intrinsic or Extrinsic? *Phys. Rev. Lett.* **2011**, *106* (19), 197401–197404. https://doi.org/10.1103/PhysRevLett.106.197401.

(38) Yu, G.; Phillips, S. D.; Tomozawa, H.; Heeger, A. J. Subnanosecond Transient Photoconductivity in Poly(3-Hexylthiophene). *Phys. Rev. B* **1990**, *42* (5), 3004–3010. https://doi.org/10.1103/PhysRevB.42.3004.

(39) Reid, O. G.; Pensack, R. D.; Song, Y.; Scholes, G. D.; Rumbles, G. Charge Photogeneration in Neat Conjugated Polymers. *Chem. Mater.* **2014**, *26* (1), 561–575. https://doi.org/10.1021/cm4027144.

(40) Rolczynski, B. S.; Szarko, J. M.; Son, H. J.; Liang, Y.; Yu, L.; Chen, L. X. Ultrafast Intramolecular Exciton Splitting Dynamics in Isolated Low-Band-Gap Polymers and Their Implications in Photovoltaic Materials Design. *J. Am. Chem. Soc.* **2012**, *134* (9), 4142–4152. https://doi.org/10.1021/ja209003y.

(41) Szarko, J. M.; Rolczynski, B. S.; Lou, S. J.; Xu, T.; Strzalka, J.; Marks, T. J.; Yu, L.; Chen, L. X. Photovoltaic Function and Exciton/Charge Transfer Dynamics in a Highly Efficient Semiconducting Copolymer. *Adv. Funct. Mater.* **2014**, *24* (1), 10–26. https://doi.org/10.1002/adfm.201301820.

(42) Hwang, I.; Beaupré, S.; Leclerc, M.; Scholes, G. D. Ultrafast Relaxation of Charge-Transfer Excitons in Low-Bandgap Conjugated Copolymers. *Chem. Sci.* **2012**, *3* (7), 2270–2277. https://doi.org/10.1039/c2sc20078c.

(43) Tong, M.; Coates, N. E.; Moses, D.; Heeger, A. J.; Beaupré, S.; Leclerc, M. Charge Carrier Photogeneration and Decay Dynamics in the Poly(2,7-Carbazole) Copolymer PCDTBT and in Bulk Heterojunction Composites with PC70 BM. *Phys. Rev. B - Condens. Matter Mater. Phys.* **2010**, *81* (12), 125210–125215. https://doi.org/10.1103/PhysRevB.81.125210.

(44) Glowe, J. F.; Perrin, M.; Beljonne, D.; Hayes, S. C.; Gardebien, F.; Silva, C. Charge-Transfer Excitons in Strongly Coupled Organic Semiconductors. *Phys. Rev. B - Condens. Matter Mater. Phys.* **2010**, *81* (4), 041201–041214. https://doi.org/10.1103/PhysRevB.81.041201.

(45) Beljonne, D.; Yamagata, H.; Brédas, J. L.; Spano, F. C.; Olivier, Y. Charge-Transfer Excitations Steer the Davydov Splitting and Mediate Singlet Exciton Fission in Pentacene. *Phys. Rev. Lett.* **2013**, *110* (22), 226402–226406. https://doi.org/10.1103/PhysRevLett.110.226402.

(46) Weiser, G.; Sebastian, L.; Physikalische, F. Charge Transfer Transitions in Solid Tetracene and Pentacene Studied by Electroabsorption. *Chem. Phys.* **1981**, *61*, 125–135.

(47) Muntwiler, M.; Yang, Q.; Tisdale, W. A.; Zhu, X. Y. Coulomb Barrier for Charge Separation at an Organic Semiconductor Interface. *Phys. Rev. Lett.* **2008**, *101* (19), 196403–196406. https://doi.org/10.1103/PhysRevLett.101.196403.

(48) Pope, M.; Swenberg, C. E. *Electronic Processes in Organic Crystals and Polymers*, Second Edi.; Oxford University Press: New York, 1999.

(49) Ohkita, H.; Cook, S.; Astuti, Y.; Duffy, W.; Tierney, S.; Zhang, W.; Heeney, M.; McCulloch, I.; Nelson, J.; Bradley, D. D. C.; Durrant, J. R. Charge Carrier Formation in Polythiophene/Fullerene Blend Films Studied by Transient Absorption Spectroscopy. *J. Am. Chem. Soc.* **2008**, *130* (10), 3030–3042. https://doi.org/10.1021/ja076568q.

(50) Kawashima, K.; Tamai, Y.; Ohkita, H.; Osaka, I.; Takimiya, K. High-Efficiency Polymer Solar Cells with Small Photon Energy Loss. *Nat. Commun.* **2015**, *6*, 10085–10090. https://doi.org/10.1038/ncomms10085.

Chapter 3. Lower limits for non-radiative recombination losses of charge-transfer states: the role of LE-CT mixing

This chapter is from the submitted manuscript: Liu, Y.; Zheng, Z.; Coropceanu, V., Bredas, J-L., Ginger, D. Lower Limits for Non-Radiative Recombination Losses in Donor/Acceptor Organic Complexes.

3.1 Overview

the factors controlling radiative and non-radiative transition rates for charge transfer states in organic systems is important for applications ranging from organic photovoltaics (OPV) to lasers and LEDs. We explore the role of charge-transfer (CT) energetics, lifetimes, and photovoltaic properties in the limit of very slow non-radiative rates by using a model donor/acceptor system with photoluminescence dominated by thermally activated delayed fluorescence (TADF). This blend exhibits an extremely high photoluminescence quantum efficiency (PLQY = ~22%) and comparatively long PL lifetime, while simultaneously yielding appreciable amounts of free charge generation (photocurrent external quantum efficiency EQE of 24%). In solar cells, this blend exhibits non-radiative voltage losses of only ~0.1 V, among the lowest reported for an organic system. Notably, we find the non-radiative decay rate, $k_{nr,}$ on the order of $\mathbf{10^5\ s^{-1}}$, approximately 4-5 orders of magnitude slower than typical OPV blends, thereby confirming that high radiative efficiency and low non-radiative voltage losses are achievable by reducing k_{nr}. Furthermore, despite the high radiative efficiency and already comparatively slow k_{nr}, we find that k_{nr} is nevertheless much faster than predicted by Marcus-Jortner-Levich two-state theory and we conclude that CT-local exciton hybridization is present. Our findings highlight that it is crucial to evaluate how radiative and non-radiative rates of the local exciton individually influence the PLQY of charge-transfer states, rather than solely focusing on the PLQY of the LE. This conclusion will guide material selection in achieving low non-radiative voltage loss in organic solar cells and high luminescence efficiency in organic LEDs.

3.2 Introduction

Donor-acceptor (D:A) blends are widely used in efficient organic light emitting diodes (OLEDs) and organic photovoltaics (OPVs). Detailed balance arguments indicate that these two applications are two sides of the same coin,[1,2] which, as OPVs have climbed to higher efficiencies, has led to the realization in the organic solar cell community that OPVs should also be bright (radiatively efficient) if they are to approach theoretical efficiency limits.[3] Despite recent efforts to improve the luminescence efficiency of charge-transfer states, OPVs still largely suffer significant energy losses from non-radiative recombination[3–5] compared to inorganic systems like perovskites or GaAs.[6–9] Typically, polymer/fullerene-based OPVs have non-radiative voltage losses (ΔV_{OC}^{nr}) in the range of ~0.3-0.4 V,[10] with the most efficient polymer/non-fullerene systems reaching ΔV_{OC}^{nr} of 0.2-0.3 V.[11–17] While these values approach those for commercial silicon (~0.18 V),[18] they still compare poorly with ΔV_{OC}^{nr} values of 0.027 V for GaAs[8] and 0.034 V for emerging perovskite materials.[9] The so-called "energy gap law"[19] for non-radiative geminate recombination rates has been invoked to set the boundaries for the radiative efficiency of organic D:A blends. Furthermore, Vandewal and co-workers have suggested that organic blends should have intrinsically high non-

radiative recombination rates due to the coupling of the electron transfer process with high-frequency intramolecular vibrations.[10] Multiple groups have highlighted the importance of controlling reorganization energy and disorder to achieve high radiative efficiency.[20–22] Despite these efforts, the radiative and non-radiative rates of organic (macro)molecules in OLEDs and OPVs are still not fully understood at the microscopic level. For example, remarkably emissive CT states have been reported with radiative efficiencies exceeding those predicted by the "energy gap law".[12,13,23,24] Along the same line, after it was demonstrated in 2012 that D:A exciplexes[25] can be used to build efficient OLEDs, there have been major advances in exciplex-based OLEDs with external quantum efficiencies (EQEs) of 20.0% for blue and 24.0% for green emitting devices.[26] Since many exciplex emitters rely on the thermally activated delayed fluorescence (TADF) mechanism, a significant amount of recent work was mainly focused on understanding intersystem crossing (ISC) and reverse ISC transitions. In contrast, understanding the transition rates of the exciplex or CT state itself has received less attention.

To gain insight into the radiative and non-radiative rates of the CT state as well as the impact of these rates on the optoelectronic performance, we use a model TADF-emissive blend composed of 4,4′,4″-tris[3-methylphenyl(phenyl)amino]triphenylamine (m-MTDATA) as the donor and tris-[3-(3-pyridyl)mesityl]borane (3TPYMB) as the acceptor. TADF blends, compared to typical donor/acceptor OPV blends, are luminescent systems with long PL lifetime due to thermally activated reverse intersystem crossing from the lowest triplet state to the lowest singlet excited state.[27–30] The m-MTDATA/3TPYMB blend is intriguing because it exhibits both a high photoluminescence quantum yield (PLQY ~22%), and an appreciable photovoltaic external quantum efficiency (EQE_{PV} max ~24%) for converting incident photons into photocurrent.[31–34] We find that the non-radiative decay rate is significantly faster than that predicted by the Marcus-Levich-Jortner (MLJ) two-state model within the realm of plausible molecular parameters. Combining our experimental and theoretical results, we conclude that hybridization of the CT states with the local exciton (LE) states speeds up the non-radiative decay and harms the photoluminescence quantum yield, leading to additional non-radiative recombination loss. Our results highlight the importance of controlling CT energetics, namely CT-LE hybridization, to achieve small non-radiative recombination loss in OPVs and high radiative efficiency in OLEDs.

3.3 An emissive and charge-generating charge-transfer state- based system: m-MTDATA/3TPYMB blend

Photoluminescence properties

Figure 3.1a shows the molecular structures and reported state energies of both m-MTDATA and 3TPYMB.[35] We deposited (1:1) blend films of m-MTDATA:3TPYMB by thermal co-evaporation of the donor and acceptor materials. Figure 3.1b shows the PL of the neat donor and acceptor materials, as well as the blend. Compared to neat donor and acceptor films, the m-MTDATA:3TPYMB blend shows a significantly red-shifted PL spectrum, consistent with charge-transfer state emission, indicating that charge and energy transfer from the local exciton to the CT state are highly efficient, in good agreement with previous reports.[31,32]

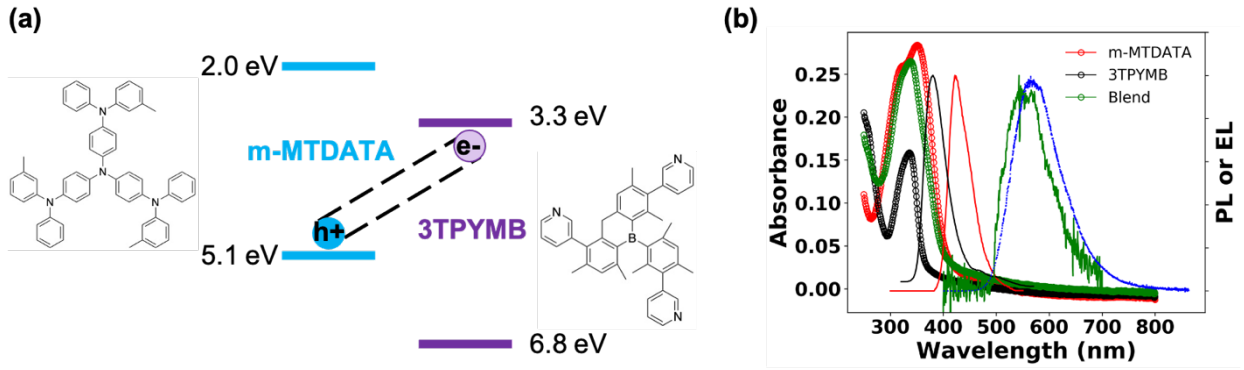

Figure 3.1 (a) Energy levels and molecular structures of m-MTDATA and 3TPYMB. **(b)** Absorption (-o-) and PL spectra (-) of neat donor (red), acceptor (black) and blend films/devices (green) overlaid with EL spectrum (blue) of the blend device. The PL spectrum of the blend was measured from the solar cell device stack.

Figure 3.2 shows the time-resolved photoluminescence (PL) from the blend measured at room temperature. We observe a clear bi-phasic PL decay with both prompt and delayed emission, characteristic of TADF materials. **Figure 3.2** also shows fits of a bi-exponential decay to the observed PL kinetics, which yields lifetimes of 4.7 µs and 43 µs for the prompt and delayed decays, respectively, both consistent with previous reports on this system.[32,34,35] On glass substrates, our blends exhibit a PLQY from the CT state of 22%. This PLQY value is 2-3 orders of magnitude higher than typical CT emission in OPVs.[12,36] Based on our measured PLQYs and lifetimes, we determine the radiative (k_r), intersystem crossing (k_{ISC}), and non-radiative (k_{nr}) rate constants of the singlet CT state (^{1}CT) to be $k_r = 2.75 \times 10^4\ s^{-1}$, $k_{ISC} = 8.9 \times 10^4\ s^{-1}$, and $k_{nr} = 9.8 \times 10^4\ s^{-1}$, respectively (see SI Section 1 for details on the rate calculation). Compared to previously reported k_r and k_{nr} values for CT states in D/A OPV blends, the m-MTDATA/3TPYMB blend system exhibits what appears to be a remarkably slow non-radiative rate—roughly 5 orders of magnitude slower than commonly reported k_{nr} values for CT states (Appendix B Table S1).

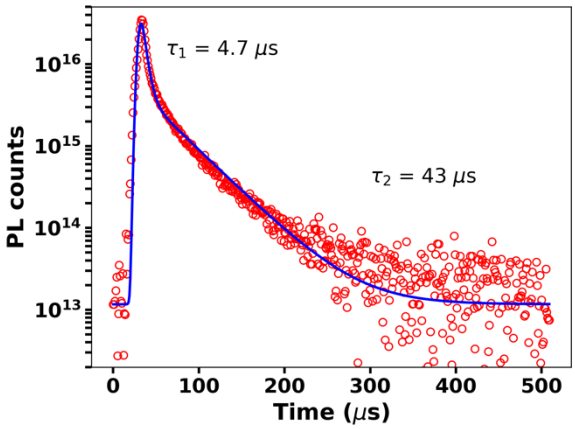

Figure 3.2 PL decay shows prompt and delayed emission with time constants of 4.7 µs and 43 µs. A two-exponential function convolved with experimentally measured IRF is fit to the data, shown in blue.

Photovoltaic properties

Next, we explore the photovoltaic properties of the m-MTDATA:3TPYMB blend. We chose the following device structure: glass/ITO/PEDOT-PSS/MeO-TPD/m-MTDATA/m-TDATA:3TPYMB/3TPYMB/Bphen/LiF/Al, in order to avoid formation of any potentially interfering exciplexes at the interfaces of the active layer and transport layers. The device demonstrates a maximum incident photon to charge collection efficiency (EQE_{PV}) of 24% (**Figure 3.3a**). We measured the refractive indices via ellipsometry and modelled the absorption of the m-MTDATA:3TPYMB layer in the device (see Appendix B Figure S1) using a transfer matrix algorithm to calculate the photovoltaic internal quantum efficiency (IQE_{PV}).[37] We find that IQE_{PV} is over 40% over the region corresponding to the majority of the donor and acceptor absorption spectra. **Figure 3.3c** shows the electroluminescence quantum yield (EQE_{EL}) measured as a function of injected current density. In the best performing PV cell, we measure EQE_{EL} to be 1.67% at injection current equivalent to short-circuit current at 1-Sun illumination condition (average EQE_{EL}=1.82±0.02%, number of devices, N=6). We thus obtain the corresponding ΔV_{OC}^{nr} according to Eqn. 3.2 below to be only ~100meV, which places this system among the most emissive charge-generating organic photodiode structures, comparable to the best OLED-based OPVs reported so far (**Figure 3.3d**).[10,12,13,15,16,24,38–43] **Figure 3.3b** shows that under AM1.5G illumination conditions, the best performing PV cell yields a V_{OC} of 2.12 V (2.12±0.03 V, N=6); however, despite a photocurrent EQE_{PV} of ~24%, J_{SC} only reaches ~0.1 mA/cm^2 (0.09±0.02 mA/cm^2, N=6) due to the wide bandgap and consequent poor overlap with the solar spectrum.

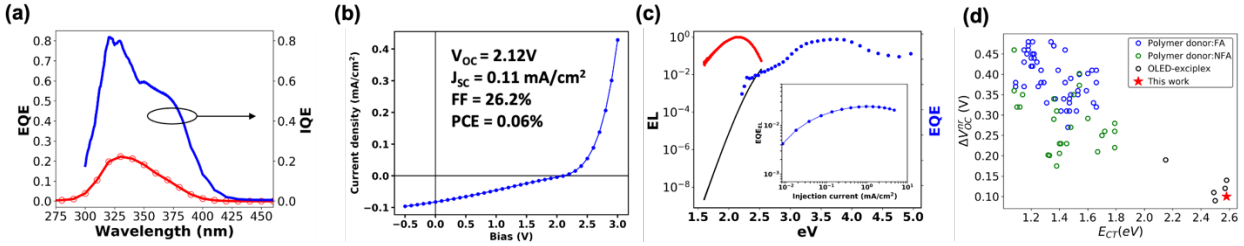

Figure 3.3 (a) EQE_{PV} and IQE_{PV} spectra, overlaid with PLE spectrum (dashed red line). **(b)** J-V curve measured under simulated AM1.5G illumination. **(c)** EL (red), EQE_{PV} (blue), and recreated EQE_{PV} (black) spectrum based on Rau's reciprocity theorem. The EL spectrum is divided by the blackbody radiation spectrum and multiplied by a scaling factor to match the low-energy EQE tail. (inset) Electroluminescence external quantum efficiency (EQE_{EL}) at 1-Sun illumination relevant injection current. **(d)** Survey of ΔV_{nr}^{OC} and E_{CT} of previously reported CT-based donor/acceptor blends (blue and green), a previously reported OLED exciplex-based blend (black) and our blend.

The experimental V_{OC} of 2.12 V is 0.73 V lower than the Shockley-Queisser V_{OC} limit (V_{OC}^{SQ}) of 2.85 V for the bandgap of 3.239 eV. Thus, we next consider the factors governing the overall voltage loss in our CT-based TADF-emissive solar cell. Following the well-established framework based on detailed balance,[44,45] we separate the V_{OC} loss into two sources: (1) charge generation loss (ΔV_{OC}^{SC}), which is due to non-ideal EQE_{PV} and (2) charge recombination loss, both radiative and non-radiative, where ΔV_{OC}^{nr} is related to energy loss due to non-radiative recombination (Eqn. 3.1):

$$V_{OC} = V_{OC}^{SQ} + \Delta V_{OC}^{SC} + \Delta V_{OC}^{r} + \Delta V_{OC}^{nr} \qquad \text{Eqn. 3.1}$$

$$q\Delta V_{OC}^{nr} = -kTln(EQE_{EL}) \qquad \text{Eqn. 3.2}$$

Table 3.1 Results of the open-circuit voltage loss analysis.

$E_{gap}(eV)$	$V_{OC}^{SQ}(V)$	$\Delta V_{OC}^{SC}(V)$	$\Delta V_{OC}^{r}(V)$	$\Delta V_{OC}^{nr}(V)$	$V_{OC}^{calc}(V)$	$V_{OC}^{meas}(V)$
3.239	2.85	-0.0484	-0.6	-0.104	2.098	2.11

The radiative voltage loss (ΔV_{OC}^{r}) is due to radiative recombination that is not accounted for in the Shockley-Queisser limit due to additional absorption/emission states below the bandgap (which is a step function in the ideal SQ case). By analyzing the sub-gap EQE and EL spectra within Rau's reciprocity framework (Table 3.1; see Appendix B Section 2 for details), we determine ΔV_{OC}^{r} to be 0.600 V. This value is on the higher end compared to efficient BHJ OPVs.[12–15,46] We attribute this large ΔV_{OC}^{r} to the large offset between E_{CT} and the bandgap (Figure S2), leading to significant below-gap absorption. Taken together, our voltage loss analysis (1) demonstrates a small non-radiative recombination loss, among the lowest reported to date in charge-generating organic solar cells and (2) highlights the challenge of simultaneously reducing radiative and non-radiative voltage losses in CT-based solar cells.[47]

Benchmarking transition rates of the CT state

At this point, we return to analyze the k_{nr} values in more detail. It is instructive to compare the emissive properties of the m-MTDATA:3TPYMB *blend* with those of the m-MTDATA and 3TPYMB components. We measured the radiative rate (k_r^{LE}), non-radiative rate (k_{nr}^{LE}) and PLQY, respectively, to be 5.14x10^7 s^{-1}, 4.2x10^8 s^{-1} and 11% in m-MTDATA, and 6.44x10^7 s^{-1}, 8.97x10^8 s^{-1} and 6% in 3TPYMB (see Appendix B Section 3 for details). Interestingly, the PLQY of the blend (22%) is over twice as large as the respective values for the D and A components. Another intriguing finding is that the non-radiative rate of the CT state is about four orders of magnitude slower than the non-radiative rates of the related local-exciton (LE) states despite the fact that the CT state is located about 0.7 eV and 1.0 eV below the emissive states of m-MTDATA and 3TPYMB, respectively.

Therefore, it is of great interest (1) to examine in detail the radiative and non-radiative transition rates of the CT state and (2) to correlate the luminescence properties with the photovoltaic properties in order to understand whether a small non-radiative recombination loss is expected given the large bandgap in our system.

3.4 Transition rates of CT states in the MLJ framework

The radiative and non-radiative transitions involving CT states are commonly investigated within the two-state MLJ formalism (see Appendix Section 4 for details).[4,21,48–50] Briefly, in the MLJ framework, both radiative and non-radiative transitions are described as electron-transfer events between the CT and ground (G) states. Thus, this model assumes that the electronic coupling ($V_{CT\text{-}G}$) between the CT and G states is much larger than that between the CT state and donor and/or acceptor LE state ($V_{CT\text{-}LE}$). The non-radiative and radiative transition rates can then be written as

a function of the adiabatic CT energy (E_{CT}), electronic coupling ($V_{CT\text{-}G}$), classical (λ_c) and quantum mechanical (λ_{qm}) components of the total reorganization energy ($\lambda_t = \lambda_c + \lambda_{qm}$), frequency of an effective quantum vibrational mode (ω_{qm}), and transition dipole moment (d_{CT}). The MLJ model has previously been used extensively to rationalize the experimental non-radiative voltage losses in polymer/NFA,[12,13,15,16,24,41–43] polymer/fullerene,[10,13,24,38–40] and OLED-based OPV materials[40] (see Appendix B Section 4 for details and further discussion on the two-state MLJ model).

Molecular dynamics calculation

In order to estimate the non-radiative decay rate constant, the microscopic parameters mentioned above have to be determined first. On the theoretical side, we started by carrying out molecular dynamics (MD) simulations to determine the likely morphology of the m-MTDATA:3TPYMB (**Figure 3.4a**) blend. We then computed the energy distributions of the lowest excited CT and LE states as well as of the $V_{CT\text{-}G}$ and $V_{CT\text{-}LE}$ electronic couplings by performing time-dependent DFT (TDDFT) calculations at the SRSH-ωPBE-D3/6-31G(d) level of theory for 1,500 D-A complexes extracted from the MD-derived film morphology. In addition, we performed geometry optimizations of the neutral and charged configurations of the m-MTDATA and 3TPYMB molecules to estimate the intramolecular contributions to the reorganization energy λ_t. **Figure 3.4b** shows that the singlet (^{1}CT) and triplet (^{3}CT) CT states have similar energy distributions, with the singlet-triplet energy splitting not exceeding 2 meV. The energy distribution of the lowest triplet state in the m-MTDATA molecule overlaps with the ^{1}CT and ^{3}CT distributions, which suggests that the spin-orbit interactions between the CT singlet and triplet states are strongly influenced by this local triplet state.

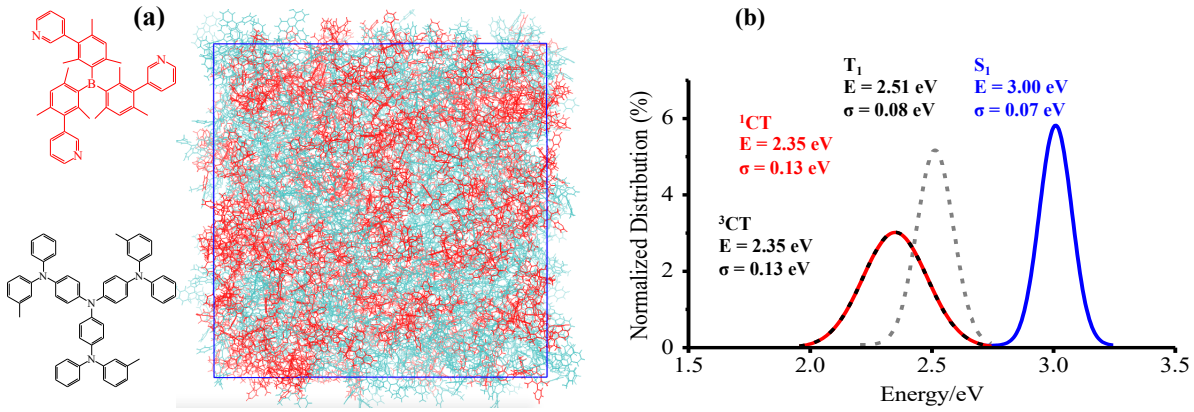

Figure 3.4 (a) Illustration of the morphologies of the m-MTDATA:3TPYMB blend; **(b)** Distributions of the energies of the lowest CT and LE singlet and triplet states.

Figure 3.5 shows the results derived for the electronic couplings and reorganization energies. **Figure 3.5a-b** shows that the electronic couplings between the singlet CT state and the first LE singlet excited state (V_{CT-LE}) and those between the CT state and the ground state (V_{CT-G}) have exponential-type energy distributions with average values of 3 meV for V_{CT-LE} and 6 meV for

V_{CT-G}. We estimate the overall reorganization energy to be 0.41 eV, with 0.18 eV coming from the D component and 0.23 eV from the A component. As seen from **Figure 3.5c-d**, the partition of the reorganization energy over the normal modes indicates that a significant contribution to the reorganization energy is coming from low-energy (classical) vibrational modes.

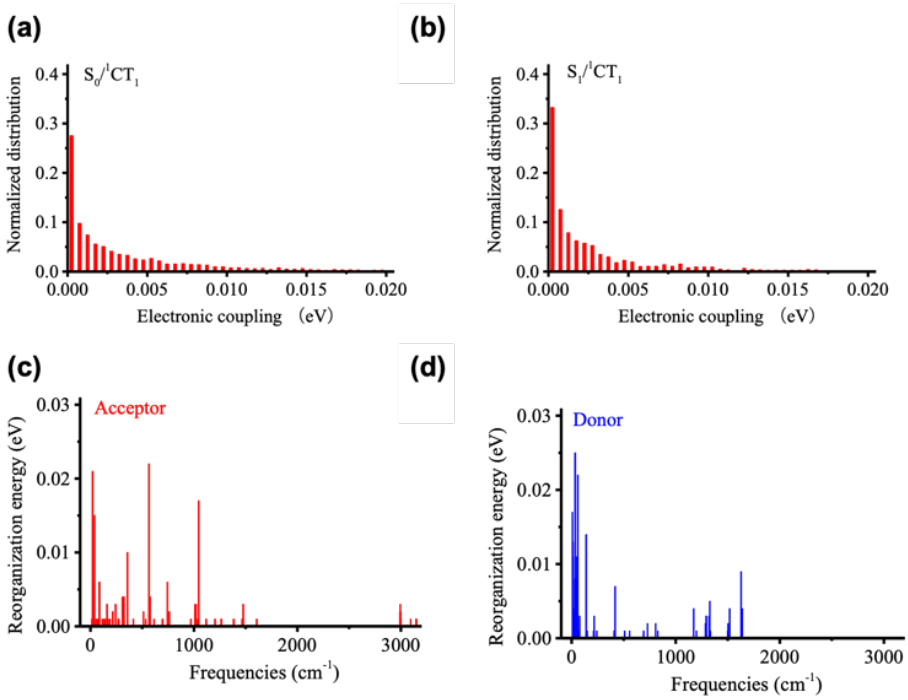

Figure 3.5 Distribution of (a) V_{CT-G} and (b) V_{CT-LE} electronic couplings, and vibrational normal mode contributions to the (c) acceptor and (d) donor reorganization energy components of λ_t.

Fitting of experimental photoluminescence data

On the experimental side, information on the microscopic parameters can be obtained from the intensity and profile of the absorption or emission CT band.[51,52,53] Here, we estimated E_{CT}, λ_t, λ_{qm} and ω_{qm} by fitting the profile of the blend PL band measured at 80 K to an extended version of the MLJ model that accounts for static disorder (see Eqn. S11). As seen from **Figure 3.6a** (red trace), an excellent simulation of the CT band can be obtained by using: E_{CT} = 2.65 eV, λ_t = 0.4 eV, λ_{qm} = 0.25 eV, ω_{qm} = 0.1 eV, and σ_s =70 meV for the standard deviation of static disorder (70 meV is in the range of reported values for other D:A blends[54]). For high-energy CT systems, such as the TADF-based system in this study and OLED-material-based systems, the non-radiative transition rates can vary as a function of the reorganization energy (in particular of λ_{qm}) by orders of magnitude (see Figure S3). Since the MLJ fitting procedure depends on the multiple parameters listed above and thus is not unique, we checked what could be the upper limit of the reorganization energy. We found that MLJ calculations employing λ_{qm} of 0.39 eV or larger yield broader PL bands than that observed experimentally, even for negligible values of λ_c (**Error! Reference source not found.**a). Thus, we conclude that, in the present system, λ_{qm} must be smaller than 0.39 eV. This conclusion is in good agreement with the results of the quantum-mechanical calculations described above, which yield a value of 0.41 eV for λ_t.

We next use Mulliken-Hush formalism to estimate the electronic coupling $V_{CT\text{-}G}$:[52]

$$V_{CT-G} = \frac{d_{CT-G}}{\Delta d_{CT-G}} E_{CT}^{v} \qquad \text{Eqn. 3.3}$$

where Δd_{CT-G} is the difference between the CT and G state dipole moments. We obtained the transition dipole moment (d_{CT-G}= 0.05 D) and transition (vertical) energy (E_{CT}^{v}=2.16 eV) from the PL measurements (see Appendix B Section 5 for details). Δd_{CT-G} can also be estimated experimentally via electroabsorption spectroscopy.[12,55] For the sake of simplicity, we took Δd_{CT-G}= 23 D, as calculated at the DFT level. Based on Eqn. 3, we estimate a value of 5 meV for V_{CT-G}, which is in very good agreement with the average value of 6 meV obtained from the TDDFT calculations, as described above (see Appendix B Section 6 for details on the theoretical methodology).

Based on these parameters, we calculated k_r and k_{nr} within the MLJ framework (see SI Section 4 for details). **Figure 3.6b** and **c** highlight that a variation of λ_t (and λ_{qm}) in the range of 0.2-0.6 eV results in a variation of the non-radiative transition rates by many orders of magnitude, whereas the radiative transition rates exhibit a less dramatic response. Intriguingly, if we employ the microscopic parameters reported above: V_{CT-G} = 0.01 eV, E_{CT} = 2.65 eV, λ_t = 0.4 eV, λ_{qm} = 0.25 eV, ω_{qm} = 0.1 eV and σ_s=70 meV, we find that the MLJ theory estimate for k_{nr} is about 8 orders of magnitude smaller than the experimental value. To reproduce the experimental k_{nr} value using the MLJ model would require λ_t values exceeding 0.6 eV and coming nearly exclusively from quantum vibrational modes (**Figure 3.6b**). However, if such high λ_t were actually the case, the MLJ model predicts that the PL emission spectrum would be significantly broader and shifted from the experimental absorption spectrum. Since the actual situation is inconsistent with this picture, we must conclude that the MLJ framework is unable to provide a self-consistent description of the transition rates and PL spectrum of the m-MTDATA:3TPYMB blend. More importantly, this crosschecking exercise again highlights the importance of using the appropriate microscopic parameters, especially reorganization energy, when predicting CT kinetics and thus non-radiative voltage loss: While it may be possible to fit spectra and rates, doing so with unphysical molecular parameters may not provide the sought-after physical insight.

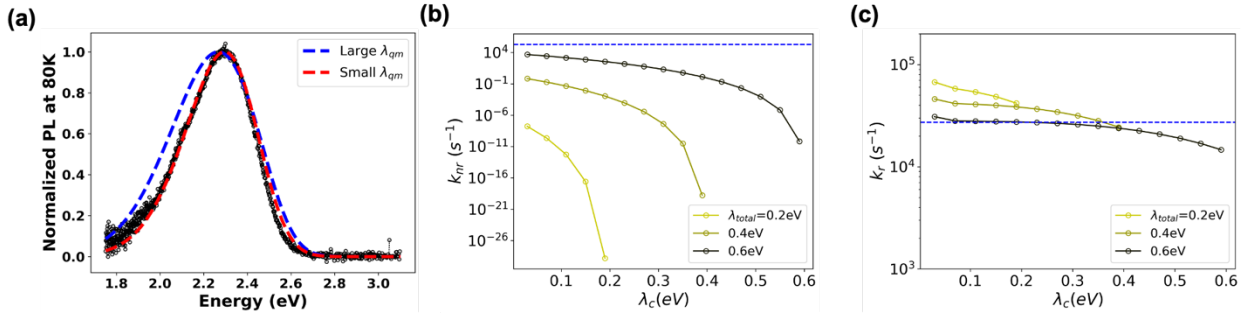

Figure 3.6 (a) Comparison between the experimental PL spectrum (black) and best-fits from simulation (red and blue). λ_t is fixed at 0.4 eV, σ_s=70 meV, ω_{qm} = 0.1 eV. Blue trace: λ_{qm}=0.39 eV, E_{CT}=2.58 eV; red: λ_{qm}=0.2 eV, E_{CT}=2.65 eV. (b) k_{nr} and (c) k_r calculated as a function of total reorganization energy, using the following microscopic parameters: σ_s=70 meV, ω_{qm} = 0.1 eV, and E_{CT}=2.58 eV. For each curve, the total reorganization energy shown in the legend is

fixed at a certain value (0.2eV, 0.4eV, 0.6eV) and the portion accounted to λ_c (up to 100% λ_t with the balance being λ_{qm}) is varied as indicated on the x-axis. The blue dotted line is the experimental value.

3.5 Three-state model: Charge-transfer, local exciton and ground state

From this discussion, it is not surprising that high-energy CT systems could exhibit very small non-radiative decay rates. For the m-MTDATA:3TPYMB blend, the question in fact is why the experimental non-radiative rate is dramatically *faster* than that expected in the framework of the MLJ model, even though it appears much slower than most of the reported values for (lower energy) organic CT states. Finding the explanation requires going beyond the two-state model. Since the local exciton states formed on m-MTDATA and 3TPYMB efficiently dissociate into CT states, it means that that the LE and CT states are also electronically coupled. According to our DFT calculations, the coupling between the CT state and lowest LE state (V_{CT-LE}) is about 3 meV. We have previously shown that a three-state model, which accounts for the couplings of the CT state with both the LE and ground states, is needed in order to rationalize the radiative and non-radiative transitions from inter-molecular and intra-molecular CT states.[56] In fact, as we have recently found in the case of D-A neutral radical systems, when the LE state exhibits large non-radiative rates, even a modest hybridization between the LE and CT states can result in a significant increase in the CT k_{nr} value.[57] The experimental optical-gap (adiabatic) energies (E_{LE}) are 3.09 eV in m-MTDATA and 3.5 eV in 3TPYMB (see Appendix Section 3). The k_{nr} value for the CT state when considering CT-LE hybridization can be roughly estimated as:[57,58]

$$k_{nr} = (1 - f_{CT-LE})k_{nr}^{MLJ} + f_{CT-LE}k_{nr}^{LE} \qquad \text{Eqn. 3.4}$$

$$f_{CT-LE} = \left[\frac{V_{CT-LE}}{\Delta E_{LE-CT}}\right]^2 \Big/ \left(1 + \left[\frac{V_{CT-LE}}{\Delta E_{LE-CT}}\right]^2\right) \qquad \text{Eqn. 3.5}$$

where k_{nr} is the non-radiative rate for the CT state in the three-state model, k_{nr}^{MLJ} is the non-radiative rate for the CT state according to MLJ two-state theory, k_{nr}^{LE} is the non-radiative rate for the LE state according to MLJ theory, f_{CT-LE} describes the contributions of k_{nr}^{LE} to k_{nr}, and ΔE_{LE-CT} is the difference between the adiabatic LE and CT energies.

Using the experimental k_{nr}^{LE} rates for m-MTDATA and 3TPYMB, the experimental optical-gap (adiabatic) energy (see Appendix Section 3), and the DFT electronic coupling between the CT and LE states (assuming that this coupling is the same for both m-MTDATA and 3TPYMB), we estimate that CT-LE mixing leads to an increase in k_{nr} by a factor of about $3\text{x}10^4$ s^{-1}; this value is in very good qualitative agreement with the experimental value of $9.8\text{x}10^4$ s^{-1}. To rationalize the k_r value in the context of the three-state model, a similar procedure can be performed for the transition dipole moments:[59,60]

$$(d_r^{\mathrm{CT}})^2 = (1 - f_{CT-LE})\left(d_{CT-G}\right)^2 + f_{CT-LE}\,(d_r^{LE})^2 \qquad \text{Eqn. 3.6}$$

The derived transition dipole moment can be then used to calculate the radiative rates by means of Eqn. S8 or S10. For the m-MTDATA:3TPYMB blend, the contribution to k_r from CT-LE hybridization is smaller than that due to CT-G hybridization. Thus, we conclude that the non-radiative transitions in the m-MTDATA:3TPYMB blend are governed by the coupling of the CT

states with the LE states while the radiative decay of the CT state is dominated by the CT-G coupling.

3.6 Influence of LE's transitions rates on CT state

These findings for the m-MTDATA:3TPYMB system indicate that in D:A blends with CT energies above 2 eV, the PLQY of the blend can be much larger than the PLQY values of the pristine D and A components as a result of the very small intrinsic non-radiative rates of the CT states. However, the blend's PLQY can decrease due to CT-LE mixing since the large k_{nr} value of the LE state can significantly speed up the CT-state k_{nr}. Overall, what these results tell us is that a strong hybridization between the CT and ground states, and a weak hybridization between the CT and LE states can result in blends with very large PLQYs even for D and A components with moderate individual PLQY values.

This phenomenon is in stark contrast with what is found in donor/acceptor blends commonly used for OPV applications. According to the Shockley-Queisser model, to obtain highly efficient solar cells, the bandgap (and hence CT-state energies) should be in the range of 1.0-1.6 eV.[1] In such instances, the CT non-radiative rates are significant. Thus, in order to minimize the non-radiative voltage loss, CT-LE mixing with an LE state having a high PLQY is beneficial, in such a way that the CT-state emission can "borrow intensity" from the LE state.[3,24,56] A small LE-CT energy gap is then desirable in this case.[24]

In order to better illustrate the effect of CT-LE hybridization over a range of CT energies, we calculated the blend's (CT) PLQY as a function of LE-CT energy (**Figure 3.7**, red trace). In this calculation, the electronic couplings between the CT states and the ground and LE states (V_{CT-G} and V_{CT-LE}), the transition dipole moment (d_{CT-G} , estimated according to Eqn. 3.3), the LE adiabatic energy (E_{LE}), and the LE radiative and non-radiative rates (k_r^{LE} and k_{nr}^{LE}) are fixed as given in the **Figure 3.7** caption. In the two-state model (**Figure 3.7**, red trace), the blend's PLQY saturates when E_{CT} approaches 2 eV because k_{nr} is significantly smaller than k_r. In the three-state model, however, the maximum PLQY of the blend is obtained at CT energies of about 2 eV. When the adiabatic energy of the CT state approaches that of the LE states, the CT-LE hybridization becomes "activated" and the LE-state large k_{nr} value carries over to the CT k_{nr} (**Figure 3.7b**), which reduces the blend's PLQY.

Recent OPV studies concluded that in the context of CT-LE mixing, the LE PLQY sets an upper limit for the CT PLQY. We wondered whether this holds true in the case of high-gap blends, where the LE k_{nr} contributes significantly to the CT k_{nr}. We calculated the CT transition rates and PLQY, while keeping $PLQY_{LE}$ fixed at 10% but considering a range of values for the LE lifetimes (τ_{LE}). **Figure 3.7** shows that τ_{LE} can affect the blend's PLQY. Specifically, when τ_{LE} becomes longer, the blend's PLQY increases (**Figure 3.7c**, solid blue circles), whereas a shorter τ_{LE} (open blue circles) leads to smaller PLQY of the blend. Furthermore, we evaluated the influence of $PLQY_{LE}$ on the blend (See Appendix B Section 7). In this series of calculations, we increased k_r^{LE} or decreased k_{nr}^{LE} to obtain a higher $PLQY_{LE}$ (80%) (Figure S7). The blend's (CT) PLQY maximizes when $PLQY_{LE}$ is increased by reducing k_{nr}^{LE} rather than increasing k_r^{LE}. Here as well, a longer τ_{LE} is beneficial for the blend's PLQY at higher CT energies. Finally, we show in Figures S8 and S9 that a moderate change of the electronic couplings has little effect on the CT PLQY. Thus, for blends with large LE PLQY values, the CT PLQY increases systematically with an

increase in CT energy. This finding is in line with the data obtained for blends where, upon blend dilution, the blend emission energy and PLQY increase concomitantly.[61,62]

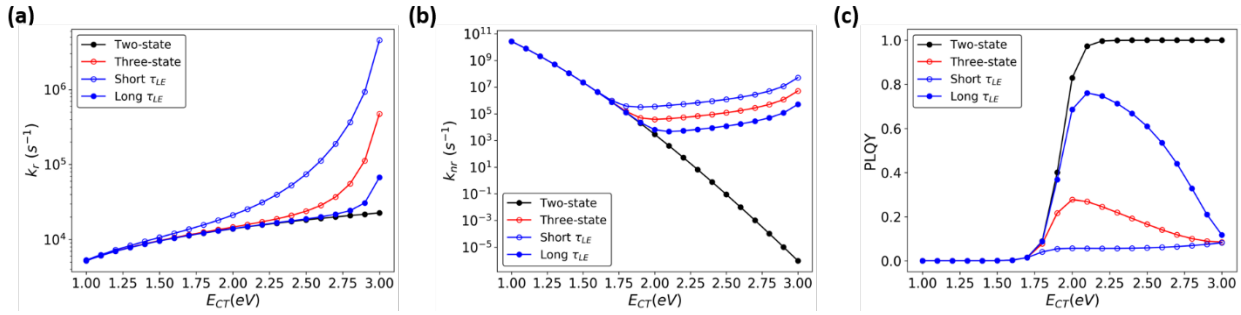

Figure 3.7 (a) k_r **(b)** k_{nr}, and **(c)** PLQY calculated for a range of E_{CT} values, based on two-state MLJ (black) and three-state models (blue and red). The red line represents results based on a three-state model using the LE lifetime (Table S1, τ_{LE}=2.12 ns), while the blue traces represent results from three-state model calculations where τ_{LE} was increased (shown in solid circles) or decreased (shown in open circles) by 10-fold, by manipulating k_r and k_{nr} simultaneously. Parameters used: E_{CT}=1.0-3.0 eV, V_{CT-G} =10 meV and V_{CT-LE}=10 meV, d_{CT-G} = 0.049 D, d_r^{LE} = 3.58 D, $k_{nr}^{LE} = 4.2 \times 10^8 s^{-1}$, $k_r^{LE} = 5.14 \times 10^7 s^{-1}$ are based on parameters for pure m-MTDATA and the blend (Appendix B Table S1).

3.7 Conclusion

In summary, we have demonstrated that a highly emissive and charge-generating organic photovoltaic based on a TADF-emitting CT state can exhibit an extremely small non-radiative recombination loss, ΔV_{OC}^{nr}, of only ~0.1 V and a photocurrent EQE_{max} of 24%. Compared to previously reported OPV blends, this model system demonstrates an extremely slow non-radiative recombination rate of 9.8x10^4 s^{-1}, approximately 4 to 5 orders of magnitude slower than in typical efficient polymer/NFA blends.

In this context, we re-examined the "Energy Gap Law" for non-radiative voltage loss by using the two-state Marcus-Levich-Jortner approach[20] and tuning the molecular parameters such as reorganization energy and change in dipole moment. We find that, for values of reorganization energies that are consistent with the spectral lineshapes in the MLJ picture, the non-radiative recombination rate in our blend is much faster than the MLJ model estimates.

As a result, we conclude that a three-state model that includes the local exciton state in addition to the CT and ground states is required to understand our observations. We show that the hybridization between the CT and LE states, which was previously considered to enhance only the radiative decay rates of the CT states (via intensity borrowing), can in fact also speed up the non-radiative decay, thus compromising the CT PLQY. Furthermore, in the context of the three-state model, for organic blends with CT energies over 2.0 eV, to achieve an optimal PLQY requires not only choosing low-gap components with a high PLQY, but also an evaluation of how the k_r and k_{nr} rates from the LE states tune the CT PLQY via CT-LE mixing. This consideration must inform the material selection for high-gap CT-based OLEDs.

Appendix B

Experimental method and supplementary information for Chapter 3.

Acknowledgement

The work at the University of Washington was supported by the Office of Naval Research through grant number N00014-17-1-2201. The theoretical work is supported by the Department of Energy through grant number DEEE0008205. Part of this work was conducted at the Molecular Analysis Facility, a National Nanotechnology Coordinated Infrastructure site at the University of Washington, which is supported in part by the National Science Foundation (grant ECC-1542101), the University of Washington, the Molecular Engineering & Sciences Institute, the Clean Energy Institute, and the National Institutes of Health. We thank Dr. Jian Wang and Dr. Mark Ziffer for valuable discussions, and Karisse Yamamoto for help with the literature survey.

References

(1) Shockley, W.; Queisser, H. J. Detailed Balance Limit of Efficiency of P-n Junction Solar Cells. *J. Appl. Phys.* **1961**, *32* (3), 510–519. https://doi.org/10.1063/1.1736034.

(2) Miller, O. D.; Yablonovitch, E.; Kurtz, S. R. Strong Internal and External Luminescence as Solar Cells Approach the Shockley-Queisser Limit. *IEEE J. Photovoltaics* **2012**, *2* (3), 303–311. https://doi.org/10.1109/JPHOTOV.2012.2198434.

(3) Coropceanu, V.; Chen, X.-K.; Wang, T.; Zheng, Z.; Brédas, J.-L. Charge-Transfer Electronic States in Organic Solar Cells. *Nat. Rev. Mater.* **2019**, *4* (11), 689–707. https://doi.org/10.1038/s41578-019-0137-9.

(4) Liu, X.; Li, Y.; Ding, K.; Forrest, S. Energy Loss in Organic Photovoltaics: Nonfullerene Versus Fullerene Acceptors. *Phys. Rev. Appl.* **2019**, *11* (2), 024060. https://doi.org/10.1103/PhysRevApplied.11.024060.

(5) Xie, Y.; Wu, H. Balancing Charge Generation and Voltage Loss toward Efficient Nonfullerene Organic Solar Cells. *Mater. Today Adv.* **2020**, *5*, 100048. https://doi.org/10.1016/j.mtadv.2019.100048.

(6) Braly, I. L.; Dequilettes, D. W.; Pazos-Outón, L. M.; Burke, S.; Ziffer, M. E.; Ginger, D. S.; Hillhouse, H. W. Hybrid Perovskite Films Approaching the Radiative Limit with over 90% Photoluminescence Quantum Efficiency. *Nat. Photonics* **2018**, *12* (6), 355–361. https://doi.org/10.1038/s41566-018-0154-z.

(7) Dequilettes, D. W.; Koch, S.; Burke, S.; Paranji, R. K.; Shropshire, A. J.; Ziffer, M. E.; Ginger, D. S. Photoluminescence Lifetimes Exceeding 8 Ms and Quantum Yields Exceeding 30% in Hybrid Perovskite Thin Films by Ligand Passivation. *ACS Energy Lett.* **2016**, *1* (2), 438–444. https://doi.org/10.1021/acsenergylett.6b00236.

(8) Green, M. A.; Dunlop, E. D.; Hohl-Ebinger, J.; Yoshita, M.; Kopidakis, N.; Ho-Baillie, A. W. Y. Solar Cell Efficiency Tables (Version 55). *Prog. Photovoltaics Res. Appl.* **2020**, *28* (1), 3–15. https://doi.org/10.1002/pip.3228.

(9) Yoo, J. J.; Wieghold, S.; Sponseller, M. C.; Chua, M. R.; Bertram, S. N.; Hartono, N. T. P.; Tresback, J. S.; Hansen, E. C.; Correa-Baena, J. P.; Bulović, V.; Buonassisi, T.; Shin, S. S.; Bawendi, M. G. An Interface Stabilized Perovskite Solar Cell with High Stabilized Efficiency and Low Voltage Loss. *Energy Environ. Sci.* **2019**, *12* (7), 2192–2199. https://doi.org/10.1039/c9ee00751b.

(10) Benduhn, J.; Tvingstedt, K.; Piersimoni, F.; Ullbrich, S.; Fan, Y.; Tropiano, M.; McGarry, K. A.; Zeika, O.; Riede, M. K.; Douglas, C. J.; Barlow, S.; Marder, S. R.; Neher, D.; Spoltore, D.; Vandewal, K. Intrinsic Non-Radiative Voltage Losses in Fullerene-Based Organic Solar Cells. *Nat. Energy* **2017**, *2* (6), 17053. https://doi.org/10.1038/nenergy.2017.53.

(11) An, N.; Cai, Y.; Wu, H.; Tang, A.; Zhang, K.; Hao, X.; Ma, Z.; Guo, Q.; Ryu, H. S.; Woo, H. Y.; Sun, Y.; Zhou, E. Solution-Processed Organic Solar Cells with High Open-Circuit Voltage of 1.3 V and Low Non-Radiative Voltage Loss of 0.16 V. *Adv. Mater.* **2020**, *2002122*, 1–7. https://doi.org/10.1002/adma.202002122.

(12) Ziffer, M. E.; Jo, S. B.; Zhong, H.; Ye, L.; Liu, H.; Lin, F.; Zhang, J.; Li, X.; Ade, H. W.; Jen, A. K.-Y.; Ginger, D. S. Long-Lived, Non-Geminate, Radiative Recombination of Photogenerated Charges in a Polymer/Small-Molecule Acceptor Photovoltaic Blend. *J. Am. Chem. Soc.* **2018**, *140* (31), 9996–10008. https://doi.org/10.1021/jacs.8b05834.

(13) Liu, S.; Yuan, J.; Deng, W.; Luo, M.; Xie, Y.; Liang, Q.; Zou, Y.; He, Z.; Wu, H.; Cao, Y. High-Efficiency Organic Solar Cells with Low Non-Radiative Recombination Loss and Low Energetic Disorder. *Nat. Photonics* **2020**, *14* (5), 300–305. https://doi.org/10.1038/s41566-019-0573-5.

(14) Cui, Y.; Yao, H.; Zhang, J.; Zhang, T.; Wang, Y.; Hong, L.; Xian, K.; Xu, B.; Zhang, S.; Peng, J.; Wei, Z.; Gao, F.; Hou, J. Over 16% Efficiency Organic Photovoltaic Cells Enabled by a Chlorinated Acceptor with Increased Open-Circuit Voltages. *Nat. Commun.* **2019**, *10* (1), 2515. https://doi.org/10.1038/s41467-019-10351-5.

(15) Qian, D.; Zheng, Z.; Yao, H.; Tress, W.; Hopper, T. R.; Chen, S.; Li, S.; Liu, J.; Chen, S.; Zhang, J.; Liu, X.-K.; Gao, B.; Ouyang, L.; Jin, Y.; Pozina, G.; Buyanova, I. A.; Chen, W. M.; Inganäs, O.; Coropceanu, V.; Bredas, J.-L.; Yan, H.; Hou, J.; Zhang, F.; Bakulin, A. A.; Gao, F. Design Rules for Minimizing Voltage Losses in High-Efficiency Organic Solar Cells. *Nat. Mater.* **2018**, *17* (8), 703–709. https://doi.org/10.1038/s41563-018-0128-z.

(16) Liu, X.; Du, X.; Wang, J.; Duan, C.; Tang, X.; Heumueller, T.; Liu, G.; Li, Y.; Wang, Z.; Wang, J.; Liu, F.; Li, N.; Brabec, C. J.; Huang, F.; Cao, Y. Efficient Organic Solar Cells with Extremely High Open-Circuit Voltages and Low Voltage Losses by Suppressing Nonradiative Recombination Losses. *Adv. Energy Mater.* **2018**, *8* (26), 1–9. https://doi.org/10.1002/aenm.201801699.

(17) Cui, Y.; Yao, H.; Zhang, J.; Xian, K.; Zhang, T.; Hong, L.; Wang, Y.; Xu, Y.; Ma, K.; An, C.; He, C.; Wei, Z.; Gao, F.; Hou, J. Single-Junction Organic Photovoltaic Cells with Approaching 18% Efficiency. *Adv. Mater.* **2020**, *1908205*, 1–7. https://doi.org/10.1002/adma.201908205.

(18) Kirchartz, T.; Rau, U.; Kurth, M.; Mattheis, J.; Werner, J. H. Comparative Study of Electroluminescence from Cu(In,Ga)Se2 and Si Solar Cells. *Thin Solid Films* **2007**, *515* (15 SPEC. ISS.), 6238–6242. https://doi.org/10.1016/j.tsf.2006.12.105.

(19) Engleman, R.; Jortner, J. The Energy Gap Law for Radiationless Transitions in Large Molecules. *Mol. Phys.* **1970**, *18* (2), 145–164.

(20) Azzouzi, M.; Yan, J.; Kirchartz, T.; Liu, K.; Wang, J.; Wu, H.; Nelson, J. Nonradiative Energy Losses in Bulk-Heterojunction Organic Photovoltaics. *Phys. Rev. X* **2018**, *8* (3), 1–14. https://doi.org/10.1103/PhysRevX.8.031055.

(21) Kahle, F. J.; Rudnick, A.; Bässler, H.; Köhler, A. How to Interpret Absorption and Fluorescence Spectra of Charge Transfer States in an Organic Solar Cell. *Mater. Horizons* **2018**, *5* (5), 837–848. https://doi.org/10.1039/c8mh00564h.

(22) Panhans, M.; Hutsch, S.; Benduhn, J.; Schellhammer, K. S.; Nikolis, V. C.; Vangerven, T.; Vandewal, K.; Ortmann, F. Molecular Vibrations Reduce the Maximum Achievable Photovoltage in Organic Solar Cells. *Nat. Commun.* **2020**, *11* (1), 1–10. https://doi.org/10.1038/s41467-020-15215-x.

(23) Qian, D.; Zheng, Z.; Yao, H.; Tress, W.; Hopper, T. R.; Chen, S.; Li, S.; Liu, J.; Chen, S.; Zhang, J.; Liu, X. K.; Gao, B.; Ouyang, L.; Jin, Y.; Pozina, G.; Buyanova, I. A.; Chen, W. M.; Inganäs, O.; Coropceanu, V.; Bredas, J. L.; Yan, H.; Hou, J.; Zhang, F.; Bakulin, A. A.; Gao, F. Design Rules for Minimizing Voltage Losses in High-Efficiency Organic Solar Cells. *Nat. Mater.* **2018**, *17* (8), 703–709. https://doi.org/10.1038/s41563-018-0128-z.

(24) Eisner, F. D.; Azzouzi, M.; Fei, Z.; Hou, X.; Anthopoulos, T. D.; Dennis, T. J. S.; Heeney, M.; Nelson, J. Hybridization of Local Exciton and Charge-Transfer States Reduces Nonradiative Voltage Losses in Organic Solar Cells. *J Am Chem Soc* **2019**, *141*, 6362–6374. https://doi.org/10.1021/jacs.9b01465.

(25) Giro, G.; Cocchi, M.; Kalinowski, J.; Di Marco, P.; Fattori, V. Multicomponent Emission from Organic Light Emitting Diodes Based on Polymer Dispersion of an Aromatic Diamine and an Oxadiazole Derivative. *Chem. Phys. Lett.* **2000**, *318* (1–3), 137–141. https://doi.org/10.1016/S0009-2614(99)01456-6.

(26) Zhang, M.; Zheng, C.; Lin, H.; Tao, S.-L. Thermally Activated Delayed Fluorescence Exciplex Emitters for High-Performance Organic. *Mater. Horizons* **2021**, *8*, 401–425. https://doi.org/10.1039/d0mh01245a.

(27) King, S. M.; Hintschich, S. I.; Dai, D.; Rothe, C.; Monkman, A. P. Spiroconjugation-Enhanced Intramolecular Charge-Transfer State Formation in a Polyspirobifluorene Homopolymer. *J. Phys. Chem. C* **2007**, *111* (50), 18759–18764. https://doi.org/10.1021/jp0755138.

(28) Chen, X.; Kim, D.; Bredas, J. Thermally Activated Delayed Fluorescence (TADF) Path toward E Ffi Cient Electroluminescence in Purely Organic Materials : Molecular Level Insight. *Acc. Chem. Res.* **2018**, *51*, 2215–2224. https://doi.org/10.1021/acs.accounts.8b00174.

(29) Gibson, J.; Monkman, A. P.; Penfold, T. J. The Importance of Vibronic Coupling for Efficient Reverse Intersystem Crossing in Thermally Activated Delayed Fluorescence Molecules. *ChemPhysChem* **2016**, No. 1, 2956–2961. https://doi.org/10.1002/cphc.201600662.

(30) Santos, P. L.; Dias, F. B.; Monkman, A. P. Investigation of the Mechanisms Giving Rise to TADF in Exciplex States. *J. Phys. Chem. C* **2016**, *120*, 18259–18267. https://doi.org/10.1021/acs.jpcc.6b05198.

(31) Goushi, K.; Yoshida, K.; Sato, K.; Adachi, C. Organic Light-Emitting Diodes Employing Efficient Reverse Intersystem Crossing for Triplet-to-Singlet State Conversion. *Nat. Photonics* **2012**, *6* (4), 253–258. https://doi.org/10.1038/nphoton.2012.31.

(32) Deotare, P. B.; Chang, W.; Hontz, E.; Congreve, D. N.; Shi, L.; Reusswig, P. D.; Modtland, B.; Bahlke, M. E.; Lee, C. K.; Willard, A. P.; Bulovic, V.; Van Voorhis, T.; Baldo, M. A. Nanoscale Transport of Charge-Transfer States in Organic Donor-Acceptor Blends. *Nat. Mater.* **2015**, *14* (11), 1130–1134. https://doi.org/10.1038/nmat4424.

(33) Chang, W.; Congreve, D. N.; Hontz, E.; Bahlke, M. E.; Mcmahon, D. P.; Voorhis, T. Van; Baldo, M. A.; Reineke, S.; Wu, T. C.; Bulovic, V. Spin-Dependent Charge Transfer State Design Rules in Organic Photovoltaics. *Nat. Commun.* **2015**, 1–6. https://doi.org/10.1038/ncomms7415.

(34) Bunzmann, N.; Weissenseel, S.; Kudriashova, L.; Gruene, J.; Krugmann, B.; Grazulevicius, J. V.; Sperlich, A.; Dyakonov, V. Optically and Electrically Excited Intermediate Electronic States in Donor:Acceptor Based OLEDs. *Mater. Horizons* **2020**, *7* (4), 1126–1137. https://doi.org/10.1039/c9mh01475f.

(35) Goushi, K.; Yoshida, K.; Sato, K.; Adachi, C. Organic Light-Emitting Diodes Employing Efficient Reverse Intersystem Crossing for Triplet-to-Singlet State Conversion. *Nat. Photonics* **2012**, *6* (4), 253–258. https://doi.org/10.1038/nphoton.2012.31.

(36) Sulas, D. B.; Rabe, E. J.; Schlenker, C. W. Kinetic Competition between Charge Separation and Triplet Formation in Small-Molecule Photovoltaic Blends. *J. Phys. Chem. C* **2017**, *121* (48), 26667–26676. https://doi.org/10.1021/acs.jpcc.7b09365.

(37) Byrnes, S. J. Multilayer Optical Calculations. *arXiv 1603 . 02720v3* **2018**, 1–20.

(38) Ullbrich, S.; Benduhn, J.; Jia, X.; Nikolis, V. C.; Tvingstedt, K.; Piersimoni, F.; Roland, S.; Liu, Y.; Wu, J.; Fischer, A.; Neher, D.; Reineke, S.; Spoltore, D.; Vandewal, K. Emissive and Charge-Generating Donor–Acceptor Interfaces for Organic Optoelectronics with Low Voltage Losses. *Nat. Mater.* **2019**, *18* (5), 459–464. https://doi.org/10.1038/s41563-019-0324-5.

(39) Zhao, W.; Qian, D.; Zhang, S.; Li, S.; Inganäs, O.; Gao, F.; Hou, J. Fullerene-Free Polymer Solar Cells with over 11% Efficiency and Excellent Thermal Stability. *Adv. Mater.* **2016**, *28* (23), 4734–4739. https://doi.org/10.1002/adma.201600281.

(40) Zhang, J.; Kan, B.; Pearson, A. J.; Parnell, A. J.; Cooper, J. F. K.; Liu, X. K.; Conaghan, P. J.; Hopper, T. R.; Wu, Y.; Wan, X.; Gao, F.; Greenham, N. C.; Bakulin, A. A.; Chen, Y.; Friend, R. H. Efficient Non-Fullerene Organic Solar Cells Employing Sequentially Deposited Donor-Acceptor Layers. *J. Mater. Chem. A* **2018**, *6* (37), 18225–18233. https://doi.org/10.1039/c8ta06860g.

(41) Liu, J.; Chen, S.; Qian, D.; Gautam, B.; Yang, G.; Zhao, J.; Bergqvist, J.; Zhang, F.; Ma, W.; Ade, H.; Inganäs, O.; Gundogdu, K.; Gao, F.; Yan, H. Fast Charge Separation in a Non-Fullerene Organic Solar Cell with a Small Driving Force. *Nat. Energy* **2016**, *1* (7), 16089–16095. https://doi.org/10.1038/nenergy.2016.89.

(42) Ran, N. A.; Love, J. A.; Takacs, C. J.; Sadhanala, A.; Beavers, J. K.; Collins, S. D.; Huang, Y.; Wang, M.; Friend, R. H.; Bazan, G. C. Harvesting the Full Potential of Photons with Organic Solar Cells. *Adv. Mater.* **2016**, 1482–1488. https://doi.org/10.1002/adma.201504417.

(43) Wang, C.; Xu, X.; Zhang, W.; Bergqvist, J.; Xia, Y.; Meng, X.; Bini, K.; Ma, W.; Yartsev, A.; Vandewal, K.; Andersson, M. R.; Inganäs, O.; Fahlman, M.; Wang, E. Low Band Gap Polymer Solar Cells With Minimal Voltage Losses. *Adv. Energy Mater.* **2016**, *6* (18), 1–10. https://doi.org/10.1002/aenm.201600148.

(44) Rau, U. Reciprocity Relation between Photovoltaic Quantum Efficiency and Electroluminescent Emission of Solar Cells. *Phys. Rev. B* **2007**, *76* (8), 1–8. https://doi.org/10.1103/PhysRevB.76.085303.

(45) Rau, U.; Blank, B.; Müller, T. C. M.; Kirchartz, T.; Jülich, F. Efficiency Potential of Photovoltaic Materials and Devices Unveiled by Detailed-Balance Analysis. *Phys. Rev. Appl.* **2017**, No. 7, 044016. https://doi.org/10.1103/PhysRevApplied.7.044016.

(46) Baran, D.; Kirchartz, T.; Wheeler, S.; Dimitrov, S.; Abdelsamie, M.; Gorman, J.; Ashraf, R. S.; Holliday, S.; Wadsworth, A.; Gasparini, N.; Kaienburg, P.; Yan, H.; Amassian, A.; Brabec, C. J.; Durrant, J. R.; Mcculloch, I. Reduced Voltage Losses Yield 10% Efficient Fullerene Free Organic Solar Cells with 41 V Open Circuit Voltages. *Energy Environ. Sci.* **2016**, *9*, 3783–3793. https://doi.org/10.1039/C6EE02598F.

(47) Ullbrich, S.; Benduhn, J.; Jia, X.; Nikolis, V. C.; Tvingstedt, K.; Piersimoni, F.; Roland, S.; Liu, Y.; Wu, J.; Fischer, A.; Neher, D.; Reineke, S.; Spoltore, D.; Vandewal, K. Emissive and Charge-Generating Donor–Acceptor Interfaces for Organic Optoelectronics with Low Voltage Losses. *Nat. Mater.* **2019**, *18* (5), 459–464. https://doi.org/10.1038/s41563-019-0324-5.

(48) Jortner, J. Temperature Dependent Activation Energy for Electron Transfer between Biological Molecules. *J. Chem. Phys.* **1976**, *64* (12), 4860–4867. https://doi.org/10.1063/1.432142.

(49) Azzouzi, M.; Yan, J.; Kirchartz, T.; Liu, K.; Wang, J.; Wu, H.; Nelson, J. Nonradiative Energy Losses in Bulk-Heterojunction Organic Photovoltaics. *Phys. Rev. X* **2018**, *8* (3), 031055. https://doi.org/10.1103/PhysRevX.8.031055.

(50) Wang, T.; Coropceanu, V.; Brédas, J.-L. All-Polymer Solar Cells: Impact of the Length of the Branched Alkyl Side Chains on the Polymer Acceptors on the Interchain Packing and Electronic Properties in Amorphous Blends. *Chem. Mater.* **2019**, *31* (16), 6239–6248. https://doi.org/10.1021/acs.chemmater.9b02284.

(51) Hush, N. S. Homogeneous and Heterogeneous Optical and Thermal Electron Transfer. *Electrochim. Acta* **1968**, *13* (5), 1005–1023. https://doi.org/10.1016/0013-4686(68)80032-5.

(52) Hush, N. S. Theoretical Considerations and Spectroscopic Data. *Prog. Inorg. Chem.* **1967**, *8*, 391–444.

(53) Mulliken, R. S. Molecular Compounds and Their Spectra. II. *J. Am. Chem. Soc.* **1952**, *74* (3), 811–824. https://doi.org/10.1021/ja01123a067.

(54) Burke, T. M.; Sweetnam, S.; Vandewal, K.; McGehee, M. D. Beyond Langevin Recombination: How Equilibrium Between Free Carriers and Charge Transfer States Determines the Open-Circuit Voltage of Organic Solar Cells. *Adv. Energy Mater.* **2015**, *5* (11), 1500123. https://doi.org/10.1002/aenm.201500123.

(55) Oh, D. H.; Sano, M.; Boxer, S. G. Electroabsorption (Stark Effect) Spectroscopy of Mono- and Biruthenium Charge-Transfer Complexes: Measurements of Changes in Dipole Moments and

Other Electrooptic Properties. *J. Am. Chem. Soc.* **1991**, *113* (18), 6880–6890. https://doi.org/10.1021/ja00018a026.

(56) Chen, X.-K.; Coropceanu, V.; Brédas, J.-L. Assessing the Nature of the Charge-Transfer Electronic States in Organic Solar Cells. *Nat. Commun.* **2018**, *9* (1), 5295. https://doi.org/10.1038/s41467-018-07707-8.

(57) Cho, E.; Coropceanu, V.; Brédas, J. L. Organic Neutral Radical Emitters: Impact of Chemical Substitution and Electronic-State Hybridization on the Luminescence Properties. *J. Am. Chem. Soc.* **2020**, *142* (41), 17782–17786. https://doi.org/10.1021/jacs.0c08997.

(58) Gould, I. R.; Farid, S. Radiationless Decay in Exciplexes with Variable Charge Transfer. *J. Phys. Chem. B* **2007**, *111* (24), 6782–6787. https://doi.org/10.1021/jp069053e.

(59) Bixon, M.; Jortner, J.; Cortes, J.; Heitele, H.; Michel-Beyerle, M. E. Energy Gap Law for Nonradiative and Radiative Charge Transfer in Isolated and in Solvated Supermolecules. *J. Phys. Chem.* **1994**, *98* (30), 7289–7299. https://doi.org/10.1021/j100081a010.

(60) Bixon, M.; Jortner, J.; Verhoeven, J. W. Lifetimes for Radiative Charge Recombination in Donor-Acceptor Molecules. *J. Am. Chem. Soc.* **1994**, *116* (16), 7349–7355. https://doi.org/10.1021/ja00095a044.

(61) Chapran, M.; Pander, P.; Vasylieva, M.; Wiosna-Salyga, G.; Ulanski, J.; Dias, F. B.; Data, P. Realizing 20% External Quantum Efficiency in Electroluminescence with Efficient Thermally Activated Delayed Fluorescence from an Exciplex. *ACS Appl. Mater. Interfaces* **2019**, *11* (14), 13460–13471. https://doi.org/10.1021/acsami.8b18284.

(62) Colella, M.; Danos, A.; Monkman, A. P. Less Is More: Dilution Enhances Optical and Electrical Performance of a TADF Exciplex. *J. Phys. Chem. Lett.* **2019**, *10* (4), 793–798. https://doi.org/10.1021/acs.jpclett.8b03646.

Chapter 4. Experimental methods for probing CT-LE mixing

4.1 Introduction

In the past couple of years, there has been significant progress in the photovoltaic performance of polymer/non-fullerene acceptor OPV blends, with the highest efficiency climbing over 18%.[1] A significant amount of research efforts has focused on maximizing the open-circuit voltage (V_{OC}). As discussed in Chapter 1, three processes hinder an organic solar cell from achieving the theoretical maximum V_{OC}: (1) non-ideal charge generation, (2) excess radiative recombination due to absorption in the bandedge, and (3) non-radiative recombination.

Non-radiative recombination loss contributes to a significant amount of the total energy loss in OPVs. Since the photoluminescence of the charge-transfer (CT) state determines the non-radiative recombination loss, in Chapter 3, we examine the theoretical limit for non-radiative recombination loss via an intrinsically emissive CT state-based organic blend.

Using emissive CT states to reduce non-radiative recombination loss has successfully been applied in some of the most efficient OPV devices.[2–5] Specifically, high PLQY has been demonstrated in polymer/NFA blends where CT and LE have small adiabatic energy differences, resulting in non-radiative recombination loss below 0.2 V. Intriguingly, the non-radiative loss for several systems is lower than what the Marcus-Levich-Jortner model predicts.[2,3] Theoretical work has attributed these observations to wavefunction mixing between CT and LE states.[3,4,6] As we discussed in Chapter 3, wavefunction mixing between CT and LE influences CT's emission yield only when CT-LE coupling becomes comparable to CT-ground state coupling. This happens when (1) CT-GS coupling is very small due to CT's large band gap (such as in m-MTDATA:3TPYMB blend I discussed in Chapter 3) and (2) when the CT-LE energetic offset is small. When LE is highly emissive, CT state can borrow emission intensity via wavefunction mixing.

A three-state model that accounts for energetics of CT, LE and the ground state aptly predicts PL properties observed in experiments. However, to the best of our knowledge, experimental evidence that shows CT-LE mixing has not been reported in OPV blends. The main challenge lies in CT's low oscillator strength and low absorption and emission thereof. Highly sensitive spectroscopy measurements are thus required.

Electroabsorption (EA) spectroscopy detects changes in the molecule's absorption when an external electric field is applied. It has been shown as a useful approach to study optical charge-transfer transitions of molecules with applications in chemistry, biology, and material sciences.[7] Macroscopic parameters including change in dipole moment and change in polarizability can be extracted via EA spectra.[8–10] Moreover, since certain optical transition becomes allowed under an electric field, EA is a powerful tool to examine in detail the energetics of electronic structures of the molecule.[11–13] It has been shown to detect the electronic coupling between excited states that are close in energy[12,14–16] and to determine binding energies of Wannier exciton in perovskite materials[17]. In the next few sections, I propose and show encouraging results that electroabsorption spectroscopy is a useful method to directly probe CT-LE mixing.

4.2 Origin of field-induced absorption shift

An electric field can interact with the wavefunction of the molecule thereby inducing changes in the absorption and emission of the molecule. The field-induced shift has three contributions: Stark effect, change in oscillator strengths of electronic states, and change of the selection rules for electronic transitions.[7,13] Under the application of an externally applied electric field F, the absorption coefficient shift $\Delta\alpha(E)$ can be described as the difference of the absorption perturbed by the electric field $\alpha^F(E)$ and that without an applied electric field $\alpha(E)$.

$$\Delta\alpha(E) = \alpha^F(E) - \alpha(E) \qquad \text{Eqn. 4.1}$$

Stark effect describes the energy shift of the entire absorption band by an amount ΔE via a linear and a quadratic term based on their field strength dependence (Eqn. 4.2).[9] The linear term describes how the electric field acts on permanent or disorder-induced dipoles (**m**), whereas the quadratic term describes energy shift due to change of polarizability (Δp) in the presence of the electric field.

$$\Delta E = \Delta\mu \cdot F + \frac{1}{2} F \cdot \Delta p \cdot F \text{ Eqn. 4.2}$$

In the presence of an electric field, energy levels lying close to each other can couple, resulting in a redistribution of oscillator strength among them. For example, when a forbidden transition lies close to an absorption, the intensity of the absorption signal will be reduced if the forbidden transition becomes allowed with the applied field. Thus, the field-induced change in absorption coefficient is

$$\alpha^F(E) = k\alpha(E + \Delta E) \qquad \text{Eqn. 4.3}$$

Inserting Eqn. 4.3 into Eqn. 4.1 and taking the Taylor series truncated to the second derivative, we thus express the field-induced absorption coefficient shift as:

$$\Delta\alpha(E) = (k-1)\alpha(E) + k\Delta E \frac{d\alpha(E)}{dE} + \frac{k\Delta E^2}{2} \frac{d^2\alpha(E)}{dE^2} \quad \text{Eqn 4.4}$$

This means that electroabsorption spectrum is expected to be a linear combination of the absorption describing the redistribution of oscillator strength and the first and second derivative of the absorption describing Stark effect.

Furthermore, reports on polymers, small organic molecules and crystals have shown that new absorption features that are previously forbidden may appear when an external electric field is applied, as the electric field breaks the symmetry of the molecules.[9,11,13,14] Since the Liptay equation assumes non-interacting electronic states, EA spectra cannot be fully described. Theoretical methods such as sum-of-state and redfield theory are commonly applied to explain the additional absorption features.[11,12,16]

4.3 Probing energetics of CT and LE via EA spectroscopy

Hypothesis

Previous research has shown that the EA spectrum in small molecules consists of a derivative-like Stark shift of the lowest optically allowed exciton and its vibronic replicas.[14] In donor/acceptor OPV blends, local excitons of donor and acceptor molecules have randomly oriented dipole, causing the overall dipole moment to vanish. Stark effect for local excitons is thus dominated by

the field's effect on the change in polarizability, namely the quadratic term in Eqn. 4.2. Consequently, $\Delta\alpha(E)$ is expected to have a first-derivative lineshape. In contrast, CT excitations have large transition dipole moments, and thus $\Delta\mu \cdot F$ dominates the Stark effect. This means that the second-derivative term in Eqn. 4.4 is expected to dominate the EA response.[9]

Additionally, interference of an external electric field with electronic states may lead to redistribution of oscillator strengths. When electronic coupling between CT and LE is significant such that the emission properties of CT are influenced by the coupling and LE's energetics, we expect CT-LE mixing influence the absorption of the CT and LE state and thus their EA signatures are expected to deviate from derivative lineshapes.

We hypothesize that electroabsorption spectrum of a donor/acceptor blend should reflect the energetics of its photoexcited states and their interaction. Specifically, we focus on the low energy regions in EA spectra which indicate the nature of lowest optically allowed photoexcited states: whether the local exciton of the low gap component or the CT EA response dominates, and whether there is significant mixing between CT and LE states. We test our hypothesis via the following types of systems: D/A blend with weak CT oscillator strength, D/A blend with strong CT character but no CT-LE mixing and D/A blend with CT-LE mixing.

EA spectra of donor/acceptor blends

1. PTB7-Th:$PC_{60}BM$ blend

Previous research has shown that PTB7-Th:$PC_{60}BM$ blend exhibits low electroluminescence efficiency, indicating weak oscillator strength in CT.[4] We measured the change in transmission in terms of ΔT/T in PTB7-Th:$PC_{60}BM$. **Figure 4.1a** shows the normalized ΔT/T over a series of AC electric fields. The shape of the EA spectrum is invariant with the applied field and the amplitude of the low energy ΔT/T peak scales approximately quadratic with electric field strength (See **Appendix C Figure S2)**. We thus assign the EA signal to a χ^3 electro-optic response, as is typically the case for small molecules, semiconducting polymers and molecular crystals. **Figure 4.1b** compares normalized ΔT/T spectrum to the first and second derivatives of the absorption coefficient. Clearly, the low energy peak closely resembles the first derivative of k, indicating that the lowest photoexcited state giving rise to this feature has negligible $\Delta\mu$, for example, local exciton of PTB7-Th. To analyze Stark effect in PTB7-Th:$PC_{60}BM$, we use Liptay formula, shown in terms of the change in the imaginary part of the refractive index (k) in **Eqn. 4.5**.[18] Details on data analysis are described in **Appendix C**.

$$\Delta A(\nu) = F^2\{A_\chi A(\nu) + \frac{B_\chi}{15hc}\nu\frac{d}{d\nu}\left(\frac{A(\nu)}{\nu}\right) + \frac{C_\chi}{30h^2c^2}\nu\frac{d^2}{d\nu^2}\left(\frac{A(\nu)}{\nu}\right) \qquad \text{Eqn. 4.5}$$

where χ is the experimental angle between the externally applied electric field and the polarization of the incident light, and coefficients A_χ, B_χ and C_χ contain information on the transition polarizability, transition hyperpolarizability, the transition moment between the ground-state and excited state. At the magic angle of χ~54.7, B_χ and C_χ simplify to:

$$B_\chi = \frac{\Delta p}{2hc} \qquad C_\chi = \frac{\Delta\mu^2}{6h^2c^2} \qquad \text{Eqn. 4.6}$$

To fit experimental spectrum to the Liptay equation, we use a transfer matrix method to determine transmittance through the sample stack with and without the field, based on refractive indices of

each layer in the device stack.[17,19] This method accounts for light interference and electric field modulation thereof within the sample stack, which is known to significantly affect optical absorption. **Figure 4.1b** shows Liptay equation aptly describes the ΔT/T low energy peak and its vibronic features. We obtain Δp to be ~100 A^3 and a negligible $\Delta\mu$ as the fit is dominated by the first-derivative term. The magnitude for Δp is on the same order for what has been reported for pure PCE10 polymer and other semiconducting polymers.[20,21] More importantly, for the purpose of our study, first-derivative lineshape observed herein suggest that CT state formed between PCE10 and $PC_{60}BM$ does not give observable EA response.

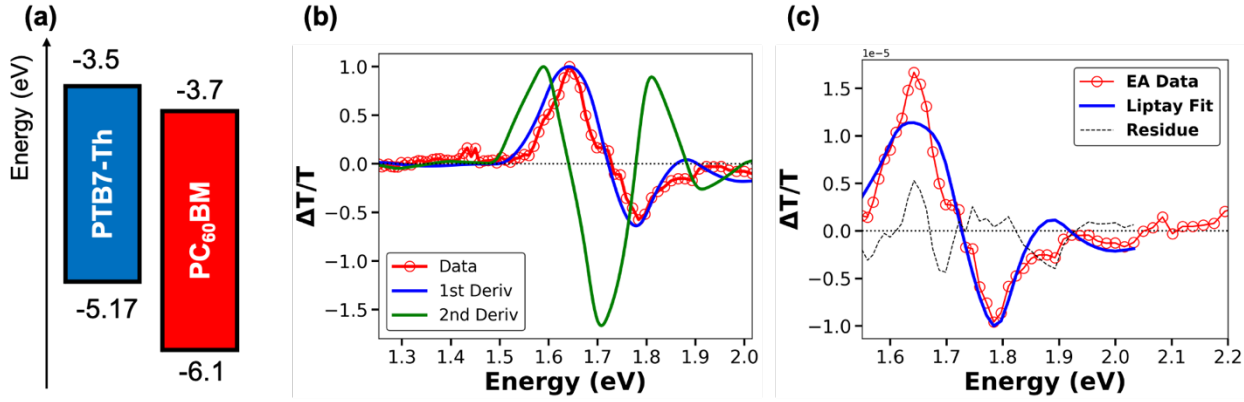

Figure 4.1 (a) Energy levels of PTB7-Th and $PC_{60}BM$. **(b)** Comparison of EA spectrum of PTB7-Th:$PC_{60}BM$ blend with 1st and 2nd derivatives of imaginary component in refractive index k. **(c)** Liptay fit of the EA spectrum and its residue.

2. PBDB-T:IT-4F blend

Next, we study the energetics of low-energy photoexcited states in a polymer/NFA blend, namely PBDB-T polymer as electron donor mixed with IT4F molecule as electron acceptor.[22] We expect efficient CT generation given good photovoltaic performance (EQE~70%). However, we do not expect electronic coupling between CT and LE in this system for the following reasons. First, energy levels of PBDB-T and IT-4F shown in **Figure 4.2a** suggest ~360 meV energy difference between CT and IT-4F low gap component. Second, PBDB-T:IT-4F exhibits ELQE of 1.9e-5% and thus non-radiative voltage loss of 0.39 V. These metrics are significantly lower than ELQE in pure IT4F of 1e-3%. In addition, **Figure 4.2b** shows that CT emission is significantly red-shifted from the LE emission by 310 meV. To summarize, we predict that although the CT oscillator strength is likely to be higher than PCE10:$PC_{60}BM$, CT-LE electronic coupling is insignificant.

We next examine the electric field induced absorption shift in PBDB-T:IT-4F blend and focus on the low energy region in the EA spectrum. **Figure 4.2c** shows that PBDB-T:IT-4F EA lineshape largely follows the second derivative of imaginary refractive index k, with some minor contribution from the first derivative. This is in stark contrast from what we observed in PCE10:$PC_{60}BM$, which closely resembles the first derivative lineshape.

At present, we are uncertain of what electronic interactions are responsible for this lineshape. Second derivative lineshape usually stems from field-induced change in dipole moment, which in

the case of PBDB-T:IT-4F, may come from two sources. A secondary exciton may exist in pure small non-fullerene acceptors films.[23,24] NFAs with IT-unit core tend to have high crystallinity and can thus form small aggregates that generate a secondary exciton with more charge-transfer character. It has been argued that in polymer films, aggregates of chains with the highest excess polarizability, give the largest EA response.[11] EA response from the secondary exciton in IT-4F may thus lead to a second derivative lineshape (see Appendix C Figure S4 for EA spectrum of pure IT-4F sample). Another species that may give rise to the observed lineshape is CT state formed at the interface of PBDB-T and IT-4F, which has greater electron-hole separation and thus more polarity (a non-zero $\Delta\mu$). Furthermore, it seems that the EA lineshape cannot be adequately described by Liptay formulism (Appendix C Figure S5). A residue centered around 1.55eV with a Gaussian shape remains. It is possible that a new absorption becomes accessible due to electric field perturbation. Theory calculations will provide a clearer picture for the energetics in a heterogeneous blend film such as the blend here.

Regardless of ambiguous interpretation of the measured EA spectrum, it is interesting to see that species with CT character, whether a secondary exciton in IT-4F or CT state formed at donor/acceptor interface, contribute substantially to the EA low energy region and lead to second derivative lineshape.

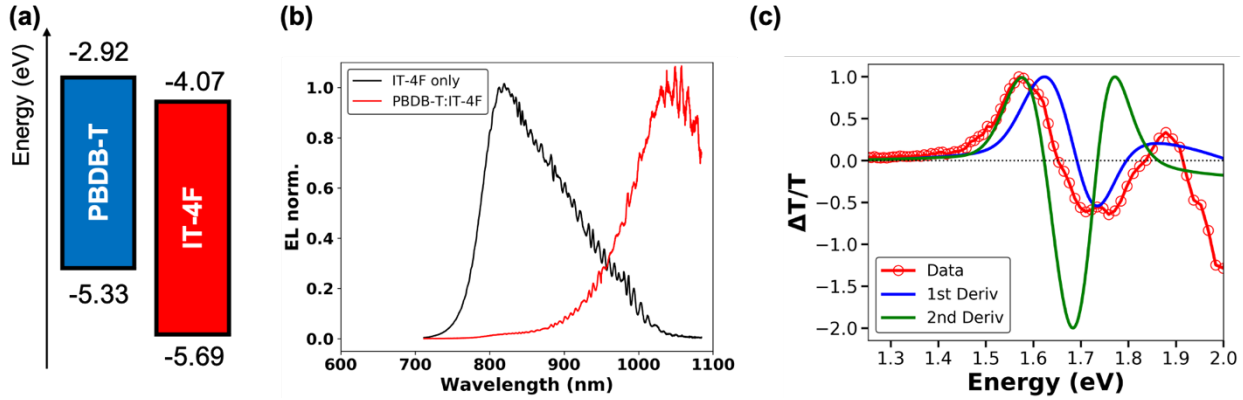

Figure 4.2 (a) Energy levels of PBDB-T and IT-4F. **(b)** Normalized EL emission spectra of pure IT-4F and PBDB-T:IT-4F blend devices. **(c)** Electroabsorption spectrum of PBDB-T:IT-4F and first and second derivatives of imaginary refractive index k.

3. PTO2:Y6 blend

Finally, we study a model system that is known to have CT-LE mixing, namely PTO2 as donor mixed with Y6 as small molecule acceptor. The energetic offsets of LE and CT in PTO2:Y6 blend is estimated to be ~50 meV (**Figure 4.3a**). This blend shows an outstanding ELQE of 0.08% and low ΔV_{nr} of 0.18 V, which is credited to intensity borrowing via CT-LE mixing.[25]

Figure 4.3b shows that the low energy EA lineshape clearly deviates from the derivative lineshape. We suspect that CT-LE mixing may be the reason for this. As a reminder, field-induced absorption shift may come from three contribution: Stark effect, redistribution of oscillator strength among nearby state, and new absorption feature due to symmetry breaking. If there is existing mixing

between CT and LE even in the absence of an electric field, the EA response from LE exciton is likely to deviate from derivative shapes.

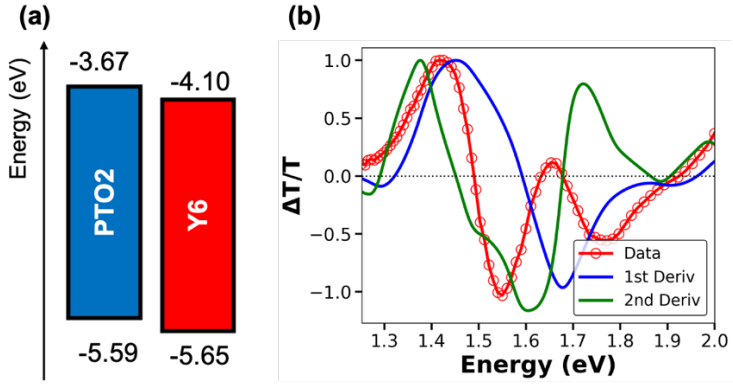

Figure 4.3 (a) Energy levels of PTO2 and Y6. **(b)** Electroabsorption spectrum of PTO2:Y6 and first and second derivatives of imaginary refractive index k.

4.4 Future direction

We have shown that EA response in a heterogeneous sample is very sensitive to the nature of photoexcited states and their interaction among these states. To fully understand if and how CT-LE mixing influences the blend's field-induced absorption, we would like to design a series of polymer/NFA blends, where we vary $\Delta E_{CT\text{-}LE}$ by gradually tuning the HOMO energy of the donor relative to the acceptor's HOMO. Then, we would like to compare the blend's EA lineshape in the low energy region. Qualitatively, we expect stronger second-derivative shape as $\Delta E_{CT\text{-}LE}$ decreases and new absorption feature that is not accounted for by the Liptay equation. To fully understand energetics reflected in EA spectrum, we propose to couple theoretical calculation with experimental measurements such as sum-of-state calculation[11,12] and molecular dynamics calculation.[6] The latter has previously used to predict absorption spectrum of polymer/NFA blend where CT-LE mixing is significant.

Appendix C

Experimental method and supplementary information for Chapter 4.

Acknowledgment

We would like to thank Dr. Mark Ziffer and Dr. Xiankai Chen for valuable discussions. This work is supported by the Office of Naval Research through grant number N00014-17-1-2201. Ellipsometry measurements were conducted at the Molecular Analysis Facility, a National Nanotechnology Coordinated Infrastructure site at the University of Washington, which is supported in part by the National Science Foundation (grant ECC-1542101), the University of Washington, the Molecular Engineering & Sciences Institute, the Clean Energy Institute, and the National Institutes of Health.

References

(1) NREL. National Renewable Energy Laboratory Research Cell Efficiency Chart https://www.nrel.gov/pv/cell-efficiency.html (accessed Mar 2, 2021).

(2) Liu, S.; Yuan, J.; Deng, W.; Luo, M.; Xie, Y.; Liang, Q.; Zou, Y.; He, Z.; Wu, H.; Cao, Y. High-Efficiency Organic Solar Cells with Low Non-Radiative Recombination Loss and Low Energetic Disorder. *Nat. Photonics* **2020**. https://doi.org/10.1038/s41566-019-0573-5.

(3) Eisner, F. D.; Azzouzi, M.; Fei, Z.; Hou, X.; Anthopoulos, T. D.; Dennis, T. J. S.; Heeney, M.; Nelson, J. Hybridization of Local Exciton and Charge-Transfer States Reduces Nonradiative Voltage Losses in Organic Solar Cells. *J Am Chem Soc* **2019**, *141*, 6362–6374. https://doi.org/10.1021/jacs.9b01465.

(4) Qian, D.; Zheng, Z.; Yao, H.; Tress, W.; Hopper, T. R.; Chen, S.; Li, S.; Liu, J.; Chen, S.; Zhang, J.; Liu, X.; Gao, B.; Ouyang, L.; Jin, Y.; Pozina, G.; Buyanova, I. A.; Chen, W. M.; Inganäs, O.; Coropceanu, V.; Bredas, J.; Yan, H.; Hou, J.; Zhang, F.; Bakulin, A. A.; Gao, F. Design Rules for Minimizing Voltage Losses in High-Efficiency Organic Solar Cells. *Nat. Mater.* **2018**, *17*. https://doi.org/10.1038/s41563-018-0128-z.

(5) Ziffer, M. E.; Jo, S. B.; Zhong, H.; Ye, L.; Liu, H.; Lin, F.; Zhang, J.; Li, X.; Ade, H. W.; Jen, A. K.-Y.; Ginger, D. S. Long-Lived, Non-Geminate, Radiative Recombination of Photogenerated Charges in a Polymer:Small-Molecule Acceptor Photovoltaic Blend. *J. Am. Chem. Soc.* **2018**, *140* (31), 9996–10008. https://doi.org/10.1021/jacs.8b05834.

(6) Chen, X. K.; Coropceanu, V.; Bredas, J. L. Assessing the Nature of the Charge-Transfer Electronic States in Organic Solar Cells. *Nat. Commun.* **2018**, *9*. https://doi.org/Artn 5295 10.1038/S41467-018-07707-8.

(7) Bublitz, G. U.; Boxer, S. G. Stark Spectroscopy: Applications in Chemistry, Biology, and Materials Science. *Annu. Rev. Phys. Chem.* **1997**, *48* (1), 213–242. https://doi.org/10.1146/annurev.physchem.48.1.213.

(8) Oh, D. H.; Sano, M.; Boxer, S. G. Electroabsorption (Stark Effect) Spectroscopy of Mono- and Biruthenium Charge-Transfer Complexes: Measurements of Changes in Dipole Moments and Other Electrooptic Properties. *J. Am. Chem. Soc.* **1991**, *113* (18), 6880–6890. https://doi.org/10.1021/ja00018a026.

(9) Weiser, G.; Sebastian, L.; Physikalische, F. Charge Transfer Transitions in Solid Tetracene and Pentacene Studied by Electroabsorption. *Chem. Phys.* **1981**, *61*, 125–135.

(10) Ziffer, M. E.; Jo, S. B.; Liu, Y.; Zhong, H.; Mohammed, J. C.; Harrison, J. S.; Jen, A. K. Y.; Ginger, D. S. Tuning H-and J-Aggregate Behavior in φ-Conjugated Polymers via Noncovalent Interactions. *J. Phys. Chem. C* **2018**. https://doi.org/10.1021/acs.jpcc.8b05505.

(11) Liess, M.; Jeglinski, S.; Vardeny, Z.; Ozaki, M.; Yoshino, K. Electroabsorption Spectroscopy of Luminescent and Nonluminescent π-Conjugated Polymers. *Phys. Rev. B - Condens. Matter Mater. Phys.* **1997**, *56* (24), 15712–15724. https://doi.org/10.1103/PhysRevB.56.15712.

(12) Saito, K.; Yanagi, K.; Cogdell, R. J.; Hashimoto, H. A Comparison of the Liptay Theory of Electroabsorption Spectroscopy with the Sum-over-State Model and Its Modification for the Degenerate Case. *J. Chem. Phys.* **2011**, *134* (4). https://doi.org/10.1063/1.3524339.

(13) Feller, F.; Monkman, A. P. Electroabsorption Studies of Poly(2, 5-Pyridinediyl). *Phys. Rev. B - Condens. Matter Mater. Phys.* **1999**, *60* (11), 8111–8116. https://doi.org/10.1103/PhysRevB.60.8111.

(14) Pereira, D. D. S.; Menelaou, C.; Danos, A.; Marian, C.; Monkman, A. P. Electroabsorption Spectroscopy as a Tool for Probing Charge Transfer and State Mixing in Thermally Activated Delayed Fluorescence Emitters. *J. Phys. Chem. Lett.* **2019**, *10*, 3205–3211. https://doi.org/10.1021/acs.jpclett.9b00999.

(15) Liess, M.; Jeglinski, S.; Vardeny, Z.; Ozaki, M.; Yoshino, K. Electroabsorption Spectroscopy of Luminescent and Nonluminescent π-Conjugated Polymers. *Phys. Rev. B - Condens. Matter Mater. Phys.* **1997**, *56* (24), 15712–15724. https://doi.org/10.1103/PhysRevB.56.15712.

(16) Novoderezhkin, V. I.; Dekker, J. P.; Van Grondelley, R. Mixing of Exciton and Charge-Transfer States in Photosystem II Reaction Centers: Modeling of Stark Spectra with Modified Redfield Theory. *Biophys. J.* **2007**, *93* (4), 1293–1311. https://doi.org/10.1529/biophysj.106.096867.

(17) Ziffer, M. E.; Mohammed, J. C.; Ginger, D. S. Electroabsorption Spectroscopy Measurements of the Exciton Binding Energy, Electron-Hole Reduced Effective Mass, and Band Gap in the Perovskite CH3NH3PbI3. *ACS Photonics* **2016**, *3* (6), 1060–1068. https://doi.org/10.1021/acsphotonics.6b00139.

(18) Ziffer, M. E.; Jo, S. B.; Liu, Y.; Zhong, H.; Mohammed, J. C.; Harrison, J. S.; Jen, A. K. Y.; Ginger, D. S. Tuning H-and J-Aggregate Behavior in φ-Conjugated Polymers via Noncovalent Interactions. *J. Phys. Chem. C* **2018**, *122* (33), 18860–18869. https://doi.org/10.1021/acs.jpcc.8b05505.

(19) Byrnes, S. J. Multilayer Optical Calculations. *arXiv 1603 . 02720v3* **2018**, 1–20.

(20) Ziffer, M. E.; Jo, S. B.; Liu, Y.; Zhong, H. L.; Mohammed, J. C.; Harrison, J. S.; Jen, A. K. Y.; Ginger, D. S. Tuning H- and J-Aggregate Behavior in, Pi-Conjugated Polymers via Noncovalent Interactions. *J. Phys. Chem. C* **2018**, *122*, 18860–18869. https://doi.org/10.1021/acs.jpcc.8b05505.

(21) Liu, T.; Foo, Y.; Zapien, J. A.; Li, M.; Tsang, S. A Generalized Stark Effect Electromodulation Model for Extracting Excitonic Properties in Organic Semiconductors. *Nat. Commun.* **2019**, *10*, 5089. https://doi.org/10.1038/s41467-019-13081-w.

(22) Zhao, W.; Li, S.; Yao, H.; Zhang, S.; Zhang, Y.; Yang, B.; Hou, J. Molecular Optimization Enables over 13% Efficiency in Organic Solar Cells. *J. Am. Chem. Soc.* **2017**, *139* (21), 7148–7151. https://doi.org/10.1021/jacs.7b02677.

(23) Liu, Y.; Zuo, L. J.; Shi, X. L.; Jen, A. K. Y.; Ginger, D. S. Unexpectedly Slow Yet Efficient Picosecond to Nanosecond Photoinduced Hole-Transfer Occurs in a Polymer/Nonfullerene Acceptor Organic Photovoltaic Blend. *Acs Energy Lett.* **2018**, *3*, 2396–2403. https://doi.org/10.1021/acsenergylett.8b01416.

(24) Zhang, G.; Chen, X. K.; Xiao, J.; Chow, P. C. Y.; Ren, M.; Kupgan, G.; Jiao, X.; Chan, C. C. S.; Du, X.; Xia, R.; Chen, Z.; Yuan, J.; Zhang, Y.; Zhang, S.; Liu, Y.; Zou, Y.; Yan, H.; Wong, K. S.; Coropceanu, V.; Li, N.; Brabec, C. J.; Bredas, J. L.; Yip, H. L.; Cao, Y. Delocalization of Exciton and Electron Wavefunction in Non-Fullerene Acceptor

Molecules Enables Efficient Organic Solar Cells. *Nat. Commun.* **2020**, *11* (1), 1–10. https://doi.org/10.1038/s41467-020-17867-1.

(25) *Unpublished Manuscript*.

Appendix A. Supporting Information for Chapter 2

Experimental Method

Device fabrication and characterization 4TIC was synthesized as previously reported[46] and PDCBT was purchased from 1-Material Inc. The device structure of optimized PDCBT/4TIC solar cells is: ITO/PEDOT:PSS/PDCBT:4TIC (1:2, wt/wt)/bis-C_{60}/silver. ITO substrates were pre-etched, cleaned via sonication in micro-90 detergent, deionized water, acetone, and isopropanol solution, and plasma cleaned with O_2 for 5 min prior to spin-coating. PEDOT:PSS was spin-coated at 4000 rpm for 30 s, followed by annealing at 150°C for 15 min. The donor and acceptor materials were dissolved in a donor/acceptor ratio of 1:2 by weight and a total concentration of 12 mg/ml in anhydrous *o*-chlorobenzene in N_2 glove box and the solution was kept stirring at ~75°C overnight. The solution was spin-coated at 2000 rpm for 1 min and the film was annealed at 150°C for 5 min. Bis-C_{60} solution (in methanol, 4 mg/ml) was then spin-coated at 3000 rpm for 1 min. A 100 nm thick layer of Ag was evaporated under high vacuum ($<1\times10^{-6}$ Torr). PDCBT/4TIC films used in spectroscopy experiments were prepared using the same procedure described above. Pristine 4TIC and PDCBT films were casted in *o*-chlorobenzene and spin-coated on clean glass substrates at 1600 rpm for 1 min.

For external quantum efficiency measurement, excitation light was produced by a monochromated Tungsten-Halogen lamp and was modulated at 220 Hz using a Stanford Research Systems SR450 Chopper Controller. Photocurrent was detected by a Stanford Research Systems SR830 Lock-in Amplifier referenced to the chopper controller. External quantum efficiency was calculated using a calibrated photodiode. The irradiation area on the pixel was 0.013 cm^2.

The current density-voltage curve was measured with a Keithley 2400 source meter under AM 1.5G illumination. The photocurrent was calibrated with an IR photodiode. The irradiation area on the pixel was 0.013 cm^2.

Transient absorption spectroscopy Samples used in TA experiments were prepared using the protocol described above and were epoxy-sealed in N_2 glovebox. The pump pulse was generated via Coherent Inc./Light Source OPerA optical parametric amplifier from a fraction of the output (800 nm, 50 fs, 1 kHz) of a Coherent Libra Ti:Sapphire amplifier. The other fraction of the amplifier output was focused onto CaF_2 or sapphire crystals to generate supercontinuum probe pulse. The probe beam was spectrally aligned with the pump on the sample. The encapsulated sample was irradiated with 810 nm laser pulse. We used a variable short-pass filter and an 800 nm cut-on filter to obtain a narrow laser profile centered at 810 nm. Laser beam profile was measured at the sample position using a Thorlabs CCD camera beam profiler (BC106N-VIS) to ensure the irradiation had a Gaussian profile and to calculate the irradiation area. The pump excitation fluence per pulse was calculated based on average power measured with the Coherent FieldMater laser power meter, the beam diameter obtained from the Thorlabs beam profiler software (~0.7 mm, $1/e^2$ cut-off), and pulse frequency. Signals were detected using a CMOS and an InGaAs fiber optics-coupled photodiode array spectrometer. The pump-probe delay up to 5.6 ns was set using a mechanical translational stage. Data was taken in random order of pump-probe delay to avoid influence of laser power fluctuation during scan and was collected using the HELIOS software. The IRF of the TA set-up was measured using a thin glass substrate. The kinetics profiles at several

wavelengths were fit to the Gaussian function and its first- and second-order derivatives to obtain the true time-zero (t_0) and pulse-width (t_p) (**Equation S1**).

$$Signal(t) = \exp\left[-\left(\frac{t-t_0}{t_p/2\sqrt{ln2}}\right)^2\right] \times (A + Bt + Ct^2) \quad \textbf{(S1)}$$

Time-resolved photoluminescence Time-resolved PL spectra were collected using a Hamamatsu streak camera with a synchroscan unit. The same samples used in TA measurement were irradiated with 810 nm pulse pumped at 1 kHz from a Coherent Inc./Light Source OPerA optical parametric amplifier. The IRF of the tr-PL set-up was measured with a sanded-glass sample in the same optical geometry as the sample measurements.

Steady-state PL spectroscopy Steady-state PL measurement was performed on a home-built set-up. A 660 nm diode-pumped solid-state laser was used for excitation. The sample was mounted in cryostat with liquid N_2 as the cryogenic gas and the temperature was controlled with a digital temperature controller. PL emission was focused onto the detector via a combination of two lenses. A 700 nm (cut-on) filter was used in front of the detector to block the scattered laser excitation. Signal was detected by fiber-coupled OceanOptics USB2000+ CCD spectrometer. The spectral response of the detector was corrected with the spectrum of a calibrated white-light source taken in the same optical geometry as PL measurements of the sample.

Electrochemical measurements Samples were prepared by spin-coating 4TIC or PDCBT on clean FTO substrates dried overnight with molecular sieves and were immersed in 0.1 M tetrabutylammonium hexafluorophosphate in anhydrous acetonitrile. FTO, Ag/AgCl and Pt wire were used as the working, reference and counter electrode, respectively. CV measurements were performed using a scan rate of 0.1 V/s. The change in absorption was recorded when a negative or positive voltage was applied to the sample.

Supplemental Information

Section 1. Driving force for hole-transfer

We used the method reported by Ren *et al*. to calculate the driving force for hole-transfer.[47] Rigorously, the hole-transfer driving force should equal to the free energy difference between the acceptor exciton and the donor/acceptor CT state. Based on this method, the driving force for photoinduced hole transfer from an excited electron acceptor to a ground state electron donor is approximated as the enthalpy energy difference between the electron affinity of the acceptor *exciton* and the ionization potential (IP) of the ground state donor (**Equation S2&3**) Nevertheless, this definition has been shown to be more appropriate than the common oversimplification of estimating driving force by taking the difference between the ground state IEs (or EAs) of the donor and acceptor molecules to calculate the driving energy for hole- (or electron-) transfer.[47,48]

$$\Delta E_{hole-transfer} = EA_{M*/M-}[Acceptor] - IP_{M/M+}[Donor] \quad \textbf{(S2)}$$

$$EA_{M*/M-} = EA_{M/M-} - E_g^{opt} \quad \textbf{(S3)}$$

Based on cyclic voltammetry data, we determined $IP_{M/M+}$[Donor] = -5.49 eV and $EA_{M/M-}$[Acceptor] = -3.82 eV. The value for E_g^{opt} is determined to be ~1.59 eV based on the red absorption peak. Thus, the driving force for hole-transfer from 4TIC exciton to the PDCBT polymer is ~-80 meV.

Section 2. Excitation density calculation

To ensure our spectroscopy studies are carried out in the excitation density regime relevant to the working condition of OPV devices under AM 1.5G illumination, we calculate the excitation density based on **Equation S4&5**. We used 810 nm excitation at a fluence of ~2.5 μJ/cm^2/pulse on ~80 nm-thick PDCBT/4TIC blend, pristine 4TIC, and pristine PDCBT films.

$$Excitation\ density = \frac{number\ of\ absorbed\ photons}{film\ thickness \times excitation\ area} \quad \textbf{(S4)}$$

$$Number\ of\ absorbed\ photons = \frac{fluence \times (1-10^{-OD})}{photon\ energy} \quad \textbf{(S5)}$$

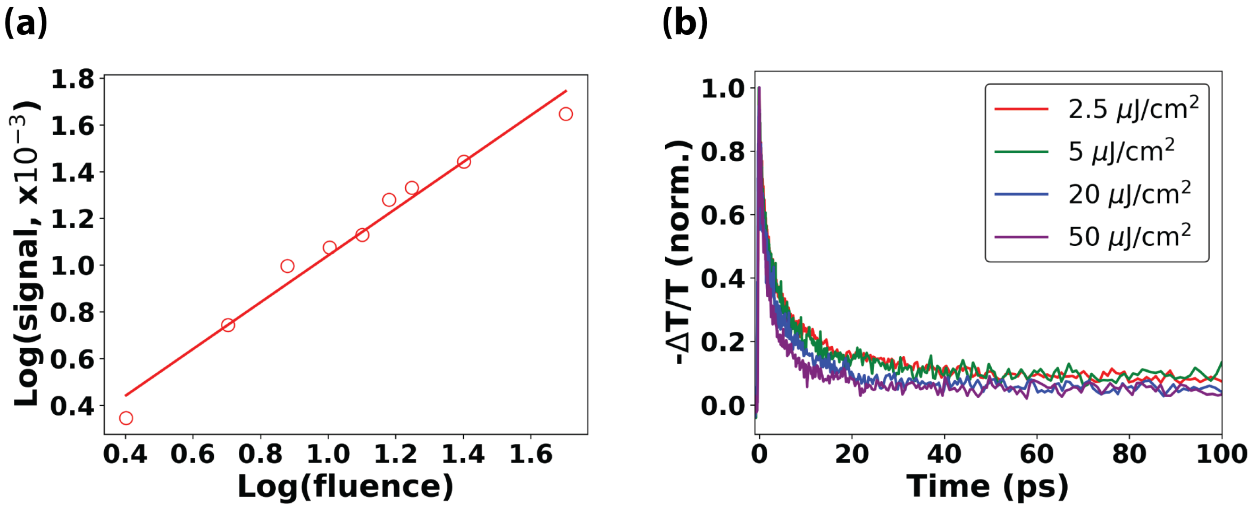

Figure S1. (a) Log-log plot of the 4TIC exciton signal versus excitation fluence (μJ/cm^2/pulse) in PDCBT/4TIC blend films. The 4TIC exciton signal is recorded as the maximum signal upon photoexcitation fluence between 2.5 and 50 μJ/cm^2/pulse. Linear regression (red trace) is represented by $log(signal) = 1.00 \times log(fluence) + 0.04$. Slope of 1 indicates that two-photon absorption is absent in this fluence range. (b) Decay traces of 4TIC exciton (at 960 nm) at various excitation fluences. Exciton decay is dependent on excitation fluence as low as 5 μJ/cm^2/pulse, likely due to non-linear processes such as exciton-exciton annihilation and exciton-charge annihilation as well as exciton diffusion, which are normally concentration dependent. We therefore use 2.5 μJ/cm^2/pulse in our TA studies to avoid such non-linear kinetics. Excitation wavelength: 810 nm.

Section 3. TA experiments on pristine PDCBT films

To verify that we only photoexcited the 4TIC molecules in the polymer/NFA blend, we performed control TA experiments on pristine PDCBT films. We observe no bleach signal of the ground-state absorption when the pristine PDCBT film was photoexcited at 810 nm, the excitation wavelength we used in TA measurements of the blend system (**Figure S2**, red).

In addition, we photoexcited the pristine PDCBT film at 480 nm and observed a ground-state bleach signal. This spectrum is used as a reference spectrum along with the steady-state absorption spectrum of PDCBT to assign the PDCBT GSB signature observed in blend film's TA spectra (**Figure S2**, green).

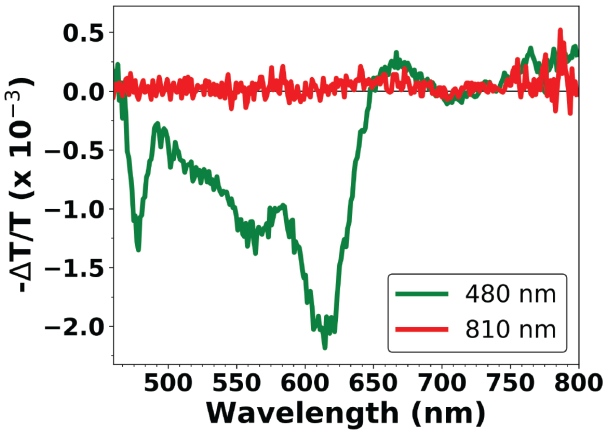

Figure S2 TA spectra of pristine PDCBT film using 480 nm (green) and 810 nm excitation (red). The peak at ~480 nm is the laser profile.

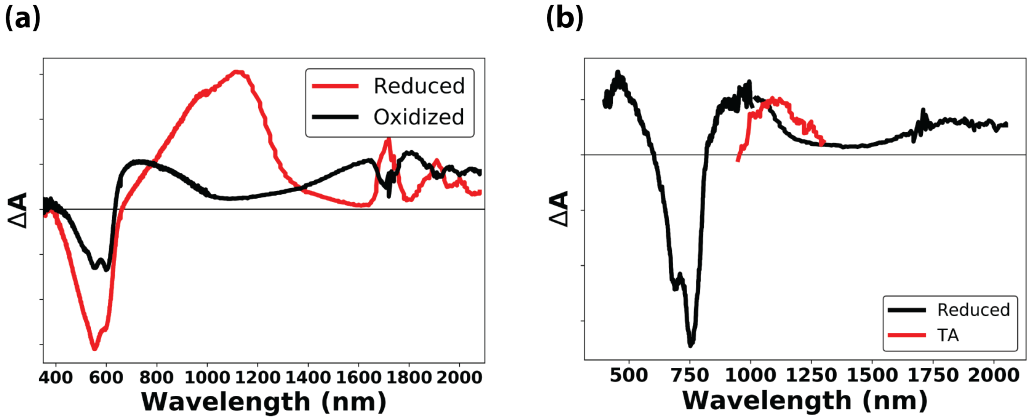

Figure S3. (a) ΔA spectra of PDCBT when reduced and oxidized electrochemically. (b) ΔA spectrum of 4TIC when oxidized electrochemically overlaid with the TA spectrum of the PIA feature centered at ~1100 nm.

Section 4. Spectral decomposition of nIR TA spectra

To obtain the kinetics of excitons and polaron-pair involved, we decompose the NIR TA spectra into representative spectra of exciton and charged species, using a method previously described by Rolczynski *et al*.[49] Since the exciton and charged-species signatures overlap in the NIR spectra, we used a linear combination of two Gaussian peaks to describe NIR spectra up to 200 ps by which time the 960 nm peak has completely vanished (**Figure S4**). The center wavelengths and widths of the Gaussian peaks are determined by fitting each Gaussian to a section of the selected NIR spectrum. In the global fitting procedure, only the intensities of the Gaussian functions are varied. **Figure S4(a) and (d)** show that the linear combination of two Gaussian functions does not fit the data perfectly. However, we rule out the possibility that a third species is hidden in the spectrum for the following reasons. First, the residue spectra at different pump-probe delay times are different (**Figure S4(b)**). Second, a three-Gaussian fit did not improve the fitting (**Figure S4(c)**).

In addition, we compare the kinetics of the two PIA features (centered at 960 nm and 1100 nm) before and after spectral decomposition. We find that in both blend and pristine 4TIC films, the overlapping of the PIA peaks does not skew the true kinetics revealed by spectral decomposition (**Figure S5**).

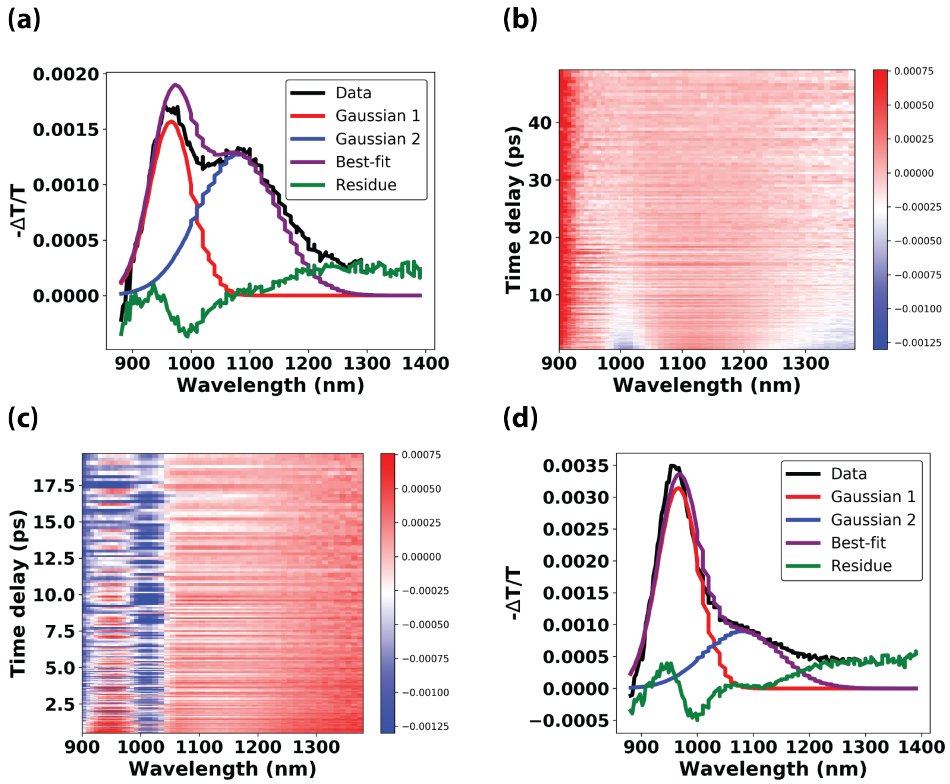

Figure S4. Spectral decomposition of the nIR spectra of pristine 4TIC **(a)** and blend **(d)** films into linear combination of two Gaussian functions. The intensities of the Gaussian functions are varied at each time-point and the sum of the Gaussians is fit globally to the data matrix. The residue is defined as the left-over signals after decomposition, i.e. the original data matrix - the best-fit matrix. **(c)** and **(d)** Contour plots of the residue matrices obtained after two-Gaussian **(c)** and three-Gaussian **(d)** decomposition are represented, repsectively.

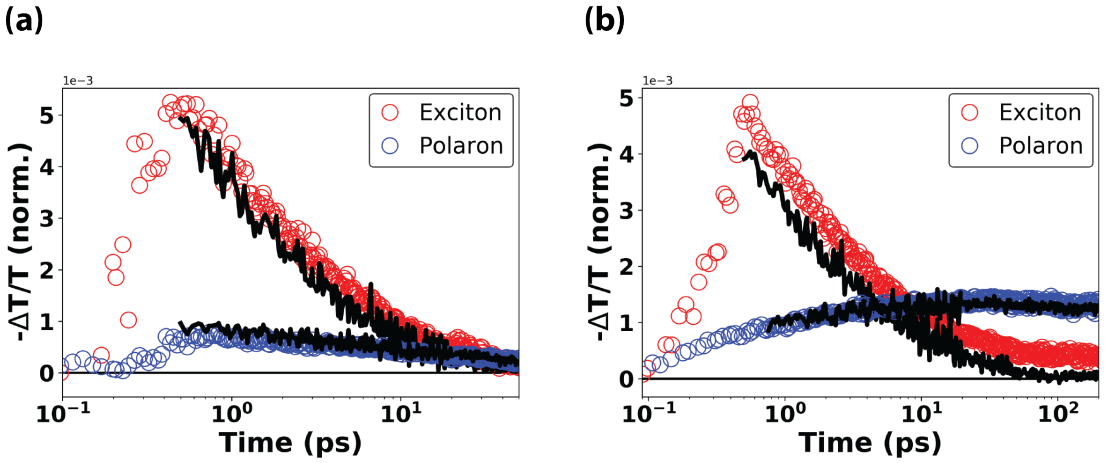

Figure S5. Comparison of exciton and polaron-pair kinetics before and after spectral de-composition **(a)** in pristine 4TIC and **(b)** in blend. Black traces represent kinetics obtained after de-composition.

Section 5. TA and time-resolved PL experiments on pristine 4TIC system

We investigate exciton dynamics in 4TIC in the absence of a donor via TA and time-resolved PL (tr-PL) spectroscopy. We use low excitation fluence of ~2.5 μJ/cm²/pulse to avoid non-linear photophysics and to keep the excitation density relevant to the working condition of a solar cell. **Figure S7(a)** shows the visible and nIR TA spectra of a pristine 4TIC film at selected pump-probe delay times after excitation at 810 nm. Upon photoexcitation, the 4TIC GSB appears immediately in the visible spectra. At 1 ps, a positive TA signal dominates the NIR spectrum. This signal consists of a peak at around 960 nm and a tail spanning throughout the rest of the NIR wavelengths. The peak at 960 nm decays quickly by 50 ps, whereas the tail evolves into a Gaussian-shape at later times and has a slow decay component. Based on these observations, we attribute this positive TA feature to a superposition of two PIA peaks centered at 960 nm and at 1100 nm, which are assigned to exciton and 4TIC polaron-pair signature (explained in detail in the next few paragraphs).

To obtain the true kinetics of the exciton and polaron-pair, we decompose the NIR spectrum (900–1400 nm) into a mixture of two Gaussian functions representing the ~960 nm and ~1100 nm features (details described in **Section 4** above, **Figure S4&5**). However, the kinetics of exciton and polaron features do not change appreciably after spectral decomposition (**Figure S6(a)**). **Figure S7(b)** shows the ps-ns kinetics of the GSB, the exciton and the polaron-pair. We obtain the decay rate of these species by re-convolution of multi-exponential decay functions with the Gaussian-shaped IRF of the laser system (~250 fs). The rate constants are shown in **Table S1**. The 4TIC exciton kinetics is well described by a sum of two exponential components. A majority of excitons are quenched with time constant of ~2 ps, and the rest decay with a lifetime of ~20 ps. The 4TIC polaron is generated within the instrument response time and decay with a sum of three mono-exponential rates: ~14 ps, ~150 ps, and longer than the nanosecond timescale. The long

lifetime of over 5 ns is typical for non-geminate recombination, suggesting that a fraction of polaron-pair may dissociate into free carriers.

Now we discuss assignment of the NIR TA spectral features. We assign the narrow TA feature around 960 nm to the 4TIC exciton absorption based on the following observations. TA experiments on 4TIC solution shows a photoinduced absorption feature centered at around 930 nm (**Figure S7(a)**). This TA feature has a similar spectral signature to the short-lived 960 nm feature in pristine 4TIC film. The small spectral shift of ~30 meV may be due to different delocalization and bandwidth of the exciton in solution and in film. In solution, the 930 nm PIA signal appears within the instrument-response limited rise-time and decayed mono-exponentially with a life-time of ~400 ps. These observations are expected for exciton kinetics. To check if the 930 nm feature is indeed from the absorption of the 4TIC exciton to higher energy levels, we monitor the PL emission of 4TIC solution using the same excitation wavelength and fluence as in TA. We find that PL emission decayed mono-exponentially with a lifetime of ~510 ps by convolving a mono-exponential function with the measured IRF. The matching lifetimes of PL emission and the TA feature verify that the 930 nm feature in solution and the 960 nm feature in film originate from 4TIC exciton absorption (**Figure S7(b)**).

Intriguingly, 4TIC film has a much longer PL emission compared to the 4TIC exciton decay in TA (**Figure S6(b)**, blue trace). Both tr-PL and TA experiments are performed using the same excitation wavelength and fluence. We determine the lifetime of PL to be ~40 ps by re-convolving a mono-exponential function with the measured IRF to fit the observed PL. Unexpectedly, this is significantly longer than the TA exciton feature's lifetime (fitting to a stretched exponential, we obtain an average life-time of 2.2 ps). Delayed fluorescence has been observed in neat polymer films and molecular crystals and attributed to the presence of interchain or charge-transfer like photoexcited species.[49,50] Specifically, these states can slowly return to the singlet exciton, which fluoresces at a much longer time-scale. Thus, we consider the possibility that a second photoexcited 4TIC species is generated, which then leads to delayed fluorescence via the exciton. Note that if the initial 4TIC excitons are regenerated from this second species, we will expect a slow decay component in the TA exciton feature. However, we are limited by the S/N ratio of our TA set-up and cannot resolve this slow decay component in exciton kinetics. Nevertheless, our kinetics data suggest that 4TIC polarons are generated on the ultrafast scale in pristine 4TIC films and regenerate the 4TIC excitons at a much longer time-scale.

Furthermore, the positive signal centered at 1100 nm corroborates the presence of a secondary 4TIC excited state. First, we rule out the possibility of triplet excitons. This TA feature appears within the time resolution of the TA system (~250 fs), but triplet excitons are generated at longer time-scale. We monitor the change in absorption spectrum when 4TIC is reduced electrochemically. The ΔA spectrum is similar to the 1100 nm PIA (**Figure S3(b)**). Thus, the 1100 nm feature is likely due to absorption of charged 4TIC population, i.e. hole or electron polarons or polaron-pair. Polaron-pairs have been observed in co-polymers and described as Coulombically bound electron-hole pairs with charge-transfer character.[51–53] They have also been referred to as pseudo-charge transfer excitons[49] or spatially indirect excitons in molecular crystal.[54] Previous photoinduced absorption spectroscopy studies have shown that interchain polaron-pairs are created via exciton-exciton annihilation at high fluence while from singlet exciton dissociation at low fluence.[49,51,52,54,55] We hypothesize that 4TIC polaron-pairs and/or free polarons might be generated in the 4TIC film but not in solution, because in films, 4TIC molecules form aggregates, in which intermolecular interaction is favored. Indeed, compared to the absorption spectrum of 4TIC

solution, the solid-state 4TIC has a significantly red-shifted absorption spectrum (**Figure S8**). In addition, **Figure S9** shows that the ratio of 0-0 to 0-1 emission peak decreases as temperature increases from 80 K to 295 K, consistent with the temperature-dependent PL trend in J-aggregates observed in various neat polymer systems.[56,57] Furthermore, the interchain species is most likely to arise from singlet exciton dissociation within instrument response instead of exciton-exciton annihilation given that our excitation fluence (10^{17} molecules/cm^3) is much lower than the fluence required for exciton-exciton annihilation.[51,53]

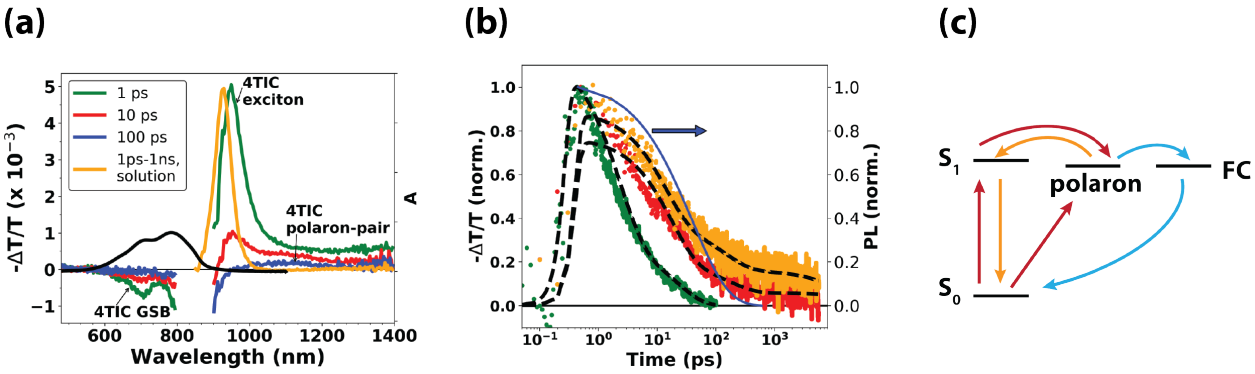

Figure S6. TA spectra of 4TIC film at selected pump-probe delays using 810 nm excitation at 2.5 μJ/cm^2 /pulse(red and green) and steady-state absorption of 4TIC (black). **(b)** Kinetics of GSB, exciton and polaron-pair. Dotted black lines indicate best-fit kinetics obtained by re-convolution of multi-exponential function with the Gaussian-shaped IRF of the TA set-up. Kinetics of excitons was characterized by a sum of two exponential, whereas GSB and polaron-pairs were fit to a sum of three exponentials. The rate constants are summarized in **Table S1**. **(c)** Proposed model for photophysics of the pristine 4TIC film. Red arrows denote generation pathways of 4TIC photoexcited species (4TIC excitons and 4TIC polaron-pairs), and orange represents fluorescence emission pathways. Two pools of 4TIC photoexcited species—excitons (S_1) and polaron-pairs—are generated within the instrument response time, of which excitons are emissive. A fraction of 4TIC excitons may also split into 4TIC polaron-pairs. Polaron-pairs may regenerate S_1, leading to delayed fluorescence, and may also dissociate into free carriers (FC) which non-geminately recombine to the ground-state.

Table S1. Kinetics parameters of multi-exponential functions that describe 4TIC exciton, 4TIC GSB and 4TIC polaron dynamics in pristine 4TIC films upon 810 nm photoexcitation.

	a_1	τ_1 (ps)	a_2	τ_2 (ps)	a_3	τ_3 (ps)
4TIC exciton	0.75	2.3	0.25	23	N/A	N/A
4TIC GSB	0.74	17	0.18	170	0.08	>5000
4TIC polaron	0.57	14	0.24	150	0.18	>5000

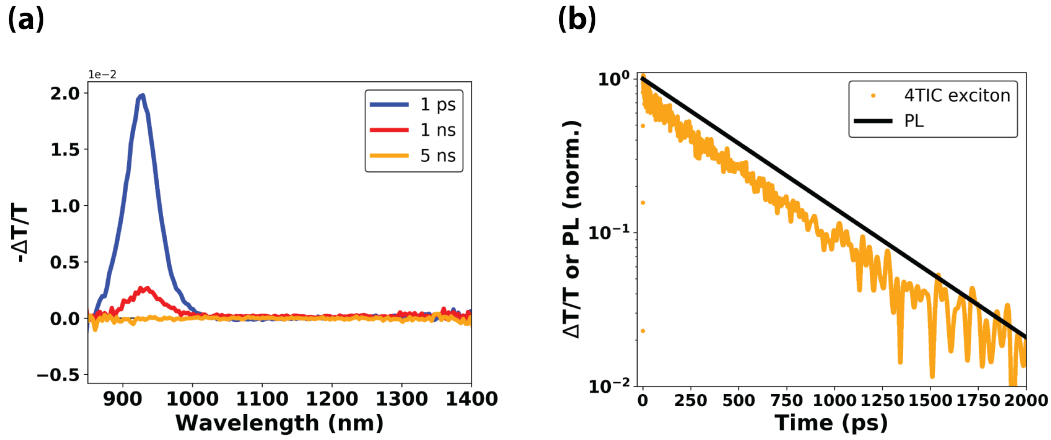

Figure S7. (a) TA spectra of 4TIC solution at selected times. Contrary to 4TIC films, only one PIA feature appears in the nIR wavelengths. (b) Comparison of 4TIC PL decay with exciton decay upon photoexcitation at 810 nm with fluence of 2.5 μJ/cm^2/pulse. Kinetic traces of PL emission and the TA signal at 930 nm were fit to mono-exponential functions re-convolved with the measured IRFs of the trPL and TA set-ups. We determine the exciton mono-exponential 1/e lifetimes of PL emission and the exciton TA feature are 480 ps and 504 ps, respectively.

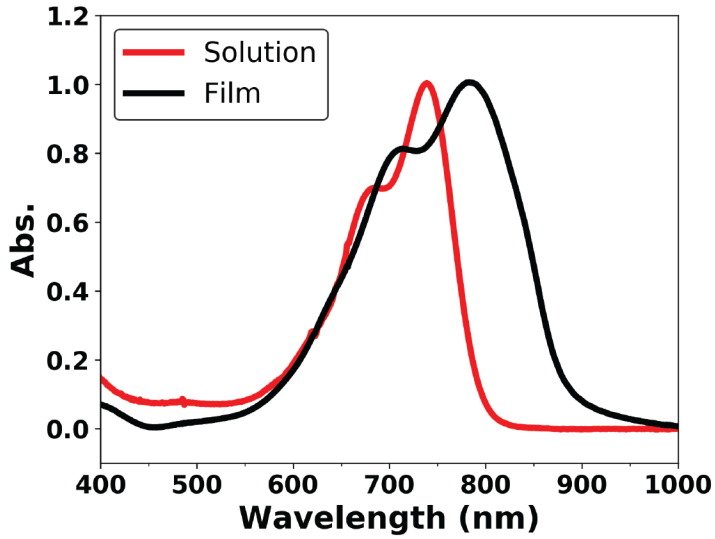

Figure S8 Absorption spectra of pristine 4TIC film and solution. Red-shift of the absorption bands in film suggests aggregate formation, leading to intermolecular interaction between 4TIC molecules.

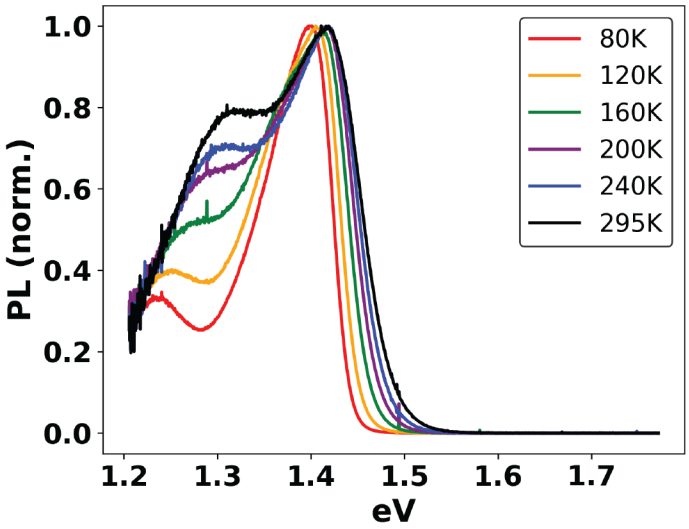

Figure S9 Temperature-dependent steady-state photoluminescence spectra of pristine 4TIC film. We assign the peak at ~1.25-1.3 eV as the 0-1 transition and the peak at ~1.4 eV as the 0-0 transition. PL emission is normalized to the red peak ~1.4 eV to monitor the ratio of 0-0 to 0-1 transition at varying temperature.

References

(1) Shi, X.; Zuo, L.; Jo, S. B.; Gao, K.; Lin, F.; Liu, F.; Jen, A. K. Y. Design of a Highly Crystalline Low-Band Gap Fused-Ring Electron Acceptor for High-Efficiency Solar Cells with Low Energy Loss. *Chem. Mater.* **2017**, *29* (19), 8369–8376.

(2) Ren, G.; Schlenker, C. W.; Ahmed, E.; Subramaniyan, S.; Olthof, S.; Kahn, A.; Ginger, D. S.; Jenekhe, S. A. Photoinduced Hole Transfer Becomes Suppressed with Diminished Driving Force in Polymer-Fullerene Solar Cells While Electron Transfer Remains Active. *Adv. Funct. Mater.* **2013**, *23* (10), 1238–1249.

(3) Zhu, X. Y. How to Draw Energy Level Diagrams in Excitonic Solar Cells. *J. Phys. Chem. Lett.* **2014**, *5* (13), 2283–2288.

(4) Rolczynski, B. S.; Szarko, J. M.; Son, H. J.; Liang, Y.; Yu, L.; Chen, L. X. Ultrafast Intramolecular Exciton Splitting Dynamics in Isolated Low-Band-Gap Polymers and Their Implications in Photovoltaic Materials Design. *J. Am. Chem. Soc.* **2012**, *134* (9), 4142–4152.

(5) Glowe, J. F.; Perrin, M.; Beljonne, D.; Hayes, S. C.; Gardebien, F.; Silva, C. Charge-Transfer Excitons in Strongly Coupled Organic Semiconductors. *Phys. Rev. B - Condens. Matter Mater. Phys.* **2010**, *81* (4), 1–4.

(6) Klimov, V. I.; McBranch, D. W.; Barashkov, N. N.; Ferraris, J. P. Femtosecond Dynamics of Excitons in π-Conjugated Oligomers: The Role of Intrachain Two-Exciton States in the

Formation of Interchain Species. *Chem. Phys. Lett.* **1997**, *277* (1), 109–117.

(7) King, S. M.; Hintschich, S. I.; Dai, D.; Rothe, C.; Monkman, A. P. Spiroconjugation-Enhanced Intramolecular Charge-Transfer State Formation in a Polyspirobifluorene Homopolymer. *J. Phys. Chem. C* **2007**, *111* (50), 18759–18764.

(8) Kraabel, B.; Klimov, V.; Kohlman, R.; Xu, S.; Wang, H. L.; McBranch, D. Unified Picture of the Photoexcitations in Phenylene-Based Conjugated Polymers: Universal Spectral and Dynamical Features in Subpicosecond Transient Absorption. *Phys. Rev. B - Condens. Matter Mater. Phys.* **2000**, *61* (12), 8501–8515.

(9) Yan, M.; Rothberg, L. J.; Papadimitrakopoulos, F.; Galvin, M. E.; Miller, T. M. Spatially Indirect Excitons as Primary Photoexcitations in Conjugated Polymers. *Phys. Rev. Lett.* **1994**, *72* (7), 1104–1107.

(10) Westerling, M.; Aarnio, H.; Österbacka, R.; Stubb, H.; King, S. M.; Monkman, A. P.; Andersson, M. R.; Jespersen, K.; Kesti, T.; Yartsev, A.; et al. Photoexcitation Dynamics in an Alternating Polyfluorene Copolymer. *Phys. Rev. B - Condens. Matter Mater. Phys.* **2007**, *75* (22), 1–9.

(11) Clark, J.; Silva, C.; Friend, R. H.; Spano, F. C. Role of Intermolecular Coupling in the Photophysics of Disordered Organic Semiconductors: Aggregate Emission in Regioregular Polythiophene. *Phys. Rev. Lett.* **2007**, *98* (20), 1–4.

(12) Spano, F. C.; Silva, C. H- and J-Aggregate Behavior in Polymeric Semiconductors. *Annu. Rev. Phys. Chem.* **2014**, *65* (1), 477–500.

.

Appendix B. Supporting Information for Chapter 3

Experimental Method

Device fabrication and characterization The device structure of optimized m-MTDATA:3TPYMB solar cells is: ITO/PEDOT:PSS (50nm)/Meo-TPD (12nm)/m-MTDATA (10nm)/m-MTDATA:3TPYMB (1:1 by mass)/3TPYMB (10nm)/Bphen (10nm)/LiF (1nm)/Al (100nm). ITO substrates were pre-etched, cleaned via sonication in micro-90 detergent, deionized water, acetone, and isopropanol solution, and plasma cleaned with O_2 for 10 min prior to spin-coating. PEDOT:PSS was spin-coated at 4000 rpm for 40 s, followed by annealing at 150°C for 15 min. All following layers were deposited via thermal evaporation. For codeposition of m-MTDATA and 3TPYMB, the 1:1 mass ratio was achieved via controlling deposition rate.

For external quantum efficiency measurement, excitation light was produced by a monochromated Tungsten-Halogen lamp and was modulated at 220 Hz using a Stanford Research Systems SR450 Chopper Controller. Photocurrent was detected by a Stanford Research Systems SR830 Lock-in Amplifier referenced to the chopper controller. External quantum efficiency was calculated using a calibrated photodiode. Pixel mask was used to minimize edge effect, and the irradiation area on the pixel was ~0.06cm^2.

We performed variable angle spectroscopic ellipsometry (VASE) measurement to calculate the fraction of light absorbed by the m-MTDATA:3TPYMB layer in the device. VASE measures the change in polarization, both the amplitude ratio Ψ and the phase difference Δ, as light from various incidence angles reflects or transmits from the material. Spectra of Ψ and Δ were measured on m-MTDATA:3TPYMB blend co-deposited onto silicon substrates with 300 nm thermally grown SiO_2, at 3 different incidence angles (55°, 65° and 75°). The complex refractive indices n and k were modeled using a B-Spline model via the CompleteEASE software from J.A. Woollam Co. A transfer-matrix algorithm was used to calculate the fraction of light absorbed in each layer of the solar cell device.[1] To calculate IQE_{PV}, the EQE_{PV} spectrum was divided by the fraction of absorbed light in the m-MTDATA:3TPYMB layer.

The current density-voltage curve was measured with a Keithley 2400 source meter upon illumination of a 385nm LED on the same irradiation area as EQE measurement. The intensity of the LED illumination was corrected to AM1.5G 1-Sun intensity by spectrally matching to the solar spectrum.

EL spectrum was measured on the same m-MTDATA:3TPYMB device used for EQE and J-V measurement. The device was mounted inside a chamber under dynamic vacuum and was held at a constant bias (Keithley 2400) that corresponded to the short-circuit charge density at AM1.5G illumination. The electroluminescence was collected and focused into a spectrograph (MS-2300i, Princeton Instruments) using F/# matched optics and the spectra were measured using a LN2-cooled Si array CCD detector (Spec-10, Princeton Instruments). The spectra were corrected for the instrument response using a calibrated white light source (HL-P-CAL-EXT, Ocean Optics).

EL quantum yield was measured on a home-built set-up inside a N_2 glovebox. The device was mounted onto a holder inside a light-tight enclosure, with glass side facing a large area Si photodiode (Hamamatsu S3204-08). The holder was designed such that waveguided emission was blocked from the detector.

Photoluminescence characterization

PL decay kinetics of the blend film were measured using a Hamamatsu streak camera with a slow-scan unit. Samples used in trPL experiments were prepared on glass substrates using the protocol described above and were kept under dynamic vacuum during measurement. Film samples were irradiated with 365 nm pulse pumped at 1 kHz from a Coherent Inc./Light Source OPerA optical parametric amplifier. PL decay of the m-MTDATA and 3TPYMB solution (0.016M) was measured using a time-correlated single photon counting system (Picoharp 300) using a 375nm pulsed laser (PDL-800) as excitation source.

Steady-state PL measurement was performed on m-MTDATA:3TPYMB device on a home-built set-up. A 374 nm solid-state laser was used for excitation. The sample was mounted in a chamber and placed at a 45-degree angle from the laser beam path. The photoexcitation was focused onto one specific pixel from the glass side. PL emission was focused onto a fiber-coupled OceanOptics USB2000+ CCD spectrometer. A 500 nm (cut-on) filter was used in front of the detector to block the scattered laser excitation. The spectral response of the detector was corrected with the spectrum of a calibrated white-light source taken in the same optical geometry as PL measurements of the sample. Low-temperature PL spectrum was measured by mounting samples in a cryostat (Janis Research Co., STVP-100) with a temperature controller (Lakeshore 332).

PL quantum efficiency of m-MTDATA:3TPYMB thin film was measured with a Hamamatsu C9920-2 integrating sphere system. The film was photoexcited with 365nm beam generated from monochromated lamp. The excitation intensity and sample photoluminescence were simultaneously measured using a CCD spectrometer (Hamamatsu C10027). Three measurements were made (sample in the light path, sample out of the light path, and sample removed) and PLQY was calculated using the method of de Mello *et al*.[2] PL quantum efficiency of m-MTDATA and 3-TPYMB solution (0.016M) was measured in the same set-up.

Supplemental Information

Section S1 Calculation of kinetic rates

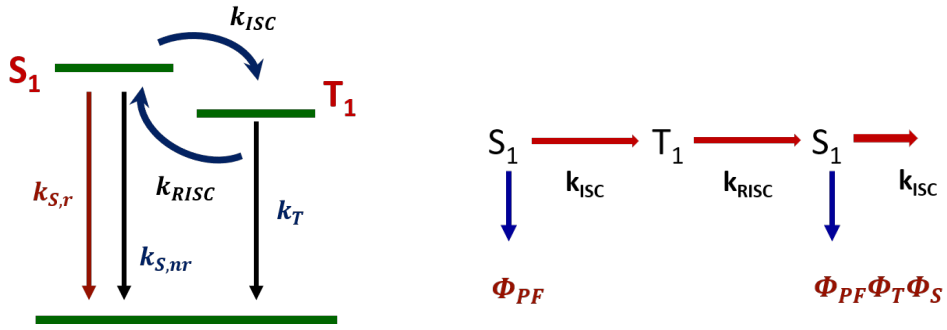

Kinetics of TADF-emissive states can be described via the scheme above.[3] To calculate parameters of our interest ($k_{s,r}$, $k_{s,nr}$, k_{ISC}), we can first write the prompt PL yield (Φ_{PF}), the triplet and singlet yields (Φ_T and Φ_S), and total PL yield (Φ_F) as

$$\Phi_{PF} = \frac{k_{s,r}}{k_{s,r}+k_{s,nr}+k_{ISC}} = k_{s,r}\tau_{PF} \quad (1)$$

$$\Phi_T = \frac{k_{ISC}}{k_{s,r}+k_{s,nr}+k_{ISC}} = k_{ISC}\tau_{PF} \quad (2)$$

$$\Phi_S = \frac{k_{RISC}}{k_{s,r}+k_{RISC}} \sim 1 \; assuming \; k_T \ll k_{RISC} \quad (3)$$

$$\Phi_F = \Phi_{PF} + \Phi_{DF} = \Phi_{PF} + \Phi_{PF}\Phi_T\Phi_S + \Phi_{PF}\Phi_S^2\Phi_T^2 + \Phi_{PF}\Phi_S^3\Phi_T^3 + \cdots \quad (4)$$

From (4), we obtain

$$\Phi_F = \frac{\Phi_{PF}}{1-\Phi_S\Phi_T} \quad (5)$$

$$\Phi_{DF} = \frac{\Phi_{PF}\Phi_S\Phi_T}{1-\Phi_S\Phi_T} \quad (6)$$

$$\frac{\Phi_{DF}}{\Phi_{PF}} = \frac{\Phi_S\Phi_T}{1-\Phi_S\Phi_T} \quad (7)$$

Substitution (3) and (2) into (7), we get

$$\frac{\Phi_{DF}}{\Phi_{PF}} = \frac{k_{ISC}\tau_{PF}}{1-k_{ISC}\tau_{PF}} \quad (8)$$

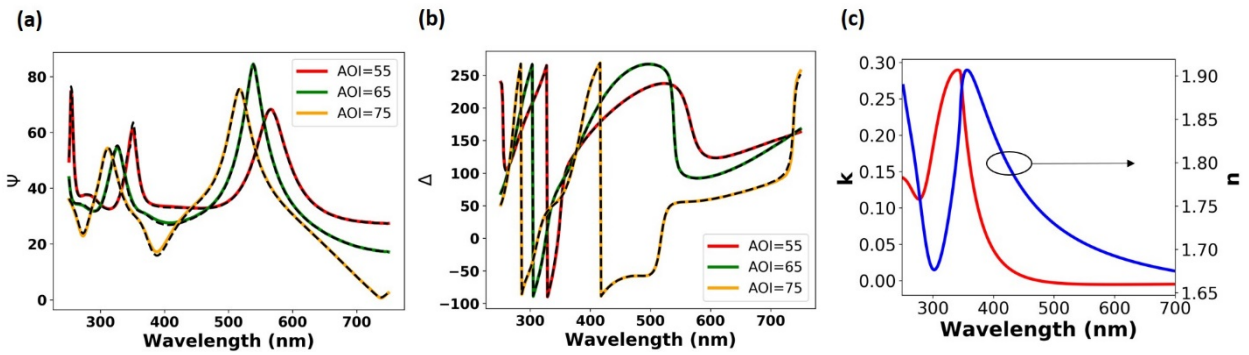

Figure S1 Fitting results of ellipsometry data of m-MTDATA:3-TPYMB blend: (a) Ψ and (b) Δ at three angles of incidence (AOI). Refractive indices n and k are shown in (c).

Section S2 Voltage loss analysis

The open circuit voltage loss can be separated into the following terms[4], based on the deviation of the actual short-circuit current J_{SC} and dark saturation current J_0 from their ideal values (J_{SC}^{SQ} and J_0^{SQ}) calculated based on the Shockley-Queisser limit[5] (Eqn. S1-3). V_{OC}^{SQ} is the ideal open-circuit voltage in the Shockley-Queisser limits, which assume EQE$_{PV}$ to be a step-function that equals unity above bandgap and zero below bandgap.[5] ΔV_{OC}^{SC} is the voltage loss due to a non-ideal charge generation.[6,7] At low photon energies, blackbody radiation spectrum increases in intensity, resulting in excess absorption by the solar cell and thus, based on Kirchhoff's radiation theorem, equivalent emission from the solar cell to the ambient. This absorption edge broadening results in additional radiative recombination and thus voltage loss, namely radiative recombination voltage loss (ΔV_{OC}^{r}).[6,7] The last loss term ΔV_{OC}^{nr} is due to non-radiative recombination of photogenerated charge recombination, and is thus determined by the electroluminescence efficiency (EQE_{EL})

$$V_{OC} = \frac{kT}{q}\ln\left(\frac{Jsc}{J_0}\right) \qquad \text{Eqn. S1}$$

$$V_{OC} = \frac{kT}{q}\ln\left(\frac{J_{SC}^{SQ}}{J_0^{SQ}} * \frac{Jsc}{J_{SC}^{SQ}} * \frac{J_0^{SQ}}{J_0^{rad}} * \frac{J_0^{rad}}{J_0}\right) \qquad \text{Eqn. S2}$$

$$V_{OC} = V_{OC}^{SQ} + \Delta V_{OC}^{SC} + \Delta V_{OC}^{r} + \Delta V_{OC}^{nr} \qquad \text{Eqn. S3}$$

We briefly explain the procedure for calculating each voltage term, as described in detail in previous work.[4,7]

1. V_{OC}^{SQ}: We first evaluate the bandgap (E_g) as the average of the probability distribution of E_g calculated from the first derivative of the EQE$_{PV}$ onset (Eqn. S4). We determine this value to be 3.239eV,[8] which corresponds to an ideal V_{OC} of 2.85V in the Shockley-Queisser limits at 295K.[5]

$E_g = \int_a^b E_g P(E_g) dE_g \,/\, \int_a^b P(E_g) dE_g$, where a and b are the FWHM limits of $P(E_g)$ Eqn. S4

2. ΔV_{OC}^{SC}: We evaluate the actual short-circuit current (J_{SC}) and the Shockley-Queisser J_{SC}^{SQ} via Eqn S5. For J_{SC}^{SQ}, EQE_{PV} is represented by a Heaviside function with onset at E_g. J_{SC} the experimental EQE_{PV} is used.

$$J_{SC} = q\int_{E_g}^{\infty} EQE_{PV}(E)\phi_{AM1.5}(E)dE \qquad \text{Eqn. S5}$$

3. ΔV_{OC}^{r}: We evaluate J_0^{SQ} and J_0^{rad} based on Eqn. S6. To calculate J_0^{SQ}, EQE_{PV} is represented by a Heaviside function with onset at E_g. For J_0^{rad}, the experimental EQE_{PV} spectrum was extended to lower energy region based on Rau's reciprocity theorem.[7,9] Within the framework of Rau's reciprocity theorem, EQE_{PV} and EL spectra are related via the blackbody radiation spectrum (Eqn. S7), because photogenerated free charges must radiatively recombine. First, we test reciprocity theorem by recreating the sub-gap tail of the EQE_{PV} spectrum with blackbody radiation spectrum at 295K and the EL spectrum measured at 1 Sun equivalent injection current condition. Figure 3c in main text shows that although the large shift of EL spectrum from absorption limits the overlapping wavelength range between EL onset and EQE_{PV} tail, recreated sub-gap EQE_{PV} tail follows the overall trend of the experimental EQE_{PV} spectrum and overlays well over the measured EQE_{PV} tail. Using the recreated EQE_{PV} spectrum, we then estimated the radiative saturation current and the radiative recombination loss given a non-step function absorption edge and obtain $\Delta V_{OC}^{r} = 0.600V$.

$$J_0 = q\int_0^{\infty} EQE_{PV}(E)\phi_{BB}(E)dE \qquad \text{Eqn. S6}$$

$$\phi_{EL}(E) = EQE_{PV}(E)\phi_{BB}(E)\left(\exp\left(\frac{qV}{kT}\right) - 1\right) \qquad \text{Eqn. S7}$$

4. ΔV_{OC}^{nr}: We determined EQE_{EL} of the solar cell device to be 1.67% at injection current equivalent to J_{SC} at AM1.5G illumination intensity. Based on Eqn. 2 in the main text, ΔV_{OC}^{nr} is thus 0.104V. Taken together, our voltage loss analysis leads to an estimated V_{OC} of 2.10V, agreeing quantitatively with our measured value of 2.11V (Table 1 in main text).

Section S3. PL spectra of m-MTDATA, 3TPYMB and m-MTDATA: 3TPYMB

The transition dipole moments are calculated using the equation below.[27] Parameters are obtained from PLQY, steady-state PL spectroscopy and PL lifetime measurements on m-MTDATA:3TPYMB blend film, dilute m-MTDATA and 3TPYMB solution samples. To determine the adiabatic energies the LE of single components, we found the intersection of normalized PL and absorption spectra (Figure S5).[28] The adiabatic CT energy is found via fitting EQE and EL spectra simultaneously to a set of Gaussian equation as described in detail in the next section.

$$k_{rad} = \frac{64\pi^4 E_{em}^3 d_{LE}^2}{3h^4 c^3} \quad \text{Eqn. S8}$$

d_{LE}: transition dipole moment from LE state to the ground state

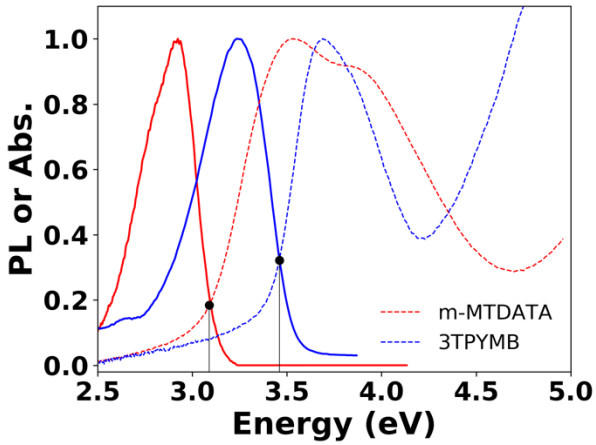

Figure S2 Normalized absorption and PL spectra of m-MTDATA and 3TPYMB.

Table S1. Summary of molecular and photoluminescence parameters.

	m-MTDATA	**3TPYMB**	**m-MTDATA:3TPYMB blend**
E_{em} **(eV)**	2.9	3.2	2.18
PLQY	0.109	0.067	0.128
τ_{mono} **(s)**	2.12×10^{-9}	1.04×10^{-9}	4.7×10^{-6} (prompt)
k_r **(s-1)**	5.14×10^{7}	6.44×10^{7}	2.72×10^{4}
k_{nr} **(s-1)**	4.2×10^{8}	8.97×10^{8}	1.86×10^{5}
$d_{LE\ or\ CT}$ (D)	**3.58**	**3.46**	**0.049**

Section S4. Marcus-Levich-Jortner framework

1. Theory background and derivation

In the Marcus-Levich-Jortner framework, radiative and non-radiative recombination of CT states can be described as a two-state electron-transfer event between CT and ground-state, under the assumption that the electronic coupling between CT and ground-state is much larger than that between CT and local exciton.

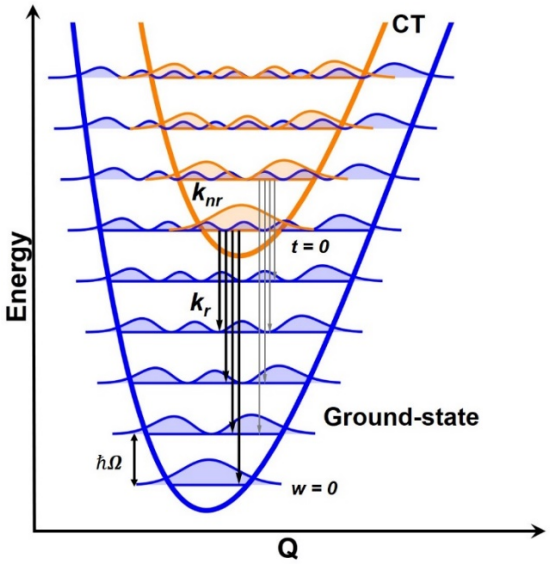

Figure S2. Potential energy surfaces of CT (orange) and ground-state (blue) with harmonic oscillator vibrational levels with quantum numbers of *t* and *w*, respectively. Vibronic wavefunctions are shown in color-shaded curves. Radiative transitions are indicated by the arrows and non-radiative transitions are shown as vibrational wavefunction overlap. Vibrational spacing is denoted as $\hbar\Omega$.

Within this framework, the non-radiative recombination rate is described by the well-known Marcus formula $k_{nr} = \frac{2\pi}{\hbar} V^2 \frac{1}{\sqrt{4\pi\lambda_{CT} k_B T}} \exp\left(-\frac{(E_{CT}-\lambda_{CT})^2}{4k_B T \lambda_{CT}}\right)$, where V^2 is the electronic coupling between ground-state and CT state, and λ_{CT} is the reorganization energy being the sum of *inter*molecular reorganization (reflecting structural rearrangements upon de-excitation of CT) and *intra*molecular reorganization due to vibrations of the molecule. In addition, intramolecular phonon modes must be treated quantum-mechanically, given that intramolecular phonon modes are "frozen" ($\hbar\omega_{intra}$~300-3000cm^{-1}) at room temperature and only intermolecular phonon modes ($\hbar\omega_{inter}$~10-100cm^{-1}) are activated.[10] Since $\hbar\omega_{inter} \ll k_B T \ll \hbar\omega_{intra}$, intramolecular phonon modes must be treated quantum-mechanically,[11,12] and thus, within the Born-Oppenheimer approximation and Fermi Golden Rule limits, the non-radiative transition rate can be written as

$$K_{nr} = \frac{2\pi}{\hbar} V^2 FCWD \quad \text{Eqn. S8}$$

where FCWD (Franck-Condon weighted density of states) factor accounts for transitions between all vibrational levels of CT and ground-states.

Here, Assuming CT and ground-state have equal intramolecular phonon modes ($\hbar\,\Omega$), it has been shown that the overlap integral squared between two vibronic states $\psi_{a\alpha}$ and $\psi_{b\beta}$ $< \psi_{a\alpha}|\psi_{b\beta} >^2$, describing the transition probability, reduces to $\frac{e^{-S}S^{w-t}t!}{w!}[L_t^{w-t}(S)]^2$,[13] S is the Huang-Rhys factor , $S = \frac{\lambda_{qm}}{\hbar\omega}$, where $\hbar$ is the intramolecular phonon mode energy, t and w are the vibrational quantum numbers for the ground-state and CT state, respectively, and $L_t^{w-t}(S)$ is the generalized Laguerre polynomial. The initial density of states at a particular vibrational level, t, of the CT state follows the Boltzmann distribution, and the density of population with energy required for the transition from the initial vibrational level of the CT state to the ground-state vibrational level, while satisfying energy conservation, is described as a delta function. At room temperature, we can safely only consider transitions from t=0 to all w vibrational levels. Taken together, we write FCWD for non-radiative transition rate as

$$FCWD(0) = \frac{1}{\sqrt{4\pi\lambda_c k_B T}} \sum_{w=0}^{\infty} \frac{e^{-S}S^{w}}{w!}[L_0^w(S)]^2 e^{\frac{-(\mathrm{E_{CT}}-\lambda_c-\mathrm{w}\hbar\Omega)^2}{4\lambda_c k_B T}} \quad \text{Eqn. S9}$$

where the factor before the double sum represents the classical density of states.

Radiative transition can be modeled as spontaneous emission with probability density of $< \psi_{a\alpha}|\vec{\mu}|\psi_{\beta\beta} >^2$. Using the MLJ approach, we then write the radiative rate constant at a particular photon energy $k_r(\hbar\omega)$ in units of $s^{-1}eV^{-1}$ as Eqn. S9 (Unit conversion is shown below) and integrate over photon energies to obtain the total radiative rate K_r (Eqn. S10). Based on generalized Mulliken-Hush approach, the transition dipole moment (M) is related to the electronic coupling (V) and change in dipole moment $\Delta\mu$.[6,14] Thus, the PLQY can be expressed as Eqn. S12. We use the full form of this equation since for high bandgap blends, such as the TADF-based blend herein, non-radiative and radiative rates may be kinetically competitive. ΔV_{OC}^{nr} is calculated via Eqn. 12, assuming the emission probability for CT state is 1.[6]

$$k_r(\hbar\omega) = \frac{1}{3\pi\epsilon_0\hbar^4}\left(\frac{\hbar\omega}{c}\right)^3 M^2 FCWD(\hbar\omega)\left[6.94\times10^{-41}\frac{C^2s^2kg^{-1}eV}{D^2}\right] \quad \text{Eqn. S10}$$

$$K_r = \int k_r(\hbar\omega)\, d\hbar\omega \quad \text{Eqn. S11}$$

$$PLQY = \frac{K_r}{K_r+K_{nr}} = \frac{\frac{1}{3\pi\epsilon_0\hbar^4}\left(\frac{1}{c}\right)^3\frac{V^2|\Delta\vec{\mu}|^2}{E_{CT}^2-4V^2}\int(\hbar\omega)^3 FCWD(\hbar\omega)\, d\hbar\omega\left[6.94\times10^{-41}\frac{C^2s^2kg^{-1}eV}{D^2}\right]}{\frac{1}{3\pi\epsilon_0\hbar^4}\left(\frac{1}{c}\right)^3\frac{V^2|\Delta\vec{\mu}|^2}{E_{CT}^2-4V^2}\int(\hbar\omega)^3 FCWD(\hbar\omega)\, d\hbar\omega\left[6.94\times10^{-41}\frac{C^2s^2kg^{-1}eV}{D^2}\right]+\frac{2\pi}{\hbar}V^2 FCWD(0)}$$

Eqn. S12

Unit conversion:

Since the change in dipole moment is in unit of Debye, we performed the unit conversion below to obtain $s^{-1}eV^{-1}$ for k_r per radiative transition energy $\hbar\omega$.

$$k_r = \frac{\delta K_r}{\delta\hbar\omega} = \frac{1}{3\pi\epsilon_0\hbar^4}\left(\frac{\hbar\omega}{c}\right)^3 M^2 FCWD(\hbar\omega) \times unit\ conversiton\ factor$$

$$\left[\frac{1}{s\cdot eV}\right] = \frac{1}{[A^2s^4kg^{-1}m^{-3}][eV\cdot s]^4}\left(\frac{[eV]}{\left[\frac{m}{s}\right]}\right)^3 [eV\cdot D]^2 \times \frac{1}{[eV]}$$

$$= \frac{[D]^2}{[Coulomb]^2[s]^3[kg]^{-1}[eV]^2}$$

$$= \frac{[10^{-18} statC \cdot cm]^2}{[2.998 \times 10^9 statC]^2[s]^3 \left[1.783 \times 10^{-36} \times \frac{(2.998 \times 10^{10} cm/s)^2}{eV}\right][eV]^2}$$

2. Range of parameters in energy gap law calculation

Based on previously reported parameter range,[26] we varied λ_c, λ_{qm}, $\Delta\mu$, V^2 and intramolecular phonon mode, individually, when calculating transition rates as a function of E_{CT}. In each calculation, the unchanged parameters ("Default value") for each E_{CT} and the range for the variable parameter are shown in the table below.

	Default value	Range
E_{CT} (eV)	-	0.6-2.7
λ_c (eV)	0.15	0.05-0.3
λ_{qm} (eV)	0.15	0.15-0.3
$\hbar\langle\Omega\rangle$ (eV)	0.15	
$\Delta\mu$ (D)	6	4-20
V (eV)	0.01	1e-3–1e-1

3. Discussion

As shown in Figure S4, the experimentally determined non-radiative voltage loss of polymer/non-fullerene aceptor,[4,15–21] polymer/fullerene,[19,21–25] and OLED-based OPVs[25] lie within the calculation range (Table S2). More importantly, for high-energy CT systems, such as the TADF-based system in this study, and OLED-material-based systems, non-radiative transition rates can vary by orders of magnitude, whereas radiative transition rates demonstrate a less dramatic response (Figure S3). Radiative rates vary by "only" 2-3 orders of magnitude due to reasonable changes in reorganization energies and change in dipole moment throughout the range of E_{CT} we explored (0.6eV-2.7eV). In contrast, for systems with low-energy CTs (0.5-1.0eV), non-radiative rates vary considerably more. We note that charge-transfer states in most polymer/NFA blends are around 1.0-1.5eV.[4,15,24,25,16–23] In this energy range, correct non-radiative rates can vary by 10^4-10^8 for seemingly "reasonable" values of the reorganization energy and other parameters. For higher E_{CT} systems, such as the TADF-emissive blend herein, the non-radiative rate is extremely sensitive to changes in the reorganization energy. These observations re-affirm that it is crucial to (1) control reorganization energy in CT systems to reduce non-radiative voltage loss, (2) use appropriate microscopic parameters when discussing experimental rates and voltage losses in the realm of two-state MLJ model.

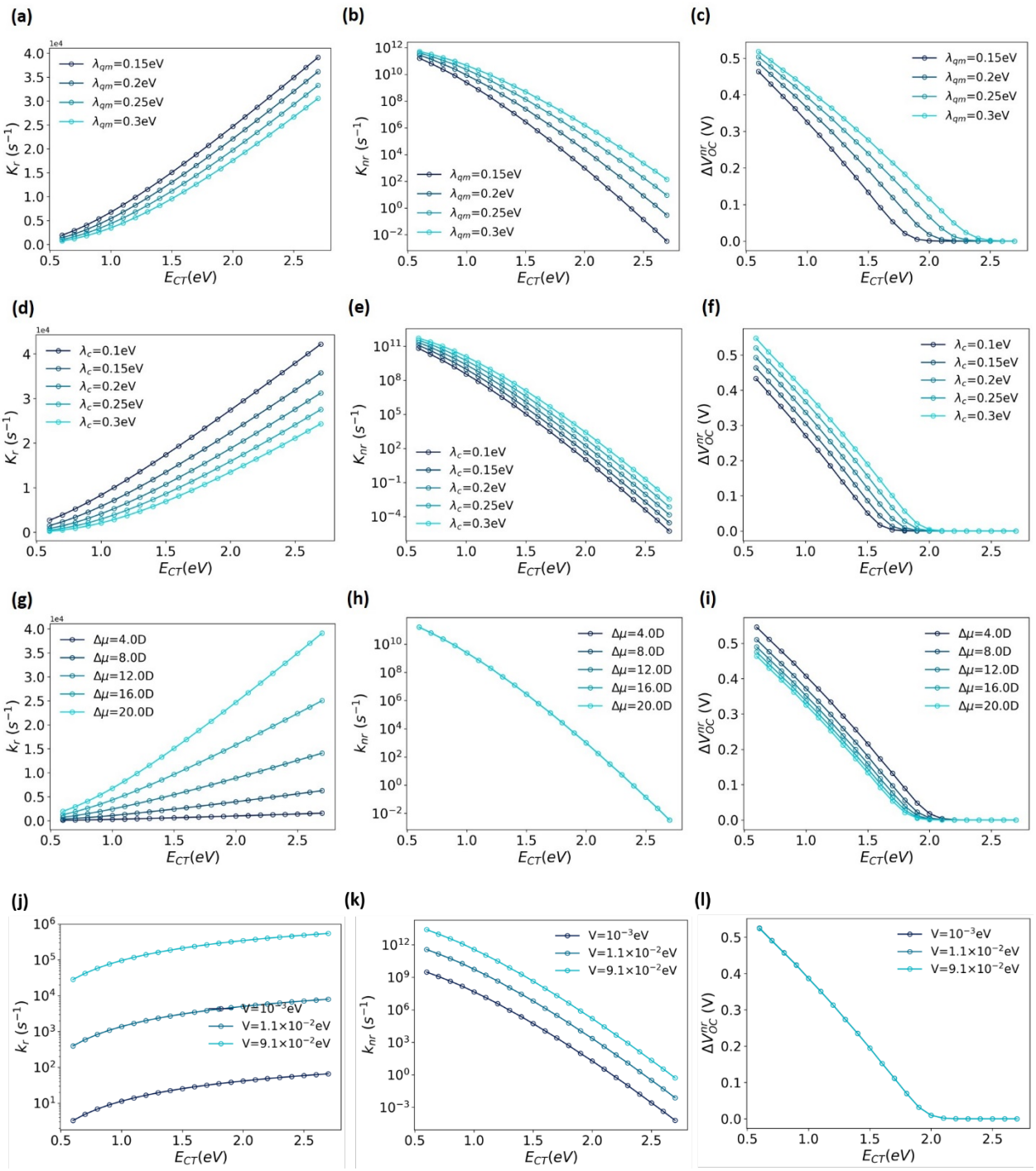

Figure S3. Effect on K_r, K_{nr} and ΔV_{OC}^{nr} as a function of E_{CT} at varying (a)-(c) λ_{qm}, (d)-(f) λ_c, (g)-(i) change in dipole moment $\Delta\mu$ and (j)-(l) electronic coupling V^2.

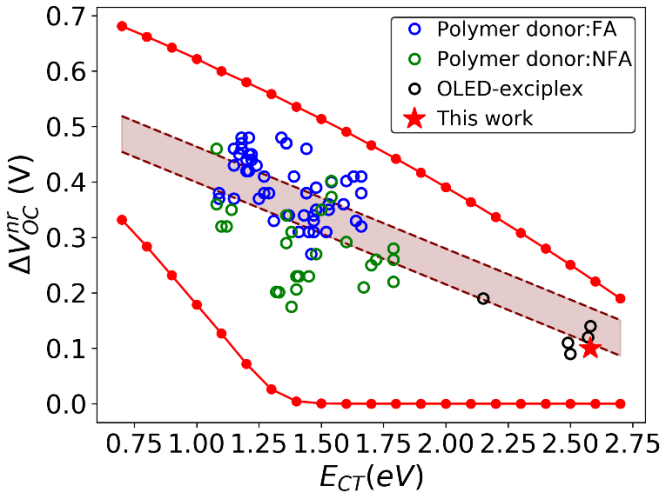

Figure S4 Expanded "energy gap law" (shown in red curve) of ΔV_{OC}^{nr} as a function of E_{CT}. The shaded area is calculated range for ΔV_{OC}^{nr} based on a linear relation between ΔV_{OC}^{nr} and $E_{CT} - \lambda_c$.[24]

Section S5 PL emission spectrum simulation

We simulate the PL emission spectrum based on the MLJ two-state model (Eqn. S15) and compare it with the experimental PL spectrum. First, we fix E_{CT} at 2.58eV determined from experiment, $\hbar\Omega$ at 0.10eV and λ_{tot} at 0.4eV. Huang-Rhys factor is varied to obtain the correct spectral peak position that overlaps with our spectrum. Static disorder (represented by σ), which leads to inhomogeneous broadening of the linewidth of the transition, is also considered.[31,32]

We show in Figure S5b that when λ_{tot} is greater than 0.4eV, PL spectrum is expected to be significantly broader than observation.

Figure S5a shows that λ_{qm} at 0.39eV would lead to the correct spectral shape and that static disorder σ is required to obscure the vibronic envelope. Previously shown, excluding the static disorder term will also lead to miscalculations of reorganization energy and CT state energy.[33] For completeness of our discussion, Figure S6a-b we thus compare k_{nr} and k_r calculation with and without σ and show that σ has negligible effect on rates.

In Figure 4a red trace, we used E_{CT} of 2.65eV. To evaluate the effect of E_{CT} on the simulation, we performed the same calculation as shown in Figure S6c-d. Our findings in the main text, i.e. k_{nr} from two-state calculation do not agree with experimental data, remain true.

$$PL(E) \propto \frac{1}{\sqrt{4\pi\lambda_c k_B T}} \sum_{w=0}^{\infty} (\mathrm{E_{CT}} - \lambda_c - \mathrm{w}\hbar\Omega)^3 \frac{e^{-S} S^w}{w!} [L_0^w(S)]^2 e^{\frac{-(\mathrm{E_{CT}} - \lambda_c - \mathrm{w}\hbar\Omega)^2}{4\lambda_c k_B T + 2\sigma^2}} \qquad \text{Eqn. S15}$$

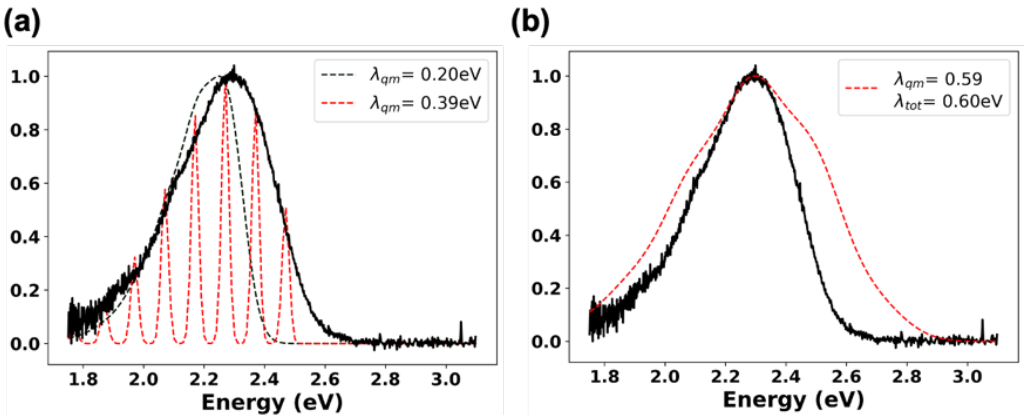

Figure S5 . Simulated PL spectra obtained from the following parameters: **(a)** λ_{total} =0.4eV, σ_s=0, ω_{qm} = 0.1eV , E_{CT} =2.58eV, λ_{qm} =0.20eV (black) or 0.39eV (red), and **(b)** λ_{total} =0.6eV, σ_s=70meV, ω_{qm} = 0.1eV, E_{CT}=2.7eV, λ_{qm}=0.59eV.

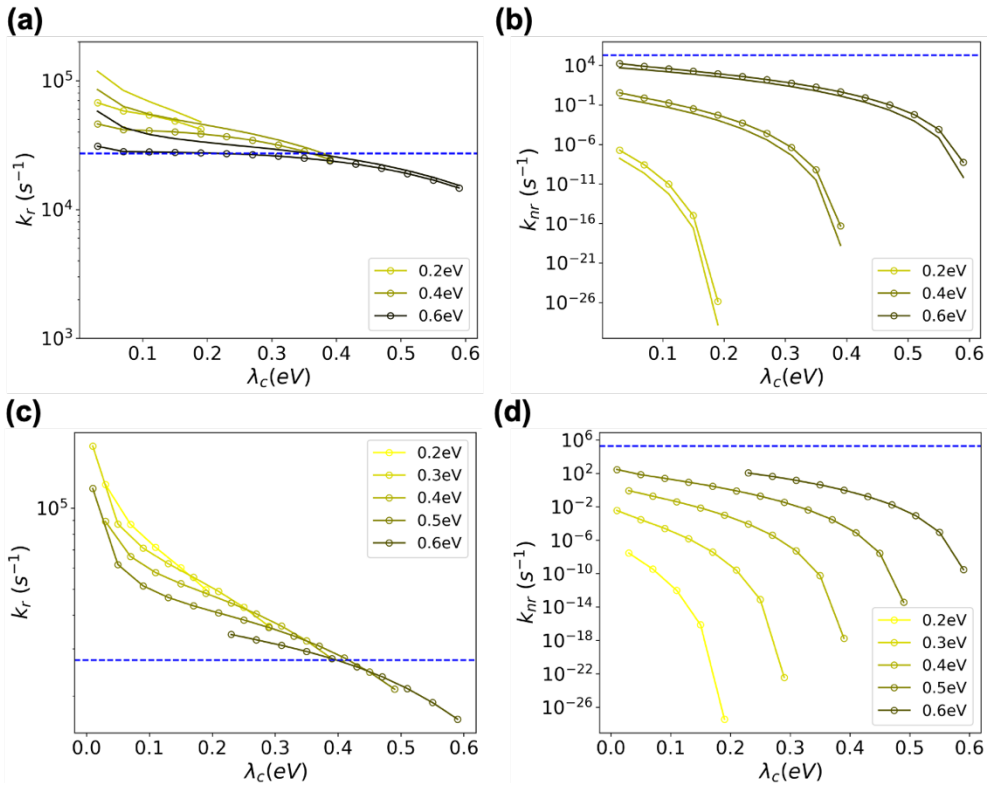

Figure S6 Comparison of **(a)** k_r and **(b)** k_{nr} with and without static disorder in Equation S9. The lighter color traces are shown in main text Figure 4b. **(c)** k_r and **(d)** k_{nr} calculation using E_{CT}=2.65eVand phonon mode of 0.1eV while varying λ_{total} from 0.2 to 0.6eV and ratio between λ_{qm} and λ_c.

Section S6. Electronic structure calculations

The morphology of the m-MTDATA/3TPYMB) blend was derived by means of molecular dynamics (MD) simulations based on the all-atom optimized potentials for liquid simulations (OPLS-AA) force field.[29] Point charge parameters of carbon, oxygen, sulfur, nitrogen, and hydrogen atoms of the donor/acceptor molecules were obtained via DFT calculations and employed for MD simulations. These parameters were shown to provide fairly accurate packing density when compared to experimental values.[30] The methodology consists of randomly placing 250 molecules each of donor and acceptor molecules in a simulation box at density of less than 0.1 gm/cc. We perform a NVT simulation at 1000 K for at least 1 ns followed by at least 5 ns isobaric-isothermal ensemble simulation at 1 bar and 300 K. A time step of 1 fs was used to integrate Newton's equations of motion. Long-range energy and coulombic corrections and particle mesh Ewald (PME) with accuracy of 0.0001 was used for computing long-range electrostatics as implemented in GROAMCS. Within these simulations we observe that the density of the

Excited-state calculations were performed by means of time-dependent DFT (TDDFT) calculations based on the Tamm-Dancoff approximation (TDA by using tuned range-separated SRSH-ωPBE-D3 functional and 6-31G(d) basis set. The geometry optimization of the donor and acceptor molecules was obtained at the same SRSH-ωPBE-D3/6-31G(d) level.

The tunning of the range-separated parameters (ω) was performed by minimizing the error function J(ω):

$$J(\omega) = [\epsilon_{HOMO}(\omega) - IP(\omega)]^2 + [\epsilon_{LUMO}(\omega) - EA(\omega)]^2$$

Here, ϵ_{HOMO} and ϵ_{LUMO} are the energies of highest occupied and lowest unoccupied molecular orbitals (HOMO and LUMO); IP and EA denote the vertical first ionization potential and electron affinity of the system. A value of 0.10 $bohr^{-1}$ was derived for the optimal value of ω.

All the excited-state calculations were performed with the Q-chem 4 package and, MD simulations were carried out using GROMACS software.[31,32] A dielectric constant of 3 was used in all these calculations.

Section S7 PL emission spectrum simulation

We calculate the k_r, k_{nr} and PLQY for a range of CT energies using the three-state model described in the main text. For the main text figure, we fix all microscopic parameters, except E_{CT}. According to Eqn.5 in main text, this varies the $f_{CT\text{-}LE}$ too, and therefore this calculation demonstrates the effect of $\Delta E_{CT\text{-}LE}$ on the CT-LE mixing and the CT transition rates and PLQY.
Values of the parameters used are based on experimental value of the low gap component m-MTDATA donor and the CT state.

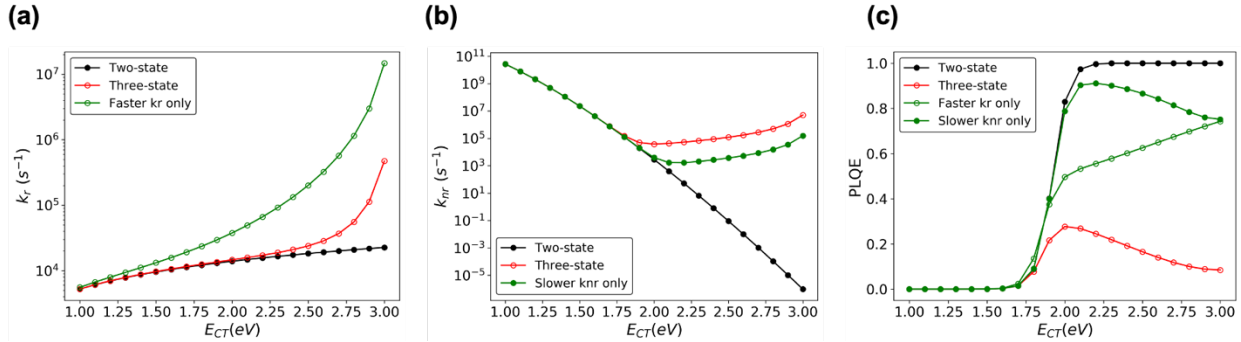

Figure S7. k_r, k_{nr} and PLQY of the CT state calculated at a range of CT energies when PLQY of the LE is varied. Black: two-state calculation. Red: three-state calculation where PLQY of LE is 10%. Green: Three-state calculation where PLQY of LE is 80% by increasing transition dipole moment or by slowing down k_{nr} is also shown.

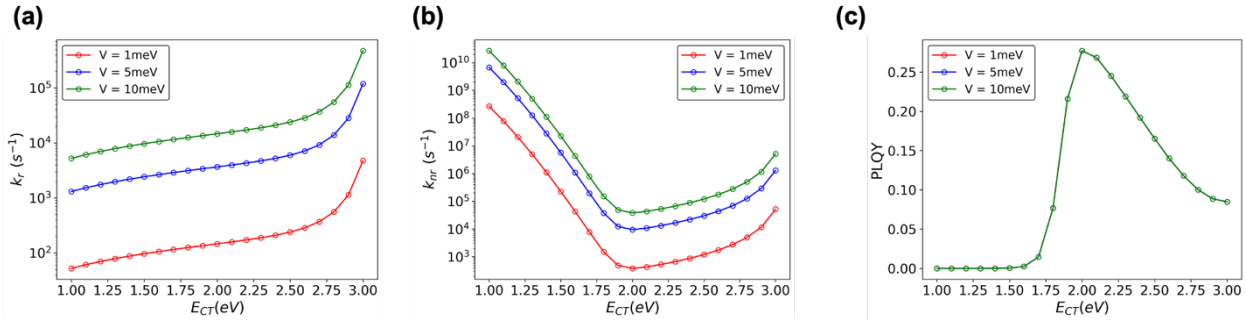

Figure S8. k_r, k_{nr} and PLQY of the CT state calculated at a range of CT energies when the CT-G and CT-LE electronic coupling vary from 1 mev, 5 meV to 10 meV. PLQY of LE is 10%.

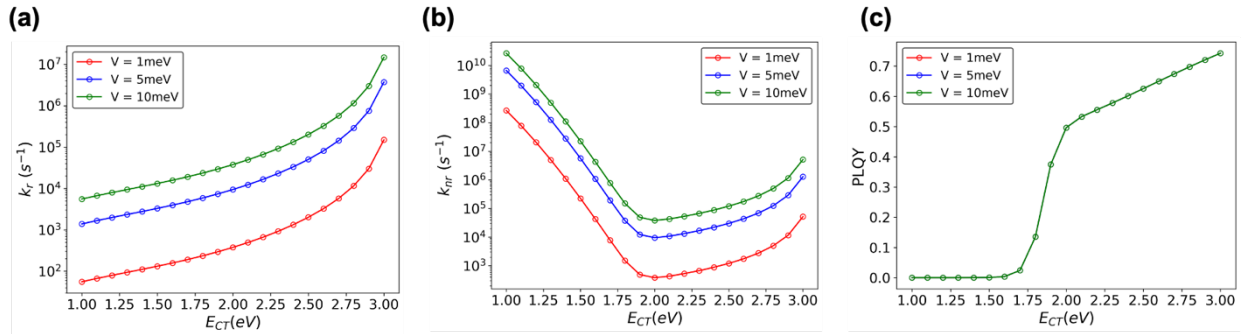

Figure S9. k_r, k_{nr} and PLQY of the CT state calculated at a range of CT energies when the CT-G and CT-LE electronic coupling vary from 1 mev, 5 meV to 10 meV. PLQY of LE is 80%.

Table S2. Summary of E_{CT}, PLQY, k_r and k_{nr} values of CT states in donor/acceptor OPV blends. E_{CT} is determined by fitting EQE_{PV} tail and EL spectra to a set of Gaussians (†), or by the intersection between normalized absorption and PL spectra (‡). Systems in ref 35 are reported to show CT-LE hybridization that increases k_r. λ_{tot} obtained from EQE_{PV} and EL fitting (* indicates the numbers were tabulated from the original published figure).

	E_{CT}	λ_{tot}	PLQY	k_r (s^{-1})	k_{nr} (s^{-1})	Ref
m-MTDATA:3TPYMB	2.58†	0.41	0.128 (prompt)	2.75E+04	1.87E+05	This work
PIDSe-PhQ:PCBM	1.35†	0.19*	9.1E-05	1.08E+05	1.19E+09	[34]
PIDT-PhQ:PCBM	1.41†	0.19*	1.3E-04	9.71E+04	7.25E+08	[34]
PIDT-PhanQ:PCBM	1.43†	0.19*	1.9E-04	1.47E+05	7.81E+08	[34]
PIDSe-PhanQ:PCBM	1.42†	0.19*	2.2E-04	2.99E+05	1.39E+09	[34]
PCE10:FIDTT-2PDI	1.6†	0.15	1.4E-04	3.43E+05	2.52E+09	[4]
PNOz4T:PC71BM	1.58‡	--	8.0E-03	2.32E+07	2.88E+09	[35]
PDCBT-2F:IT-M	1.67‡	--	1.2E-02	1.58E+08	1.30E+10	[35]
PTB7-Th:IEICO	1.67‡	--	7.0E-03	9.94E+07	1.41E+10	[35]
PBQ-QF:IEICO-4F	1.36‡	--	1.0E-04	4.38E+06	4.38E+10	[35]
PvBDTTAZ:O-IDTBR	1.7‡	--	1.2E-02	1.75E+08	1.44E+10	[35]

Table S3. Summary of E_{CT} and ΔV_{nr} values in donor/acceptor OPV blends.

Polymer:NFA	**E_{CT}**	**ΔV_{nr}**	**Ref**
PCE10:FIDTT-2PDI	1.6	0.292	[4]
P3TEA:SF-PDI2	1.72	0.26	[36]
PBDB-T:ITIC	1.5	0.35	[15]
PDCBT-2F:IT-M	1.67	0.21	[35]
PTB7-Th:IEICO	1.45	0.23	[35]
PBQ-QF:IEICO-4F	1.36	0.29	[35]
PvBDTTAZ:O-IDTBR	1.7	0.25	[35]
BDT-ffBX-DT:SFPPDI	1.79	0.22	[20]
BDT-ffBX-DT:PDI4	1.79	0.28	[20]
BDT-ffBX-DT:PDI6	1.79	0.26	[20]
PBDB-T:NCBDT	1.54	0.373	[17]
PBDB-T:NCBDT	1.54	0.402	[17]
P6:Y11	1.38	0.175	[19]
P6:Y11	1.33	0.201	[19]
P6:Y11	1.32	0.202	[19]
PBDB-TF:BTP-4F	1.4	0.23	[37]
PBDB-TF:BTP-4Cl	1.4	0.206	[37]
D-0F:8C-ITIC	1.12	0.32	[21]
D-2F:8C-ITIC	1.38	0.31	[21]
D-4F:8C-ITIC	1.41	0.23	[21]
D-0F:ITIC	1.1	0.32	[21]
D-2F:ITIC	1.36	0.34	[21]
D-4F:ITIC	1.48	0.27	[21]
D-0F:IT-4F	1.08	0.46	[21]
D-2F:IT-4F	1.08	0.36	[21]
D-4F:IT-4F	1.14	0.35	[21]
Polymer:fullerene	**E_{CT}**	**ΔV_{nr}**	**Ref**
PIPCP:PC61BM	1.46	0.27	[24]
DCV5T-Me:C60	1.47	0.31	[25]
PM6:PCBM	1.6	0.402	[25]
APFO3:PC61BM	1.64	0.33	[24]
APFO3:PC61BM	1.66	0.38	[24]
APFO3:PC61BM	1.66	0.32	[24]
APFO3:PC71BM	1.63	0.41	[24]
APFO3:PC71BM	1.66	0.41	[24]
Dihexyl-PTV:PC61BM	1.22	0.45	[24]
High-Tg-PPV:PC61BM	1.44	0.38	[24]

LBPP5:PC71BM	1.39	0.41	[24]
MDMO-PPV:PC61BM	1.41	0.31	[24]
MDMO-PPV:PC61BM	1.47	0.34	[24]
MDMO-PPV:PC61BM	1.53	0.35	[24]
MDMO-PPV:PC61BM	1.53	0.36	[24]
MDMO-PPV:PC61BM	1.52	0.31	[24]
OC9-PEO-PPV:PC61BM	1.34	0.48	[24]
P34T:PC61BM	1.18	0.48	[24]
P34T:PC61BM	1.15	0.46	[24]
P35T:PC61BM	1.21	0.42	[24]
P35T:PC61BM	1.18	0.46	[24]
P35T:PC61BM	1.17	0.45	[24]
P35T:PC61BM	1.15	0.43	[24]
P36T:PC61BM	1.24	0.43	[24]
P36T:PC61BM	1.22	0.44	[24]
P36T:PC61BM	1.21	0.45	[24]
P36T:PC61BM	1.2	0.44	[24]
P3HT:PC61BM	1.37	0.34	[24]
P3HT:PC61BM	1.2	0.42	[24]
ReRa-P3HT:PC61BM	1.47	0.33	[24]
PBDTTPD:PC71BM	1.54	0.4	[24]
PCDTBT:PC71BM	1.48	0.39	[24]
PCPDTBT:PC71BM	1.29	0.38	[24]
PCPDTBT:PC71BM	1.25	0.37	[24]
TQm6:PC71BM	1.45	0.31	[24]
TQm8:PC71BM	1.48	0.35	[24]
TQmEH:PC71BM	1.43	0.34	[24]
TQp6:PC71BM	1.21	0.48	[24]
TQp8:PC71BM	1.27	0.41	[24]
TQp12:PC71BM	1.31	0.33	[24]
D-0F:Bis-5.1-PCBM	1.18	0.47	[21]
D-2F:Bis-5.1-PCBM	1.44	0.46	[21]
D-4F:Bis-5.1-PCBM	1.59	0.36	[21]
D-0F:PC70BM	1.15	0.37	[21]
D-2F:PC70BM	1.27	0.38	[21]
D-4F:PC70BM	1.44	0.38	[21]
D-0F:C60C70	1.09	0.38	[21]
D-2F:C60C70	1.09	0.37	[21]
D-4F:C60C70	1.36	0.47	[21]
OLED-based	**E_{CT}**	**ΔV_{nr}**	**Ref**

BF-DPB:TmPPPyTz	2.5	0.09	[25]
TAPC:TmPPPyTz	2.57	0.12	[25]
TCTA:TmPPPyTz	2.58	0.14	[25]
BF-DPB:B4PYMPM	2.49	0.11	[25]
m-MTDATA:B4PYMPM	2.15	0.19	[25]

References

(1) Byrnes, S. J. Multilayer Optical Calculations. *arXiv 1603 . 02720v3* **2018**, 1–20.

(2) De Mello, J. C.; Wittmann, H. F.; Friend, R. H. An Improved Experimental Determination of External Photoluminescence Quantum Efficiency. *Adv. Mater.* **1997**, *9* (3), 230–232. https://doi.org/10.1201/b10862-2.

(3) Goushi, K.; Yoshida, K.; Sato, K.; Adachi, C. Organic Light-Emitting Diodes Employing Efficient Reverse Intersystem Crossing for Triplet-to-Singlet State Conversion. *Nature* **2012**, *6* (March). https://doi.org/10.1038/nphoton.2012.31.

(4) Ziffer, M. E.; Jo, S. B.; Zhong, H.; Ye, L.; Liu, H.; Lin, F.; Zhang, J.; Li, X.; Ade, H. W.; Jen, A. K.-Y.; Ginger, D. S. Long-Lived, Non-Geminate, Radiative Recombination of Photogenerated Charges in a Polymer:Small-Molecule Acceptor Photovoltaic Blend. *J. Am. Chem. Soc.* **2018**, *140* (31), 9996–10008. https://doi.org/10.1021/jacs.8b05834.

(5) Shockley, W.; Queisser, H. J. Detailed Balance Limit of Efficiency of P- n Junction Solar Cells. **2014**, *510* (May 1960).

(6) Azzouzi, M.; Yan, J.; Kirchartz, T.; Liu, K. K.; Wang, J. L.; Wu, H. B.; Nelson, J. Nonradiative Energy Losses in Bulk-Heterojunction Organic Photovoltaics. *Phys. Rev. X* **2018**, *8*. https://doi.org/Artn 031055 10.1103/Physrevx.8.031055.

(7) Yao, J.; Kirchartz, T.; Vezie, M. S.; Faist, M. A.; Gong, W.; He, Z.; Wu, H.; Troughton, J.; Watson, T.; Bryant, D.; Nelson, J. Quantifying Losses in Open-Circuit Voltage in Solution-Processable Solar Cells. *Phys. Rev. Appl.* **2015**, *014020*, 1–10. https://doi.org/10.1103/PhysRevApplied.4.014020.

(8) Rau, U.; Blank, B.; Müller, T. C. M.; Kirchartz, T.; Jülich, F. Efficiency Potential of Photovoltaic Materials and Devices Unveiled by Detailed-Balance Analysis. *Phys. Rev. Appl.* **2017**, No. 7, 044016. https://doi.org/10.1103/PhysRevApplied.7.044016.

(9) Rau, U. Reciprocity Relation between Photovoltaic Quantum Efficiency and Electroluminescent Emission of Solar Cells. *Phys. Rev. B* **2007**, *76* (8), 1–8. https://doi.org/10.1103/PhysRevB.76.085303.

(10) Coropceanu, Veaceslav; Chen, Xian-Kai; Wang, Tonghui; Zheng, Zilong; Bredas, J.-L. Charge-Transfer Electronic States in Organic Solar Cells. *Nat. Rev. Mater.* **2019**. https://doi.org/10.1038/s41578-019-0137-9.

(11) Wang, Y.; Qian, D.; Cui, Y.; Zhang, H.; Hou, J.; Vandewal, K.; Kirchartz, T.; Gao, F. Optical Gaps of Organic Solar Cells as a Reference for Comparing Voltage Losses. *Adv. Energy Mater.* **2018**, 1801352. https://doi.org/10.1002/aenm.201801352.

(12) Azzouzi, M.; Yan, J.; Kirchartz, T.; Liu, K.; Wang, J.; Wu, H.; Nelson, J. Nonradiative Energy Losses in Bulk-Heterojunction Organic Photovoltaics. *Phys. Rev. X* **2018**, *8* (3), 1–14. https://doi.org/10.1103/PhysRevX.8.031055.

(13) Zhao, W.; Qian, D.; Zhang, S.; Li, S.; Inganäs, O.; Gao, F.; Hou, J. Fullerene-Free Polymer Solar Cells with over 11% Efficiency and Excellent Thermal Stability. *Adv. Mater.* **2016**, *28* (23), 4734–4739. https://doi.org/10.1002/adma.201600281.

(14) Qian, D.; Zheng, Z.; Yao, H.; Tress, W.; Hopper, T. R.; Chen, S.; Li, S.; Liu, J.; Chen, S.; Zhang, J.; Liu, X.-K.; Gao, B.; Ouyang, L.; Jin, Y.; Pozina, G.; Buyanova, I. A.; Chen, W. M.; Inganäs, O.; Coropceanu, V.; Bredas, J.-L.; Yan, H.; Hou, J.; Zhang, F.; Bakulin, A. A.; Gao, F. Design Rules for Minimizing Voltage Losses in High-Efficiency Organic Solar Cells. *Nat. Mater.* **2018**, *17* (8), 703–709. https://doi.org/10.1038/s41563-018-0128-z.

(15) Zhang, J.; Kan, B.; Pearson, A. J.; Parnell, A. J.; Cooper, J. F. K.; Liu, X. K.; Conaghan, P. J.; Hopper, T. R.; Wu, Y.; Wan, X.; Gao, F.; Greenham, N. C.; Bakulin, A. A.; Chen, Y.; Friend, R. H. Efficient Non-Fullerene Organic Solar Cells Employing Sequentially Deposited Donor-Acceptor Layers. *J. Mater. Chem. A* **2018**, *6* (37), 18225–18233. https://doi.org/10.1039/c8ta06860g.

(16) Liu, J.; Chen, S.; Qian, D.; Gautam, B.; Yang, G.; Zhao, J.; Bergqvist, J.; Zhang, F.; Ma, W.; Ade, H.; Inganäs, O.; Gundogdu, K.; Gao, F.; Yan, H. Fast Charge Separation in a Non-Fullerene Organic Solar Cell with a Small Driving Force. *Nat. Energy* **2016**, *1* (7), 16089–16095. https://doi.org/10.1038/nenergy.2016.89.

(17) Liu, S.; Yuan, J.; Deng, W.; Luo, M.; Xie, Y.; Liang, Q.; Zou, Y.; He, Z.; Wu, H.; Cao, Y. High-Efficiency Organic Solar Cells with Low Non-Radiative Recombination Loss and Low Energetic Disorder. *Nat. Photonics* **2020**. https://doi.org/10.1038/s41566-019-0573-5.

(18) Liu, X.; Du, X.; Wang, J.; Duan, C.; Tang, X.; Heumueller, T.; Liu, G.; Li, Y.; Wang, Z.; Wang, J.; Liu, F.; Li, N.; Brabec, C. J.; Huang, F.; Cao, Y. Efficient Organic Solar Cells with Extremely High Open-Circuit Voltages and Low Voltage Losses by Suppressing Nonradiative Recombination Losses. *Adv. Energy Mater.* **2018**, *8* (26), 1–9. https://doi.org/10.1002/aenm.201801699.

(19) Eisner, F. D.; Azzouzi, M.; Fei, Z.; Hou, X.; Anthopoulos, T. D.; Dennis, T. J. S.; Heeney, M.; Nelson, J. Hybridization of Local Exciton and Charge-Transfer States Reduces Nonradiative Voltage Losses in Organic Solar Cells. *J Am Chem Soc* **2019**, *141*, 6362–6374. https://doi.org/10.1021/jacs.9b01465.

(20) Ran, N. A.; Love, J. A.; Takacs, C. J.; Sadhanala, A.; Beavers, J. K.; Collins, S. D.; Huang, Y.; Wang, M.; Friend, R. H.; Bazan, G. C. Harvesting the Full Potential of Photons with Organic Solar Cells. *Adv. Mater.* **2016**, 1482–1488. https://doi.org/10.1002/adma.201504417.

(21) Wang, C.; Xu, X.; Zhang, W.; Bergqvist, J.; Xia, Y.; Meng, X.; Bini, K.; Ma, W.; Yartsev, A.; Vandewal, K.; Andersson, M. R.; Inganäs, O.; Fahlman, M.; Wang, E. Low Band Gap Polymer Solar Cells With Minimal Voltage Losses. *Adv. Energy Mater.* **2016**, *6* (18), 1–10. https://doi.org/10.1002/aenm.201600148.

(22) Benduhn, J.; Tvingstedt, K.; Piersimoni, F.; Ullbrich, S.; Fan, Y. L.; Tropiano, M.; McGarry, K. A.; Zeika, O.; Riede, M. K.; Douglas, C. J.; Barlow, S.; Marder, S. R.; Neher, D.;

Spoltore, D.; Vandewal, K. Intrinsic Non-Radiative Voltage Losses in Fullerene-Based Organic Solar Cells. *Nat. Energy* **2017**, *2*. https://doi.org/Artn 17053 10.1038/Nenergy.2017.53.

(23) Ullbrich, S.; Benduhn, J.; Jia, X. K.; Nikolis, V. C.; Tvingstedt, K.; Piersimoni, F.; Roland, S.; Liu, Y.; Wu, J. H.; Fischer, A.; Neher, D.; Reineke, S.; Spoltore, D.; Vandewal, K. Emissive and Charge-Generating Donor-Acceptor Interfaces for Organic Optoelectronics with Low Voltage Losses. *Nat. Mater.* **2019**, *18*, 459. https://doi.org/10.1038/s41563-019-0324-5.

(24) Jorgensen, W. L.; Maxwell, D. S.; Tirado-Rives, J. Development and Testing of the OPLS All-Atom Force Field on Conformational Energetics and Properties of Organic Liquids. *J. Am. Chem. Soc.* **1996**, *118* (45), 11225–11236. https://doi.org/10.1021/ja9621760.

(25) Wunsch, B. H.; Rumi, M.; Tummala, N. R.; Risko, C.; Kang, D. Y.; Steirer, K. X.; Gantz, J.; Said, M.; Armstrong, N. R.; Brédas, J. L.; Bucknall, D.; Marder, S. R. Structure-Processing-Property Correlations in Solution-Processed, Small-Molecule, Organic Solar Cells. *J. Mater. Chem. C* **2013**, *1* (34), 5250–5260. https://doi.org/10.1039/c3tc30774c.

(26) Kronik, L.; Stein, T.; Refaely-Abramson, S.; Baer, R. Excitation Gaps of Finite-Sized Systems from Optimally Tuned Range-Separated Hybrid Functionals. *J. Chem. Theory Comput.* **2012**, *8* (5), 1515–1531. https://doi.org/10.1021/ct2009363.

(27) Voityuk, A. A.; Rösch, N. Fragment Charge Difference Method for Estimating Donor-Acceptor Electronic Coupling: Application to DNA π-Stacks. *J. Chem. Phys.* **2002**, *117* (12), 5607–5616. https://doi.org/10.1063/1.1502255.

(28) Hess, B.; Kutzner, C.; Van Der Spoel, D.; Lindahl, E. GRGMACS 4: Algorithms for Highly Efficient, Load-Balanced, and Scalable Molecular Simulation. *J. Chem. Theory Comput.* **2008**, *4* (3), 435–447. https://doi.org/10.1021/ct700301q.

(29) Berendsen, H. J. C.; van der Spoel, D.; van Drunen, R. GROMACS: A Message-Passing Parallel Molecular Dynamics Implementation. *Comput. Phys. Commun.* **1995**, *91* (1–3), 43–56. https://doi.org/10.1016/0010-4655(95)00042-E.

(30) Kahle, F. J.; Rudnick, A.; Bässler, H.; Köhler, A. How to Interpret Absorption and Fluorescence Spectra of Charge Transfer States in an Organic Solar Cell. *Mater. Horizons* **2018**, *5* (5), 837–848. https://doi.org/10.1039/c8mh00564h.

(31) Zheng, Z.; Tummala, N. R.; Wang, T.; Coropceanu, V.; Brédas, J.-L. Charge-Transfer States at Organic–Organic Interfaces: Impact of Static and Dynamic Disorders. *Adv. Energy Mater.* **2019**, *9* (14), 1803926. https://doi.org/10.1002/aenm.201803926.

(32) Burke, T. M.; Sweetnam, S.; Vandewal, K.; McGehee, M. D. Beyond Langevin Recombination: How Equilibrium Between Free Carriers and Charge Transfer States Determines the Open-Circuit Voltage of Organic Solar Cells. *Adv. Energy Mater.* **2015**, *5* (11). https://doi.org/Artn 150012310.1002/Aenm.201500123.

(33) Sulas, D. B.; Rabe, E. J.; Schlenker, C. W. Kinetic Competition between Charge Separation and Triplet Formation in Small-Molecule Photovoltaic Blends. *J. Phys. Chem. C* **2017**, *121* (48), 26667–26676. https://doi.org/10.1021/acs.jpcc.7b09365.

(34) Qian, D.; Zheng, Z.; Yao, H.; Tress, W.; Hopper, T. R.; Chen, S.; Li, S.; Liu, J.; Chen, S.;

Zhang, J.; Liu, X. K.; Gao, B.; Ouyang, L.; Jin, Y.; Pozina, G.; Buyanova, I. A.; Chen, W. M.; Inganäs, O.; Coropceanu, V.; Bredas, J. L.; Yan, H.; Hou, J.; Zhang, F.; Bakulin, A. A.; Gao, F. Design Rules for Minimizing Voltage Losses in High-Efficiency Organic Solar Cells. *Nat. Mater.* **2018**, *17* (8), 703–709. https://doi.org/10.1038/s41563-018-0128-z.

(35) Liu, J.; Chen, S. S.; Qian, D. P.; Gautam, B.; Yang, G. F.; Zhao, J. B.; Bergqvist, J.; Zhang, F. L.; Ma, W.; Ade, H.; Inganas, O.; Gundogdu, K.; Gao, F.; Yan, H. Fast Charge Separation in a Non-Fullerene Organic Solar Cell with a Small Driving Force. *Nat. Energy* **2016**, *1*. https://doi.org/Artn 16089 10.1038/Nenergy.2016.89.

(36) Cui, Y.; Yao, H.; Zhang, J.; Zhang, T.; Wang, Y.; Hong, L.; Xian, K.; Xu, B.; Zhang, S.; Peng, J.; Wei, Z.; Gao, F.; Hou, J. Over 16% Efficiency Organic Photovoltaic Cells Enabled by a Chlorinated Acceptor with Increased Open-Circuit Voltages. *Nat. Commun.* **2019**, No. 2019, 1–8. https://doi.org/10.1038/s41467-019-10351-5.

Appendix C. Supporting information for Chapter 4

Experimental methods

Electroabsorption spectroscopy measurement

Figure S7 shows the experimental set up for the electroabsorption measurement in the transmission mode. During the measurement, an alternating electric field is applied to the sample via a voltage waveform with its frequency (ω) and amplitude programmed on the function generator. The sample is oriented with respect to the monochromated polarized light such that the electric field across the sample and the electric field of the incident light cross at the magic angle (~54.7°). The transmitted light is focused onto a silicon photodiode. The detected signal is amplified via a current pre-amplifier and outputs to a lock-in amplifier and a Keithley voltmeter. The lock-in amplifier is synced to 2ω of the applied AC field and detects the change of transmitted light intensity due to the field. The Keithley voltmeter detects the transmitted light intensity.

Sample fabrication

The sample for EA measurement is a multi-layer capacitor-type device with the following structure: ITO/Cytop/SiO_2/active layer/SiO_2/Cytop/Al (Figure S8). This structure allows for the measurement to be performed in the transmission mode while eliminating direct charge injection. Transparent ITO substrates act as the bottom electrode. Cytop solution is spin cast onto the substrate to form an insulating layer. SiO2 is deposited as a second insulating layer via electron-beam under high vacuum. The organic solution is spin cast onto the substrate to form a 50-100nm thin film. Then, SiO2 is e-beamed and Cytop solution is spin-cast. Finally, a thin Al layer is deposited via thermal evaporation to act as the semitransparent electrode to allow for light transmission.

Ellipsometry measurement

We performed variable angle spectroscopic ellipsometry (VASE) measurement to determine the refractive indices of each layer in the EA sample stack. VASE measures the change in polarization, both the amplitude ratio Ψ and the phase difference Δ, as light from various incidence angles reflects or transmits from the material. Spectra of Ψ and Δ were measured on material deposited onto silicon substrates with 300 nm thermally grown SiO_2, at 3 different incidence angles (55°, 65° and 75°). The complex refractive indices n and k were modeled using a B-Spline model via the CompleteEASE software from J.A. Woollam Co.

Supplementary information

Section 1. Data analysis of EA

As mentioned in main text, microscopic parameters including Δμ and Δp can be extracted via the Liptay equation. The most common methods directly fit the derivatives of the absorption spectrum to the Liptay equation.[1] In one method, the absorption spectrum is reconstructed with several

Gaussian functions and the linear combination of the Gaussian components and their corresponding derivatives are fit to the Liptay equation. In the second method, the experimental absorption spectrum is first smoothed using a filter function and then the derivatives are obtained by direct numerical differentiation of the smoothened data. Both methods add some ambiguity and potential artifacts to the EA lineshape, which is a highly sensitive reflection of the macroscopic parameters. Furthermore, previous reports have shown that optical absorption omits light interference within the sample stack and thus cannot be used to model EA response.

We fit the experimental spectrum to the expected change in transmittance via a transfer matrix method based on refractive indices (n and k).[2] This method is more robust because (1) the original experimental data, rather than a reconstruction based on Gaussians, is used, (2) with good S/N ratio, no data smoothing is necessary, and (3) light interference between each sample layer is accounted for. Briefly, EA response reflects the change in n and k of the active layer due to the external electric field. This effect can be expressed by the Liptay equation.

$$\Delta k(\nu) = F^2\{A_\chi k(\nu) + \frac{B_\chi}{15hc}\nu\frac{d}{d\nu}\left(\frac{k(\nu)}{\nu}\right) + \frac{C_\chi}{30h^2c^2}\nu\frac{d^2}{d\nu^2}\left(\frac{k(\nu)}{\nu}\right)$$

Derivation for this form of the Liptay equation from Eqn. 4.5 is shown in a previous publication.[2] To model transmittance with and without the applied field, we use the corresponding refractive indices of each layer (only refractive indices of the active layer are perturbed by the field) and a transfer matrix method. The refractive indices are determined from ellipsometry measurements.

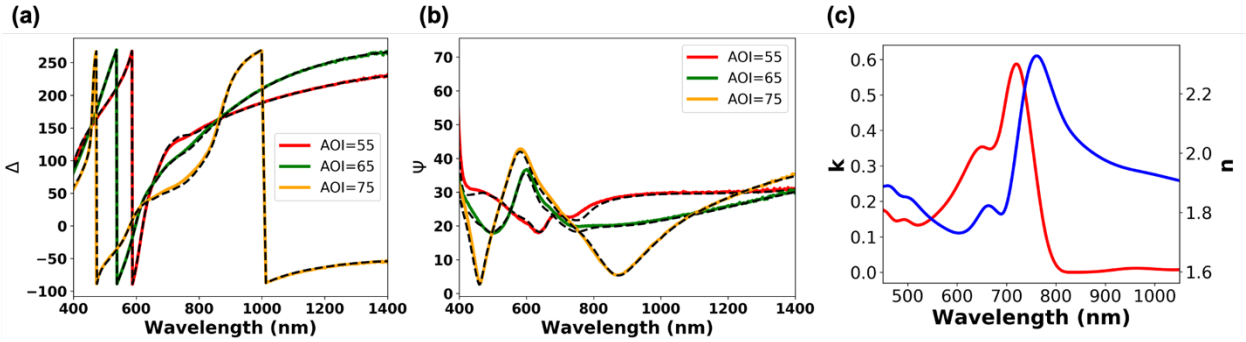

Figure S1. Fitting results of ellipsometry data of PCE10:$PC_{60}BM$ blend: **(a)** Ψ and **(b)** Δ at three angles of incidence (AOI). Refractive indices n and k are shown in **(c)**.

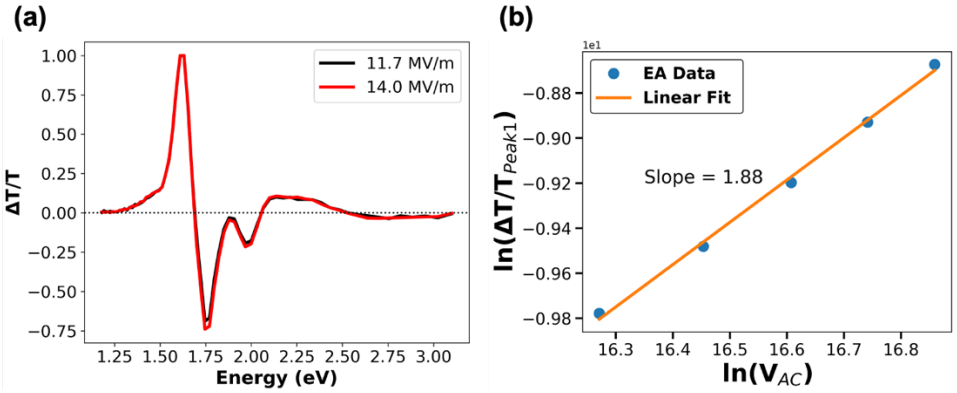

Figure S2. (a) Normalized EA spectrum of PCE10:PC60BM at two field strengths. **(b)** Magnitude of the low energy ΔT/T peak as a function of applied field.

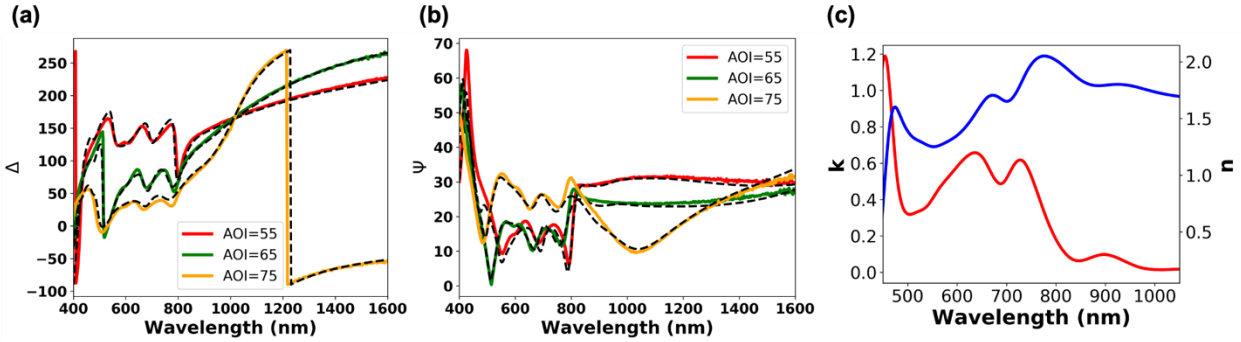

Figure S3. Fitting results of ellipsometry data of PBDB-T:IT-4F blend: **(a)** Ψ and **(b)** Δ at three angles of incidence (AOI). Refractive indices n and k are shown in **(c)**.

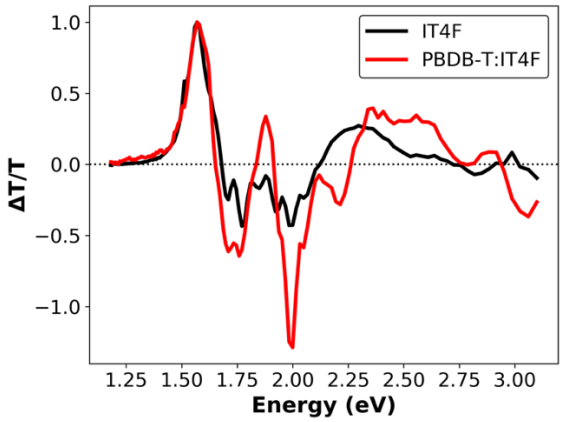

Figure S4. Comparison of EA spectra: PBDB-T:IT-4F and pure IT-4F.

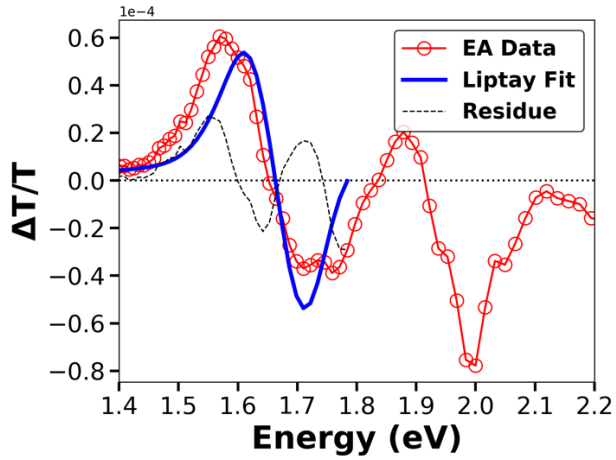

Figure S5. Fitting result of PBDB-T:IT-4F blend to Liptay equation.

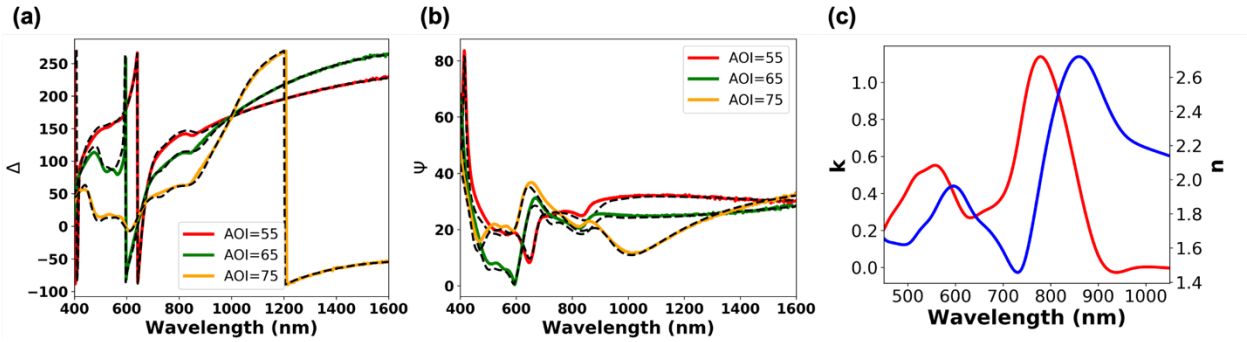

Figure S6. Fitting results of ellipsometry data of PTO2:Y6 blend: **(a)** Ψ and **(b)** Δ at three angles of incidence (AOI). Refractive indices n and k are shown in **(c)**.

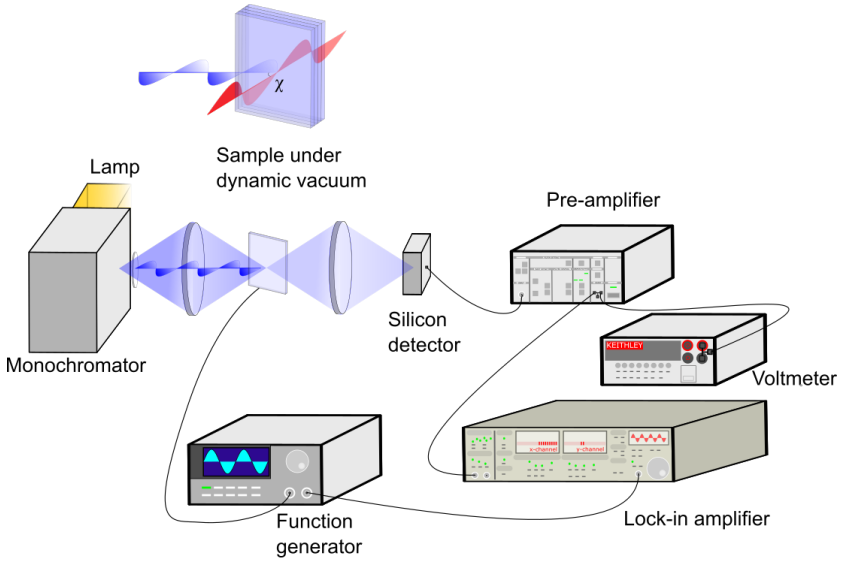

Figure S7. Experimental setup for EA measurement in transmission mode. The angle between electric field within the sample (shown in red) and field of the polarized light (shown in purple) is defined as χ.

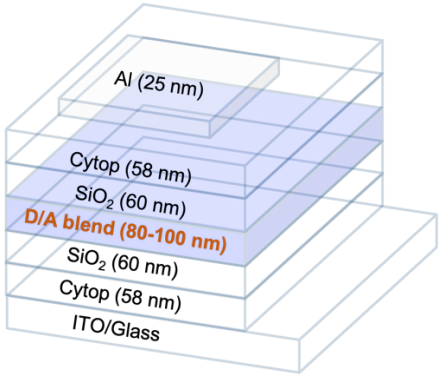

Figure S8. EA sample stack. Layer thickness is determined via ellipsometry fitting.

References

(1) Bublitz, G. U.; Boxer, S. G. Stark Spectroscopy: Applications in Chemistry, Biology, and Materials Science. *Annu. Rev. Phys. Chem.* **1997**, *48* (1), 213–242. https://doi.org/10.1146/annurev.physchem.48.1.213.

(2) Ziffer, M. E.; Jo, S. B.; Liu, Y.; Zhong, H. L.; Mohammed, J. C.; Harrison, J. S.; Jen, A. K. Y.; Ginger, D. S. Tuning H- and J-Aggregate Behavior in, Pi-Conjugated Polymers via Noncovalent Interactions. *J. Phys. Chem. C* **2018**, *122*, 18860–18869. https://doi.org/10.1021/acs.jpcc.8b05505.